Msc Thesis

Dynamic simulation of a geothermal reservoir

Case study of the Dinantian carbonates in the Californië geothermal wells, Limburg, NL

D.F.H. Reith

TU Delft

Dynamic simulation of a geothermal reservoir

Case study of the Dinantian carbonates in the Californië geothermal wells, Limburg, NL

By

D.F.H. Reith
4212185

In partial fulfilment of the requirements for the degree of Master of Science in Petroleum Engineering at the Delft University of Technology,
to be defended publicly on August 22, 2018 at 13:00 in Zaal F, CiTG

This Thesis is confidential and can be (partially) made public

Project duration	Nov 2017 – August 2018	
Supervision	Prof. Dr. G.Bertotti	TU Delft
	Dr. Ir. R. Godderij, Reservoir Engineer	EBN B.V.
	Drs. B. Jaarsma, Geoscientist	EBN B.V.
Thesis committee	Prof. Dr. G.Bertotti	TU Delft
	Dr. D.V. Voskov	TU Delft
	Drs. J.C. Blom	TU Delft
	Dr. Ir. R. Godderij	EBN B.V.
	Drs. B. Jaarsma	EBN B.V.

Abstract

In the context of the energy transition, rapid development of the geothermal sector in the Netherlands has to take place. The first steps have been taken by establishing the Green Deal UDG between multiple industrial consortia, which agree to share knowledge on the research and use of ultra-deep geothermal energy . The Dinantian carbonates are of interest for the deep geothermal wells, because of their high geothermal potential. This research project provides a case study of the Californië geothermal doublets in Limburg (NL), which are currently the only geothermal wells in the Netherlands producing from the Dinantian carbonates. However, the static and dynamic model prove that the Devonian Bosscheveld formation and Condroz group are also part of the reservoir formation. Due to the tight matrix of the reservoir rocks, the permeability is believed to be fracture and karst (meteoric and hydrothermal) driven. The goal of this Thesis is to create a static and dynamic model of the reservoir that confirms the current production data (history match) and that explores the development of the geothermal potential of the reservoir in space and time. The static and dynamic reservoir model are based on a limited amount of well and seismic data, which forms the main challenge in this project. A framework of assumptions has been created to construct the model and a scenario-based approach has been applied to construct a best case scenario that matches the production data. A key element in the static reservoir model is the Tegelen fault. To estimate the impact of the Tegelen fault on the permeability distribution in the reservoir, a fieldwork in an analogue carbonate quarry has been executed. The results are applied in the static model. The dynamic results in this study show that the permeability configuration applied in the best case scenario results in BHP, flow rate and temperature values that are of the correct order of magnitude and within an acceptable error margin of the production data. Multiple sensitivities have been simulated to determine the range of parameters that may cause an inaccuracy in the results. Additional data acquisition is necessary to validate and optimize the static model, which will result in a dynamic model with an improved history match and a larger predictive power for future production and reservoir management.

Preface

First of all, I would like to thank my supervisor Prof. Giovanni Bertotti for the guidance, advice and feedback during the past few years. During my entire educational period at the TU Delft, Giovanni Bertotti has taught and guided me through multiple courses and projects. It was a privilege being supervised by him during my Bsc Thesis and Msc Thesis and working together with him in the geoMOOC. Thanks to his critical questions, valuable insights and extensive knowledge on fractured reservoirs, this Msc Thesis has become a success.

I would also like to thank EBN B.V. for this interesting project and great workspace. My gratitude goes out to my supervisors Raymond Godderij and Bastiaan Jaarsma, who provided me with all the necessary advice, knowledge and help. The weekly meetings and daily help were highly beneficial for the progress. Furthermore, I would like to thank Nora Heijnen, who was also closely associated with the project. Without her help, the smooth interaction with the operators and the acquisition of the necessary data for the reservoir model would not have been established. I would also like to thank various EBN employees and interns for thinking along and providing feedback during the project.

My gratitude also goes out to the operators, P. Wijnen and L. Burghout, for providing me with the necessary data for the reservoir model. This reservoir model would not have been as well considered and detailed without the help of TNO and VITO. I would like to thank H. Mijnlieff, K. Geel and R. Fonseca from TNO for their critical views and fruitful discussions. The meeting and cooperation with B. Laenen, V.Harcouët-Menou and M.Broothaers from VITO were also of great importance for thorough understanding of the subsurface in the Californië area.

This Thesis marks the end of my studies at the TU Delft and internship at EBN B.V. It is a summary of 9-months hard work on a very interesting topic. I hope you enjoy readying it.

Dominique Reith
08/2018

Content

List of figures

List of tables

1. Introduction

a. Energy transition in the Netherlands

In the last few years, the energy transition to renewable energy has been set into motion. In September 2013, forty-seven organizations in the Netherlands signed the 'Agreement on Energy for Sustainable growth', which marked the start of the transition to a sustainable future. One of the main provisions in the agreement was an increase of the contribution of renewable energy to the energy mix.
In December 2015, 195 countries signed the Paris Agreement, which was the first global climate deal. The key elements of the agreement incorporated the long-term goal of keeping the global temperature increase below 2 ˚C and limiting the CO_2 emissions (European Commission, sd).
In order to achieve these goals, the Dutch government formulated the goal of reducing the CO_2 emission to practically zero in 2050 in the Energy agenda published in March 2017 (Ministry of economic affairs and climate policy, 2017). To achieve this, the contribution of geothermal energy to the energy mix must significantly increase.

Currently, the geothermal environment in the Netherlands is quickly evolving. In 2007 the first doublet has been drilled and at the end of 2018, the country counts 18 doublets. At this moment, 18 geothermal operators are member of DAGO (Dutch Association Geothermal Operators) and this number keep growing (DAGO, 2018). Since the geothermal sector operates in the same field as the E&P companies, all projects deeper than 500 meter must be approved by the State Supervision of Mines (referred to as 'SodM'). SodM regulates and supervises all projects in order to enforce safety regulations and minimalize potential hazards for the environment (SodM, 2017).

Geothermal wells can be subdivided into two types based on the target depth and the corresponding temperature. The first type is characterized by a target depth less than 4 km, resulting in a temperature of maximum 120˚C (based on the average temperature gradient in the Netherlands of ≈30˚C/km) . The second type is characterized by temperatures above 120 ˚C (SodM, 2017). This category is referred to as 'Ultra-Deep Geothermal wells' (UDG).

To meet the industrial energy demand, the UDG sector must be rapidly developed. To realize this, the 'Green Deal Ultra-Diepe Geothermie' (referred to as "Green Deal UDG") was signed on the 19th of June 2017 by the Ministry of Economic Affairs and Climate Policy (referred to as "EZK"), TNO, EBN and 7 large industrial consortia comprising process industry and partners using industrial waste heat in the Netherlands. In this agreement, the companies agree to share knowledge on the research and use of ultra-deep geothermal energy in the process industry. The aim of the Green Deal is to set-up multiple UDG projects in a foreseeable timeframe (Platform Geothermie, 2017).
The focus of the Green Deal UDG lies on the formations named in Table 1, which are characterized by a high geothermal potential, primarily defined by a suitable primary or secondary permeability and high temperature, because of the large depth.

Period	**Lithostratigraphic formation**
Triassic	Hardegsen Fm., Detfurth Fm., Volpriehausen Fm., Onder Buntsandstein Fm.
Perm	Upper Rotliegend group: Slochteren Fm.
Carboniferous - Dinantian	Zeeland Fm.
Devonian	Bosscheveld Fm.

Table 1. Overview of the geological formations of interest for UDG in the Netherlands (Boxem, Veldkamp, & Van Wees)

b. Thesis objective

The focus of this Thesis lies on the geothermal potential of the Lower Carboniferous Dinantian carbonates. This rock formation is under-explored and the scarce amount of wells that penetrate the layer are clustered along the margins of the NW European Carboniferous Basin (NWECB) in the south of the Netherlands, with the exception of the UHM-02 and LTG-01 well, which are drilled in the north of the country (Reijmer, ten Veen,

Jaarsma, & Boots, 2017). Extensive research on the reservoir characteristics and behavior of this formation is necessary for future development of UDG projects. This leads to the following general Thesis objective:

Verify the potential of the Dinantian carbonates as a geothermal reservoir, by creating a dynamic reservoir model of a Dinantian carbonate reservoir.

The reservoir model in this research project is based on a case study of the Dinantian carbonates encountered in the Californië wells in Limburg. The Californië wells consist of 2 separate doublets and are currently the only geothermal wells producing from the Dinantian carbonates in the Netherlands.
The doublets are located closely to each other and the production wells are drilled towards the Tegelen fault zone. The connection between the injector and producer well cannot be verified and therefore the origin of the produced water is currently unknown. The Tegelen fault zone forms an important component for flow for the producing wells and is thus a key element in the dynamic model. The encountered carbonates are mostly tight, implying insufficient matrix porosity and matrix permeability. Consequently, the permeability is assumed to be fracture and karst driven. In order to estimate the fault zone architecture of the Tegelen fault and resulting reservoir characteristics, a fieldwork in an analogue Dinantian carbonate quarry has been executed.
Based on the case study, a more specific Thesis objective can be formulated:

Create a dynamic reservoir model of the Dinantian carbonates in the Californië area, that confirms the current production data (pressure/flow/temperature) and can explore the geothermal potential of the reservoir in space and time.

VITO (Vlaamse Instelling voor Technologisch Onderzoek) is in charge of the reservoir model on behalf of the operators of the Californië doublets. TNO and EBN performed some separate studies on the static and dynamic modelling of the Californië reservoir. Due to a scarce amount of input data, the interpretation and resulting models differ significantly. In this Thesis, the different interpretations and modelling assumptions will be taken into account and bundled, to create an optimal static and dynamic reservoir model.

c. Case study area

The two Californië doublets are located in the greenhouse area 'Californië', near the village of Grubbenvorst (Limburg, NL).

The first doublet is owned by P. Wijnen (Californië Wijnen Grubbenvorst, referred to as 'CWG') and was drilled in 2012. It consists of 1 injector well (CAL-GT-02) and 2 producer wells (CAL-GT-01S and CAL-GT-03). Both producer wells are drilled into the Tegelen fault zone. The injector is drilled in opposite direction away from the fault zone. In 2013 the injector collapsed and was shut-in. The second producer (CAL-GT-03) was then transformed into an injector. SodM mentions that, in general, the injection of water in a fault zone is possibly related to induced seismicity (SodM, 2017). For this reason the CAL-GT-03 well is closely monitored and regular PLT's are done to check the injection interval. In May 2018, this doublet has been temporarily suspended due to preventive safety measures. This research project will **not** make a statement about the possible seismicity related to CAL-GT-03.

The second doublet is owned by Van Lipzig & Gielen (Californië Lipzig Gielen, referred to as 'CLG') and was drilled at the end of 2015. It consists of 1 injector well (CAL-GT-05) and 1 producer well (CAL-GT-04). Again, the producer well is drilled towards the Tegelen fault zone and the injector in opposite direction away from the fault zone. Both doublets produce water of approximately 75-85 degrees Celsius. From structural point of view, the wells are located in the Venlo block on the north-eastern edge of the Roer Valley Graben, which is part of the Lower Rhine Basin.

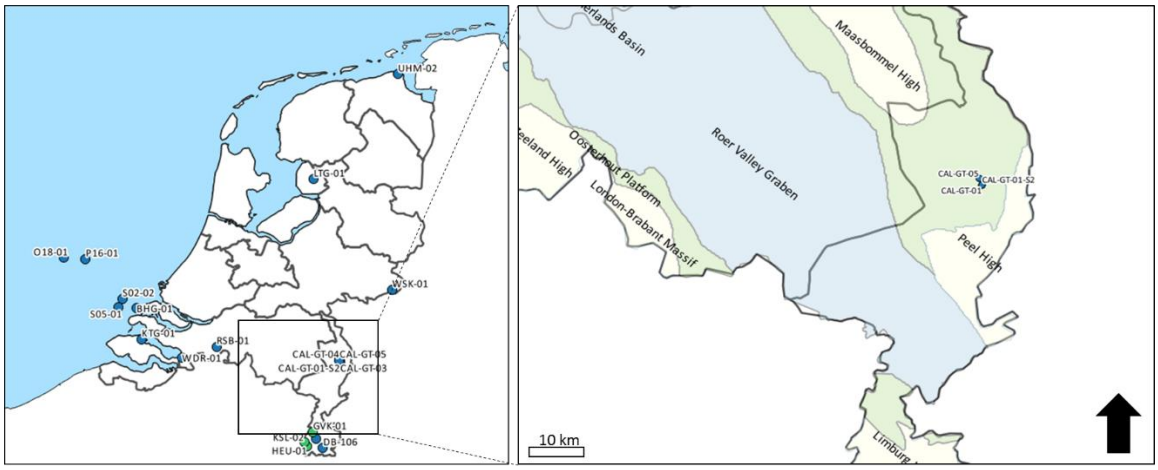

Figure 1. Location of the Californië wells in Limburg (QGIS) (background: Structural elements in the Netherlands, based on (Kombrink, et al., 2012))

d. Thesis outline

Chapter 2 is a literature review of the different geological concepts necessary for the static model and the fieldwork.

Chapter 3, 4, 5 and 6 provide an overview of the different steps in this project; the fieldwork, static and dynamic modelling. Each chapter includes the input parameters, methodology and results of each step.

Chapter 7 is the uncertainty analysis, which summarizes all the uncertainties and corresponding assumptions encountered in the static and dynamic modelling. It also provides recommendations.

Chapter 8 is the discussion. In this section the uncertainties and their implications will be reviewed. Recommendations for future work will be given, with the goal to minimize the uncertainty ranges. A comparison will be made between the different models, made by TNO, VITO and EBN.

Chapter 9 will finalize the report with a conclusion.

2. Literature review

a. Structural geological history

The geological history of NW Europe is characterized by two major orogenies; the Lower Paleozoic Caledonian phase and the Upper Paleozoic Variscan phase (Camelbeeck, et al., 2007). The case study area is located in the southern part of what used to be the North West European Carboniferous Basin (NWECB) (Figure 3). The crust of this basin was initially part of the micro-continent Avalonia. During the late Ordovician, this micro-continent consolidated with Baltica, closing the Tornquist Ocean. The newly found continent (Avalonia/Baltica) collided with Laurentia during the Silurian, resulting in a new continent named Laurussia. The establishment of this continent formed the Caledonian Orogenic Cycle, ending during the early Devonian (Figure 2) (Kombrink, The Carboniferous of the Netherlands and surrounding areas; a basin analysis, 2008). From the early Devonian to the Permian, the tectonic activities were part of the Variscan orogenic cycle. During this orogenic cycle, Laurussia collided with Gondwana and the Gondwana derived micro-continents, closing the Reic ocean, which separated them. The suture between Gondwana and Laurussia is referred to as the Variscan front. The orogeny resulted in the assembly of the super continent Pangea (Kombrink, The Carboniferous of the Netherlands and surrounding areas; a basin analysis, 2008). The Variscan front consists of multiple thrust belts forming different basins. The case study area is located close to the Rheno-Hercynian zone, (van Adrichem-Boogaert & Kouwe, 1993-1997).

The present structural pattern observed in NW-Europe results from post Paleozoic deformation. The Cenozoic rift system, which developed during the late Eocene to Holocene across the Rhenish Shield and Lower Rhine Basin forms the principal influence on the present structures (Camelbeeck, et al., 2007). See Appendix A.1. for the geological timescale.

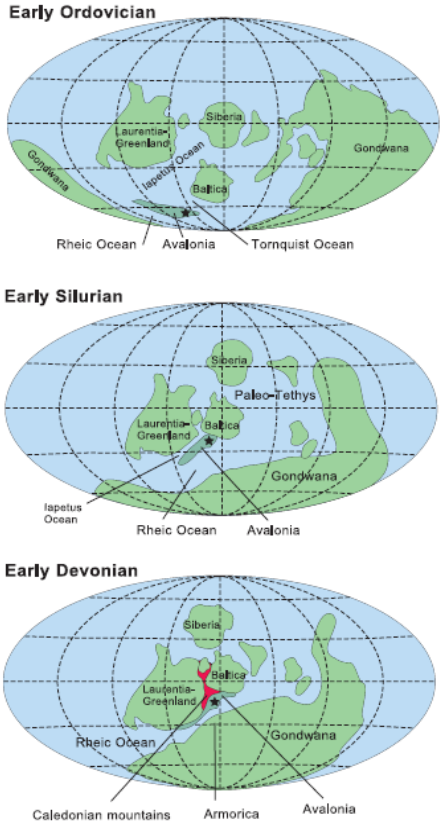

Figure 2. Palaeozoic reconstruction from Early Ordovician to Early Devonian (Caledonian orogenic cycle) (Geluk, Dusar, & de Vos, Pre-Silesian, 2007)

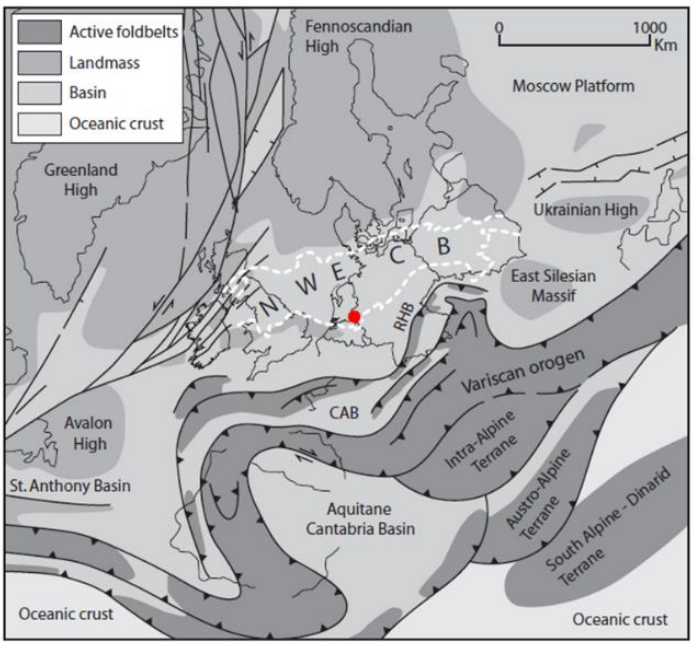

Figure 3. Palaeotectonic map of NW Europe during the Early Carboniferous. The dashed white line indicates the present day contours of the NWECB. RHB: Rhenohercynian basin, CAB: Central Armorican Basin. (Kombrink, The Carboniferous of the Netherlands and surrounding areas; a basin analysis, 2008)

Devonian

Little information is available on the early Palaeozoic geological history in NW Europe. For the NWECB, the late Early Devonian coincides with the opening of the Rhenohercynian rift basin. The structural style during this extensional regime resulted in a series of half-grabens along a series of NW-SE and NE-SW trending faults related to the Caledonian structural weakness (Kombrink, The Carboniferous of the Netherlands and surrounding areas; a basin analysis, 2008). The sediments deposited in the basin sourced from the Mid German Crystalline high in the South and the Old Red Continent in the North (Reijmer, ten Veen, Jaarsma, & Boots, 2017).

The Rhenohercynian rift basin started to close during the middle Devonian due to SE-directed subduction. During the late Devonian a period of back arc extension took place, but this rapidly gave way to a compressive regime in the transition to the Carboniferous (Kombrink, The Carboniferous of the Netherlands and surrounding areas; a basin analysis, 2008).

Early Carboniferous: Dinantian

Throughout the Dinantian, the London Brabant Massif (LBM) formed a stable southern border of the NWECB and a preferential site for the deposition of carbonates. Due to tectonic activity at the end of the Tournaisien, the LBM high underwent uplift, resulting in fracturing and karstification of the carbonates at multiple moments. Consequently, carbonate build-ups developed on the footwall block and the hanging wall blocks were filled by deep water deposits. The end of the Dinantian (Visean) was marked by the closure of the Rhenohercynian zone, which was accompanied by extensive thrusting (van Adrichem-Boogaert & Kouwe, 1993-1997). Due to sea level rise, the intra-basinal carbonate platforms drowned at the end of the Visean (Reijmer, ten Veen, Jaarsma, & Boots, 2017).

The depositional system of the carbonate sequence in the Californië area remains debatable. The absence of deep water facies and biohermal facies in the cuttings of CAL-GT-01S , suggests that the carbonate formation was possibly part of a large carbonate ramp system that stretched from the Netherlands towards Belgium. Post-Visean block faulting resulted in local highs, which were subjected to erosion and karstification (Poty, 2014). A second scenario could be the presence of a local intra-basinal high during deposition, which is characterized by the deposition of carbonates on the footwall block (Figure 4). Both depositional environments explain the thickness differences of the Zeeland formation in the Californië wells.

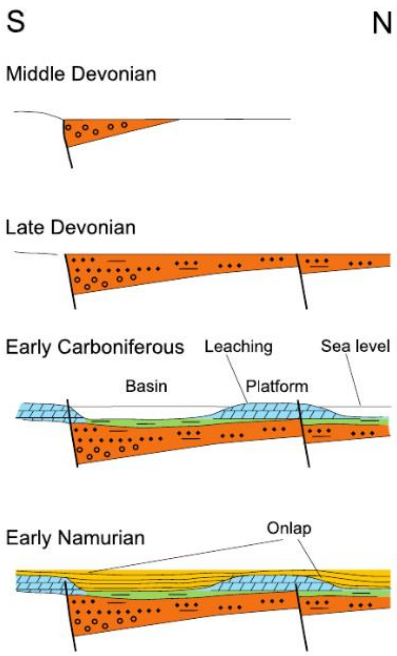

Figure 4. The depositional setting of the Devonian and Lower Carboniferous sediments in the area north of the Brabant Massif. (Geluk, Dusar, & de Vos, Pre-Silesian, 2007)

Late Carboniferous: Silesian

The Silesian consists of the Namurian, Westphalian and Stephanian. The Namurian forms the first part of the Silesian and is characterized by subsidence. Along the southern margin of the NWECB, the subsidence is controlled by thrust loading. In the Netherlands, the Namurian black shales onlap the London Brabant massif and cover the karst surface of the Dinantian, which is represented by a hiatus. In some locations, the Namurian shales are not present and the Westphalian rocks overlie the Visean carbonates (Kombrink, The Carboniferous of the Netherlands and surrounding areas; a basin analysis, 2008). The Northern flank of the London Brabant Massif was a block faulted, WNW-ESE trending plateau (van Adrichem-Boogaert & Kouwe, 1993-1997).
The thermal cooling continued during the Westphalian. Besides the resulting subsidence, the NW-SE striking faults originating from the Caledonian basement influenced the sedimentation. During the mid-Westphalian, the western part of the NWECB was controlled by a N-S compressional tectonic regime. This Variscan inversion event resulted in a series of anticlines in the hanging walls of the basin bounded faults. In the Ruhr area, the Variscan folding started after Stephanian time. The transition from Westphanien to Stephanian is marked by a change in tectonic regime. The Stephanian is characterized by a system of dextral and sinistral wrench faults, which resulted in a series of pull apart basins. The Stephanian sediments have a much wider distribution and are subjected to early uplift in the Permian. This uplift, due to the Asturian phase, caused erosion (Kombrink, The Carboniferous of the Netherlands and surrounding areas; a basin analysis, 2008).

Permian

The compressive movement of the Variscan orogeny ended at the end of the Westphalien. However, the deformation of the Carboniferous carbonates in the Netherlands postdates the Variscan movement and is assigned to the Early Permian wrenching regime. The rifting system and wrenching resulted in a series of different unconformities, bundled together as the Base Permian Unconformity. The Base Permian Unconformity forms the hiatus between the lower Rotliegend and the underlying Namurian or Stephanien deposits. Consequent to the ending of this tectonic phase, a period of non-deposition and regional uplift followed, resulting in erosion. Next, thermal subsidence took place, which lead to the formation of the Northern and Southern Permian Basins. (Geluk, Permian, 2007)

Triassic

The end of the Permian is marked by the withdrawal of the sea from the Northern and Southern Permian Basins, resulting in terrestrial conditions (van Adrichem-Boogaert & Kouwe, 1993-1997). The tectonic setting of NW-Europe during the Triassic is marked by the first movement of the Mesozoic North Sea rift system, which is part of the Arctic-North Atlantic mega-rift system. This rifting system is referred to as the Kimmerian phase and is responsible for breaking up Pangea. It commenced during the late Carboniferous in the Norwegian-Greenland sea. Then it propagated southwards into the north and central Atlantic domains during the Permian and Triassic. In the North Sea, the rifting started during the Triassic, creating the Mesozoic North Sea rift system (Ziegler, 1991). The basins in the south of the Netherlands (West Netherlands Basin and Roer Valley Graben) have a NW-SE strike and are not conform to the E-W direction of extension of the Mesozoic rift system. This implies that these basins follow older structural trends and that the main faults are older faults that are reactivated (de Jager, 2007).

Jurassic-Cretaceous

The Jurassic forms the second part of the Mesozoic rift system. During the Jurassic, the break-up of Pangea commenced along the central Atlantic axis. During this period, Gondwana became separated from Laurasia. During the transition to the early Cretaceous, the tectonic movements of the North sea rift system were governed again by the stress regime of the Arctic North Atlantic rift system (Ziegler, 1991).

The Cretaceous forms the last part of the Mesozoic rift system. After the rifting pulse in the late Jurassic, the extensional movement slowly diminished. Only the master faults bounding the large grabens remained active, resulting in continuous subsidence of these grabens (Ziegler, 1991). At the end of the early Cretaceous, the rifting came to a halt and fault activity ceased. NW-Europe was then subject to thermal subsidence, which is reflected in a large scale transgression. Multiple basins in the Netherlands drowned and the coastline shifted to the Friesland Platform (van Adrichem-Boogaert & Kouwe, 1993-1997). During the late Cretaceous an inversion of tectonic stresses took place, due to the collisional coupling of the Alpine orogenic wedge with its northern foreland (known as the Alpine orogenic system) (de Jager, 2007). The compressional stress regime resulted in an uplift of the basins, which lead to the truncation of the Cretaceous and older sediments (van Adrichem-Boogaert & Kouwe, 1993-1997).

Cenozoic era

In the early Paleogene, uplift of the west Netherlands basin took place, resulting in depositional thinning and erosion of upper Cretaceous chalk and truncation of older sediment. At the end of the Paleogene, thermal subsidence of the North Sea Basin took place simultaneously with a general sea level rise. Parallel to this event clear subsidence in the Roer Valley Graben occurred. The Roer Valley Graben forms the most prominent tectonic feature of the Cenozoic in the Netherlands (Geluk, et al., 1994) .

Roer Valley Graben

In short, the tectonic history of the Roer Valley Graben is characterized by 3 major structural events. Primarily, the Variscan orogeny caused reactivation of the NW-SE and NE-SW trending faults related to the Caledonian Basement, during the Dinantian. At the end of the Silesian, the Lower Rhine basin experienced a N-S oriented compressional regime, overprinting the area with a series of NE-SW oriented anticlines. During the Mesozoic, the Mesozoic North Sea rift system (Kimmerian Phase) reactivated the NW-SE faults. The crustal inversion of the Alpine orogeny resulted in uplift and thus a truncation of sediments. Currently the Roer Valley Graben is part of the Cenozoic rift system, resulting in subsidence along the NW-SE striking faults. (Geluk, et al., 1994) (Wong, Batjes, & de Jager, 2007)

b. Stratigraphy of the Carboniferous and Devonian

The lithostratigraphy of the Carboniferous and Devonian can be subdivided into different sediment groups (Figure 5 & 6). In the Californië wells, the following sediment groups have been encountered: the Limburg group (Silesian, Carboniferous), Zeeland formation (Dinantian, Carboniferous), Bosscheveld formation (Devonian) and Condroz group (Devonian). The Bosscheveld formation includes the Pont d'Arcole, which is a thin shale layer that is also part of the Belgium stratigraphy (Geluk, Dusar, & de Vos, Pre-Silesian, 2007) . The subsections in this chapter provide a description of the Carboniferous and Devonian sediments (information retrieved from nlog.nl).

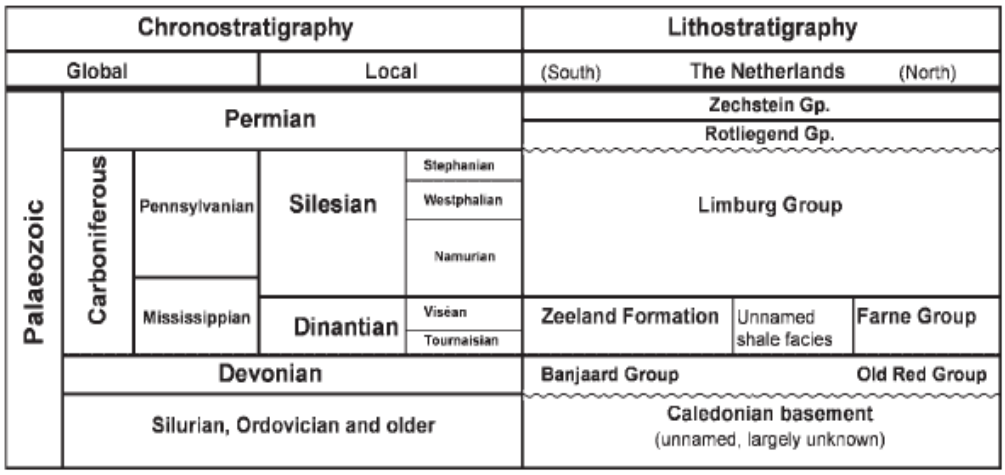

Figure 5. Stratigraphic table for the Upper Palaeozoic era in the Netherlands. Two unconformities present; at base Rotliegend (due to Variscan orogeny), at base Banjaard group (due to Caledonian Orogeny) (Van Hulten & Poty, 2008)

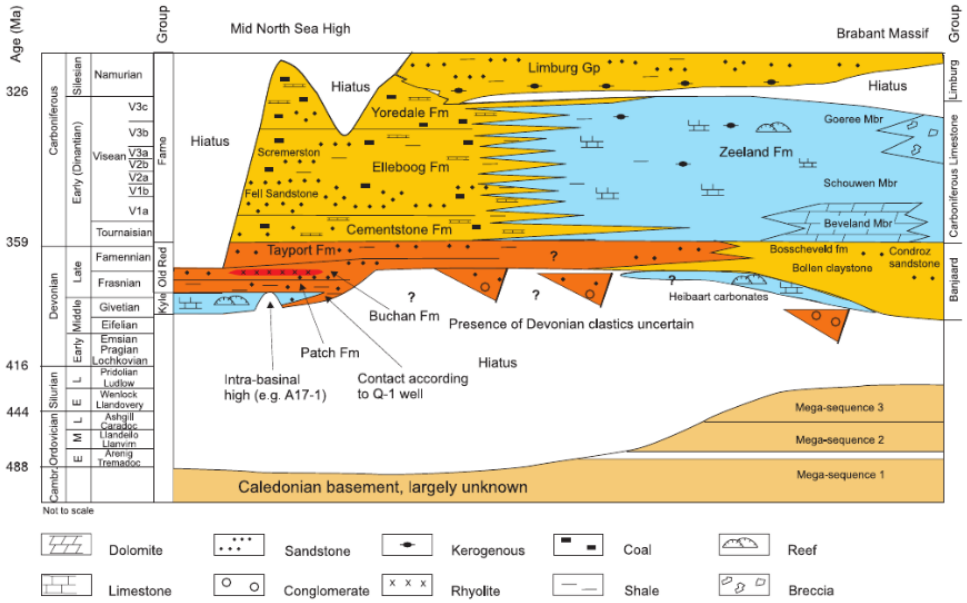

Figure 6. Schematic stratigraphic overview till Lower Carboniferous sediments in the Netherlands (Geluk, Dusar, & de Vos, Pre-Silesian, 2007)

Upper Devonian: Famenian

The Upper Devonian Banjaard Group, deposited during the Famenian, is the only Devonian formation encountered in some wells in the Dutch sector. The upper boundary of the Banjaard group is characterized by a shaly unit called the Pont d'Arcole in the Belgium stratigraphy (Duchesne & al., 2006). This is a greenish, black shale layer intercalated with limestone beds. In the GR-log of the Californië wells it is visible as a sharp increase, compared to the response of the Zeeland formation above. Below the Pont d'Arcole the Bosscheveld

formation is present. The Bosscheveld formation is a transitional unit between the clastics of the Condroz group and the carbonates of the Zeeland formation. The Bosscheveld formation has been deposited in a shallow-marine, low-energy environment and consists of mudstones, fine grained sandstones and limestones. In the south of the Netherlands, the lower boundary of the Bosscheveld formation is formed by the transition to a clastic sediment group. In the Belgium stratigraphy, this sandstone formation is named the Condroz group. The Condroz group can be subdivided in multiple subgroups. The upper group is called the Evieux group.

Early Carboniferous: Dinantian

During the Dinantian, the depositional environment showed variabilities in response to changes in tectonic activity and variations in sea level. Consequently, different types of carbonate mud-mounds were deposited through time (Reijmer, ten Veen, Jaarsma, & Boots, 2017). During the Tournaisien, sedimentation along the southern margin of the London Brabant Massif took place forming carbonate ramps, characterized by Waulsortian build-ups. The build-ups produced an irregular submarine topography (Kombrink, The Carboniferous of the Netherlands and surrounding areas; a basin analysis, 2008). In the basinal areas adjacent to the carbonate platform, thin sequences of shales, bedded cherts and limestones accumulated. The sedimentation in the eastern basinal areas was defined by clastic turbidites originating from the mid German High. On the slope of the platform, the carbonate build ups were alternated with shales from the Goeree member (van Adrichem-Boogaert & Kouwe, 1993-1997). During the Visean, the tectonic activity increased and the depositional system evolved from a carbonate ramp system to a progradational rimmed carbonate shelf. This transition pronounced the contrast between the carbonate highs and basin areas, forming a clear topographic contrast (Reijmer, ten Veen, Jaarsma, & Boots, 2017). In SE-Netherlands, carbonate turbidites from productive shallow platforms formed on the margins of the London Brabant Massif (Kombrink, The Carboniferous of the Netherlands and surrounding areas; a basin analysis, 2008). The entire carbonate deposition sequence during the Dinantian is represented by the Zeeland formation. The Farne group, is the time-equivalent, clastic-dominated sequence, which developed further to the north of the NWECB.

Zeeland formation

This formation is characterized by dark limestones and grey to dark-brown dolomites. The carbonates are often intercalated by claystones and chert beds. The claystones occur mostly in the upper and lowermost parts of the formation. The claystones increase gradually towards the East. In some parts of the Netherlands, the upper part of the Zeeland formation is truncated by erosion, which means that the upper part may be leached and silicified. The top of the formation is characterized by the transition from calcareous deposits to fine clastics of the Epen formation, which is part of the Limburg group. In most places where this transition is drilled, the upper boundary is sharp. The lower boundary of the Zeeland formation is formed by the contact with clastic sediments of the Bosscheveld formation or Devonian Bollen claystone. The former is gradual, the latter disconformable.

Late Carboniferous: Silesian

The Silesian is subdivided into the Namurian, Westphalian and Stephanian. All sediment groups deposited in these subperiods are part of the 'Limburg group'.

The transition from the Dinantian to Silesian is marked by the initial stages of the regression, gradually changing the deep marine environment into delta front environment. During this transition, the sedimentation rates drop and the Namurian shales are deposited (Geul subgroup, containing the well-known Geverik member). The previously uplifted and karstified carbonate platforms drowned and the black shales onlap the London Brabant Massif (Kombrink, The Carboniferous of the Netherlands and surrounding areas; a basin analysis, 2008). The regression continues during the early Westphalian and the depositional cycle now also includes delta-plain swamp deposition (Caumer subgroup). The peat deposition started at the margins of the North-West European basin and slowly expanded into the basin. Later in the Westphalian, the swampy lake sedimentation environment changed into coarse grained fluvial environment. These sandstone successions are part of the Dinkel subgroup. During the last part of the Westphalian, the coarse grained fluvial facies was replaced by fine grained flood plain deposits (Hunze subgroup). The climate became increasingly arid, which reflected in the change of color of the sediments to red-brown.

The depositional environment during the Stephanian remained an alluvial fan system, resulting in a large percentage of sand. The existence of the Stephanien has not yet been established in the Netherlands.

Limburg group

The Limburg deposits reflect an overall regressive deltaic front basin fill. The sediments form a thick, grey to black, fine grained siliciclastic group with intercalating coal seams in the middle and upper part. The group also contains some fossiliferous marine beds in the oldest deposits. Massive, light colored sandstones and red-bed intervals without coal occur in the middle and upper part. The lower most interval consists of black, bituminous shale, with locally some silicified limestone laminae. The upper boundary of the Limburg group is difficult to define, because it is affected by late diagenesis and is unconformably overlain by a younger formation.

The lower boundary is not well known in the Netherlands. However in the south of the country, the Limburg overlies the carbonates of the Dinantian formation.

c. Normal fault zone architecture

The fault zone architecture is important in this project, to understand the impact of the Tegelen fault on the permeability distribution in the tight reservoir rock and thus to understand the production behavior of the Californië wells (Choi, Edwards, Ko, & Kim, 2016). Faults can behave as barriers, conduits or a combined conduit/barrier (Michie, et al., 2014). The most generic fault zone architectural model, described in multiple papers, consists of a fault core enveloped by a damage zone (Figure 7). The fault core is an area of highly localized strain, accommodating the majority of the displacement of the fault (Choi, Edwards, Ko, & Kim, 2016). For faults with a large displacement, the fault core consists of multiple slip surfaces, which is in direct relationship with the width of the core. The fault core is often composed of breccias, cataclasites and gouges, which show little similarity with the host rock. Next to this, the width of the fault core depends on the carbonate lithofacies (Michie, et al., 2014). Strong carbonates localize the deformation, resulting in a thin fault core. In contrary, weak carbonates disperse the deformation, resulting in a wide fault core zone. Also, the fault core has a lower permeability and porosity than the adjacent damage zones (Michie, et al., 2014) (Guerriero, et al., 2013).

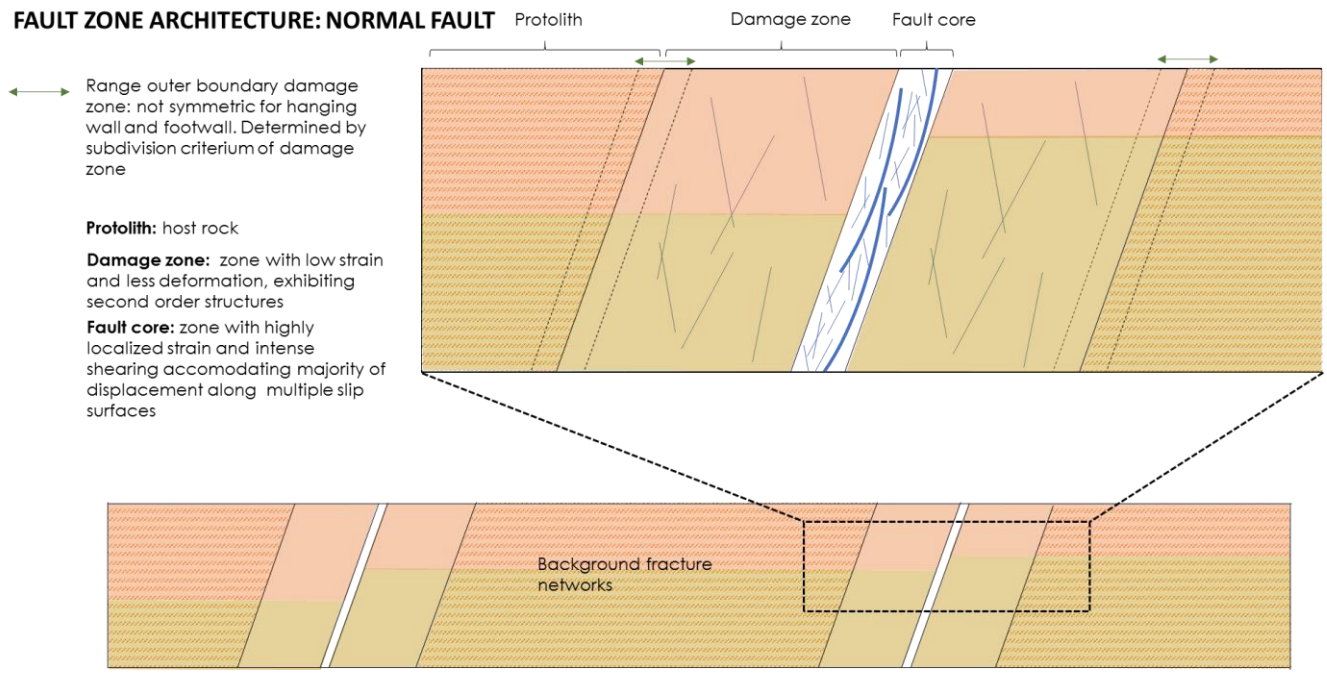

Figure 7. Fault zone architecture (image based on description in multiple papers (Choi, Edwards, Ko, & Kim, 2016) (Michie, et al., 2014) (Berg & Skar, 2005)

The damage zone is characterized by low strain and less intense deformation. The damage zone exhibits second order structures such as fractures, veins and deformation bands. The subdivision of the damage zone and the definition of its total width can be made, based on multiple criteria. The fracture frequency is one of the criteria which is commonly used. The outer boundary of the damage zone is reached when the fracture frequency drops to background level. Applying a specific criteria, a damage zone width can be defined and a scaling relationship between fault displacement and damage zone width can be established. However, these scaling relationships often show scatter, implying that the definition of the damage zone is not the only influencing factor. The lithology of the rock, associated diagenesis, depth of faulting and tectonic environment also influence the positive correlation between the damage zone width and fault displacement (Choi, Edwards, Ko, & Kim, 2016). (Choi, Edwards, Ko, & Kim, 2016) reanalyzed the fault displacement (only normal faults) vs. damage zone width data of approximately 10 studies on sandstones and other tight rocks (including carbonate rocks from the Carboniferous). The plot clearly shows a large range of values for the damage zone width.

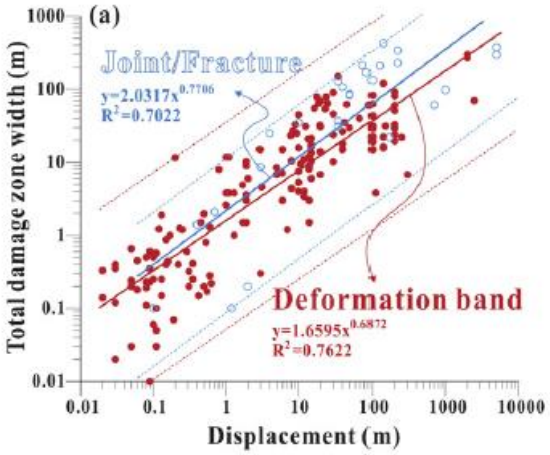

Figure 8. Log-log plot of damage zone width as a function of fault displacement (for normal faults only). Based on studies in multiple types of tight rocks (Choi, Edwards, Ko, & Kim, 2016)

Apart from the damage zone width, the permeability value in the damage zone is also a key element for flow. In general for tight rocks, the permeability in the damage zone is governed by the host rock permeability and the presence of macro-scale fracture networks (which will increase permeability) and deformation/compaction (which will decrease permeability). Both features decrease in frequency with increasing distance from the fault core. In low porosity rocks, the connectivity of the macro-scale fracture networks in the damage zone define the permeability (Faulkner, et al., 2010).
Laboratory measurements have been performed on granite cores to establish the microfracture permeability as a function of the microfracture density in the damage zone (Mitchell & Faulkner, 2012). The micro fracture density in the damage zone decreases exponentially at increasing distance from the fault core, until it reaches the background fracture network density. A decreasing power law function has been defined to calculate the microfracture permeability as a function of microfracture density, distance to fault core and two constant pre-defined coefficients.

The complete fault zone architecture depends on the geological history (i.e. changes in temperature, pressure, stress and strain conditions etc. through geological time), lithology and fracturing and diagenesis that took place under these conditions. Consequently, the architecture can vary spatially and temporarily along the same fault zone. Inclined faults result in an asymmetric deformation pattern, implying variance in stress, strain in the hanging wall and footwall. Consequently, the width of the damage zone can differ in the hanging wall and footwall (Berg & Skar, 2005) (Choi, Edwards, Ko, & Kim, 2016).

d. Karst characterization

One of the reservoir formations of the Californië reservoir is the Zeeland formation, which is a carbonate formation subjected to dissolution. The resulting karst features form an important component for the

permeability distribution in the reservoir and therefore karst characterization is an important concept in this project.

Karst is the removal of material in soluble rocks by physical and chemical dissolution. Salt, gypsum, anhydrite, limestone and dolomite are the primary host rocks for karst aquifers. Physical dissolution implies the flow of pure water along a mineral, which than instantly dissociates. This is the case for the first three minerals (salt, gypsum and anhydrite). For dolomite and limestone, the main dissolution mechanism is chemical dissolution; Carbon dioxide is dissolved in the water and reacts with the water molecule to form carbonic acid. This acid than dissolves the calcium carbonate (Kaufmann, 2016). Karstification is the dissolving of rock, which results in the widening of fissures and cracks, which have previously been created by tectonic movements and weathering. This strongly affects the flow in the subsurface and results in hydraulic heterogeneity (Hartmann & Baker, 2017).

Karst can be subdivided into two fundamental types; epigene and hypogene. Epigene karst, also known as meteoric karst, is characterized by features which are formed by the action of surface water descending into the ground. In contrary, hypogene karst is developed where ascending flow of fluids results in dissolution (Klimchouk A. , 2016). Each of these types occur in specific flow regimes, depending on depth (magnitude of pressure) and degree of hydrodynamic confinement.

Epigene karst systems develop in close interaction with the landscape and have surface and subsurface features. Hypogene karst evolves primarily in the subsurface without direct linkage to the surface. Hypogene karst systems can be overprinted by epigene systems, however, the degree of integration is limited due to large difference in driving forces, organization and functioning of flow (Klimchouk, Palmer, Waele, Auler, & Audra, 2017). The karst surface landforms are characterized by sinkholes, caves, subsidence, sinking streams, springs and caverns. The subsurface landforms are generally marked by areas of dissolution, like enlarged fracture systems, open conduits, caverns and buried sinkholes (Benson & Yuhr, 2016).

In this case study, the area of deposition has been subjected to sea level changes and uplift (Van Hulten & Poty, 2008). For this reason, the karst features in the Zeeland formation can be partly assigned to epigene karst. Next to this, carbonate outcrops in Germany and Belgium show meteoric karst features, such as sinkholes. Indications for similar sinkholes can be seen on 2D seismic lines from the Dutch offshore. The well losses in the CAL-wells can be interpreted as indicators for meteoric karst (Reijmer, ten Veen, Jaarsma, & Boots, 2017).

Hypogene karstification can be subdivided based on multiple criteria. One of these criteria is dissolution mechanism, in which hydrothermal karst forms an important type, often present in the deep subsurface. The patterns and morphologies observed in a karst system are not necessarily specific to one dissolution mechanism. In contrary, the different dissolution mechanisms can show similarities in the effect that they have on the rock. (Klimchouk, Palmer, Waele, Auler, & Audra, 2017).

The endogeneous regime is one of the main flow regimes where hypogene karst occurs. In this regime, fluids originate from metamorphism, devolatilization in the lower crust and magmatic fluids from the mantle and the core. Hypogene karst often occurs along deep rooted faults and carbonate platforms which are open to sea. Mineralization is also often associated with hydrothermal fluid fluxes moving upwards through the crust (Klimchouk, Palmer, Waele, Auler, & Audra, 2017). The analysis of the cuttings from the CAL-GT-01S well show strong indications of diagenetic Dinantian carbonates due to hydrothermal waters rich in calcium sulfate and silica. This has been deducted from the silicified limestones and dolomites affected by dedolomitization (Poty, 2014).

e. Modelling of fractured reservoirs

The permeability in tight carbonate reservoirs is fracture and karst driven. Karst features often overprint the background fracture networks, which results in a heterogeneous porosity and permeability distribution. Predicting the distribution and dimensions of such a heterogenous system remains one of the main issues when modelling a carbonate reservoir. Next to this, the distribution changes in time due to continuous circulation of fluids. This forms the second issue in the application of karst features in dynamic reservoir modelling.

Different approaches haven been developed to model karstified carbonate reservoirs. The more mathematical approaches create a simulation model in which multiple time dependent functions are used to simulate property distribution and flow in a carbonate reservoir in the subsurface.
Other studies focus on the analysis of fracture networks and karst features at the surface. Outcrop data can be combined with well data and seismic attributes, to formulate constraints for geometrical fracture parameters, which can be applied in reservoir scale fracture models (Bisdom, Bertotti, & Nick, The impact of different aperture distribution models and critical stress criteria on equivalent permeability in fractured rocks, 2016). Application of the results in a reservoir model requires that the outcrop is analogue (lithological, geo-mechanical and in terms of burial history) to the subsurface reservoir layer.
For the fieldwork in this Thesis, the latter method is partly used. The subsection below provides a brief summary of this method.

Modelling based on outcrop data

An extensive study on fracture networks and geometry has been executed by a team at the TU Delft. The information in this subsection is mainly retrieved from; (Bisdom, Bertotti, & Nick, An integrated workflow for stress and flow modelling using outcrop-derived discrete fracture networks, 2017) and (Bisdom, Bertotti, & Nick, The impact of different aperture distribution models and critical stress criteria on equivalent permeability in fractured rocks, 2016). The schematic workflow can be found in Appendix A.2.

The necessity of using georeferenced outcrop data to construct geo-mechanical models and flow models lies in the fact that well data cannot capture the spatial and size distribution of 3D fracture networks at larger inter-well scales. Next to this, wells often produce from fracture networks which are below the seismic resolution, which means that seismic reflection data cannot provide any information on fracture network geometry. On the larger scale, it might appear that fracture orientation and intensity are linked to larger structures, like faults. However, previous studies on outcrop data show that on sub-seismic scale, this relationship between regional tectonic history and fracture network characteristics is not necessarily true. The challenges of fracture modelling lie in the acquisition of high resolution data, fracture aperture modelling and permeability modelling.

It is important to notice that rocks in the subsurface have been subjected to different states of stress, compared to surface (outcrop) rocks. Depending on the depth, rocks show varying distribution of properties and display varying organization of fractures. Next to this, outcrop rocks are subjected to weathering and exhumation, which, in case of carbonate rocks, influences the structure. Also, diagenesis must be taken into account. Consequently, the chosen analogue outcrop needs to be picked carefully and the outcrop data can only provide an estimation of the subsurface parameters.

The acquisition of high resolution data forms the first step in the creation of a georeferenced outcrop model. Data acquisition is done using UAV (unmanned aerial vehicle) imagery, which stores the coordinates of each image. The outcrop position is further constrained by using markers, which are also georeferenced with a GPS. The resolution of the images must be as high as possible in order to distinguish the fracture network. Features without color distinction are difficult to trace.

The images captured by the UAV can be processed with photogrammetry. The common points in each image are identified and gathered in a point cloud. The point cloud is then converted into a meshed surface, which can have an equal or lower resolution than the point cloud. The surface is then generated and the model can be exported as a 3D textured geometry to a geological modelling software.

Digifract is a GIS based software which can be used to digitize the fractures in the outcrop model. In order to attain a high level of accuracy, the fractures must be manually traced. Attributes, like infill and orientation, can be added. Having digitized the fractures, the length, orientation and spacing distribution are defined. The fracture density (referred to as ‘P20’, is the number of fractures divided by the outcrop area) and intensity (referred to as ‘P21’, is the cumulative length of the fractures divided by the outcrop area) are calculated and

the fracture spacing distribution can be defined with the box counting method. Outcrops often also contain artefacts, like vegetation, that require manual correction.

Once the 2D fracture network geometry is defined, the fractures can be meshed using unstructured Finite Element meshing . The meshing and geo-mechanical simulations can be done in ABAQUS CAE, which is a software that resolves the local stress state. The fracture aperture distribution can be determined using a stress-aperture relation that calculates the aperture of each fracture. Four different aperture definitions can be implemented: Power law scaling (predicted by Python function in GIS environment), sublinear and linear length aperture scaling (predicted by LEFM) and Barton-Bandis conductive shearing (derived from FE model or geometrical model).

(Bisdom, Bertotti, & Nick, The impact of different aperture distribution models and critical stress criteria on equivalent permeability in fractured rocks, 2016) provides a more detailed explanation of the different stress-aperture relations. The most realistic approach is the Barton Bandis conductive shearing approach, which assumes that each fracture has an intrinsic roughness that prevents it from closing. This means that it can be used to predict apertures of fractures that have irregular walls and experience shear under compression. The aperture in this approach is quantified using a set of empirical functions based on normal stress and shear displacement.

These models define the mechanical aperture. This aperture results from in situ stresses and does not necessarily contribute to flow. Fractures only contribute to flow when they are hydraulically open, which only occurs during a critically stressed condition. The hydraulic aperture is the opening that controls fluid flow and is equal or smaller than the mechanical aperture.
The next step involves the calculation of the equivalent permeability, which incorporates the flow through matrix and fractures. The matrix permeability is often taken as a constant and the fracture permeability can be derived from the hydraulic fracture aperture through the cubic law. Even if the fractures are disconnected in an initial setting, flow can still occur through the matrix. The percolation probability is the ratio of the number of fracture intersections divided by the number of fractures. It is used as a measure of connectivity and records the scatter in permeability when fractures are the only feature that contribute to permeability.

3. Fieldwork

a. Methodology

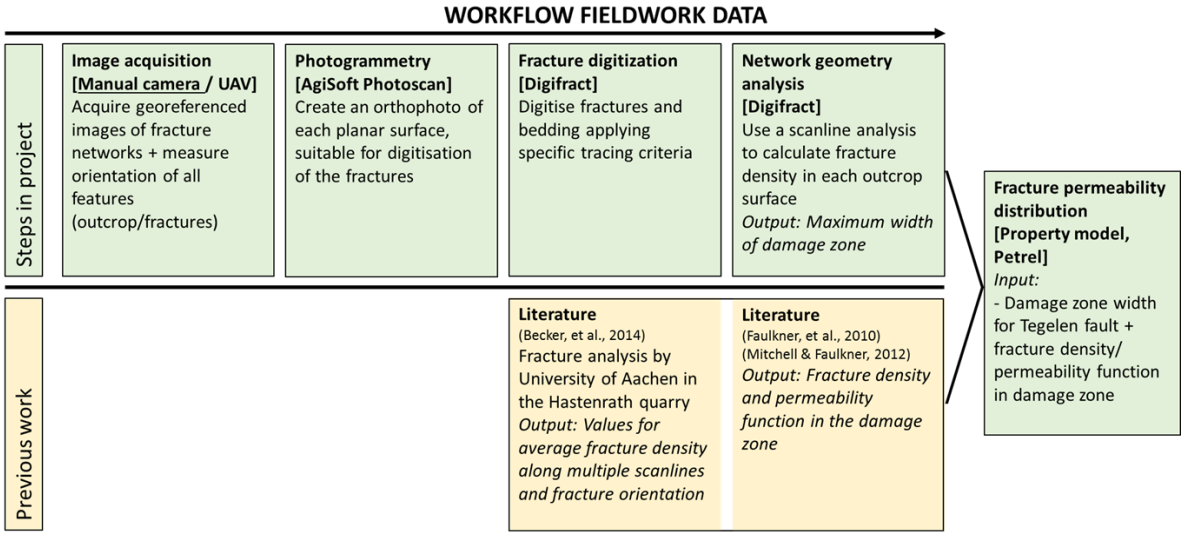

Figure 9. Workflow used in this study for analyzing fracture networks based on outcrop surface data

The main goal of the fieldwork is to obtain an overview of the fault zone architecture of the Tegelen fault. More specifically, a *maximum* width of the damage zone has to be established, in order to distribute the fracture density and corresponding permeability correctly in the property model in Petrel.
The maximum width can be defined by analyzing the average density of fracture networks with a scanline analysis on multiple outcrop surfaces in an analogue quarry.

Data acquisition has been done in the Hastenrath and Brees quarry in Germany, which are assumed to be analogue to the Californië wells (see Chapter 3b). The Hastenrath quarry is located adjacent to the Sandgewand fault and both quarries are located close to the fold axis of the Hammerberg anticline (Figure 10).

Digifract (TU Delft software) is used to trace the fractures observed on the photographs of each outcrop surface. Since the Hastenrath and Brees quarry are currently active, the fractures and mining effects are not easy to distinguish from each other. To compare the fracture network density from different outcrop surfaces, similar fracture tracing criteria are applied. The following tracing criteria have been set:

1. Analyze photo of outcrop surface at one specific scale
2. Trace fracture along fault trace
3. Only trace what is visible
4. Only trace straight lines

Figure 10. Location of the Hastenrath and Brees quarry. The yellow lines indicates the structural features. (Source background image: TIM-online (Bezirksregierun Köln, n.d.))

Due to unfortunate technical and weather conditions, the image acquisition was hampered severely. The UAV (drone) did not work sufficiently, so the manual camera was used. Consequently, appropriate outcrop surfaces at large heights could not be captured. Also, a manual camera is not automatically georeferenced, which causes an inaccuracy in the scaling of an image.

b. Analogy to Californië wells

The Californië wells are located close to Venlo (Limburg, NL) and the quarries are located close to Aachen in the Stolberg area (east of Germany). The quarries must be comparable in terms of lithology and structural history, in order to extrapolate data from one location to the other.
In terms of lithology, the carbonates encountered in the Californië wells and in the Hastenrath quarry belong to the same system (carbonate platform system) (Geel, 2017) (Becker, et al., 2014) (Poty, 2014).

From structural point of view, the quarries and Californië wells are both located at an edge of the Roer Valley Graben. The Tegelen normal fault, visible in the Californië wells, has a NW-SE strike, large offset (>100m) and is located at the NE-edge of the Roer Valley Graben. This fault is comparable to the Sandgewand fault, which is also a normal fault with a NW-SE strike, large offset (>100m) and part of the SW-edge of the Roer Valley Graben (Becker, et al., 2014). The Hastenrath quarry is located adjacent to the Sandgewand fault.

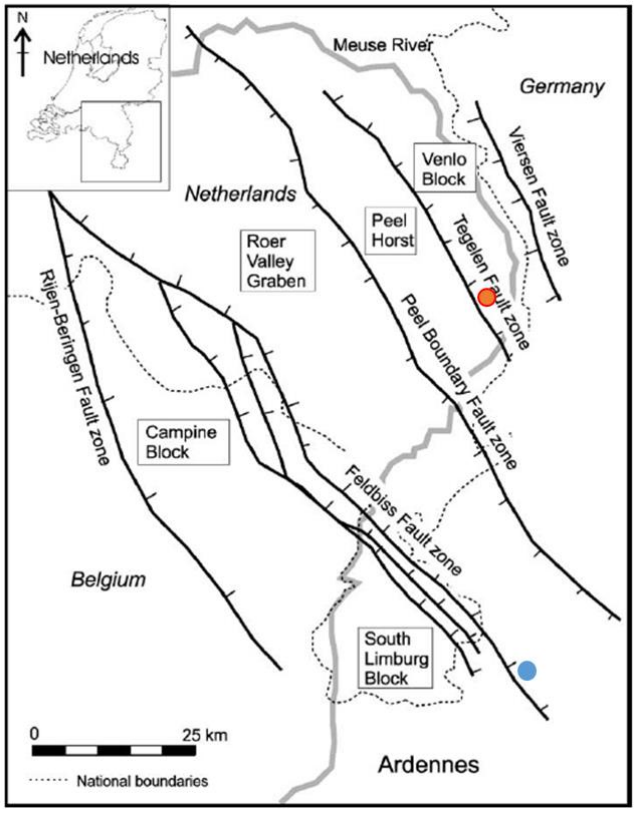

Figure 11. Tectonic features of the Lower Rhine Basin. The blue dot indicates the Hastenrath/Brees quarry and the red dot the Californië wells (Houtgast, Van Balen, Bouwer, Brand, & Brijker, 2002).

The series of events in the geological history of the Roer Valley Graben is important when defining the contribution of the different orientated fracture sets to the permeability in the reservoir. The Californië wells are located at a larger distance from the Variscan front, which means that folding related features are present in less extent than in the quarries.

The FMI results of well CAL-GT-01S (ran in the top part of the Zeeland formation) shows that the bedding has a NS-strike and dips West with a mean dip angle of 22 degrees. The interpreted faults and micro-faults have a WNW-ESE to E-W strike and dip NE and SW with a mean dip angle of 87 degrees (Appendix B.1). The strike of this set is parallel to the Tegelen fault and most likely related to the rifting events in the Roer Valley Graben.

The fracture orientation study in the Hastenrath quarry proves that the two main fracture sets show the following strike orientations: NE-SW and NW-SE. The NW-SE trending set shows NE and SW dipping angles between 50 and 85 degrees. The fracture intensity increases in the direction of the Sandgewand fault. The NW-SE fracture set can be associated to the compressional regime of the Variscan orogeny or to the extensional regime of the different rifting events.
Minor faults are recognized in the Hastenrath quarry, which are aligned with the Sandgewand fault. The minor faults show a late strike-slip movement, postdating the down-slip movement, suggesting that the Sandgewand fault might also have a late dextral strike-slip movement. A cross section shows that the Hastenrath quarry is located on the northern flank of the Hammerberg anticline, which has a NE-SW orientation. The Brees quarry is located on the southern flank of the same anticline (Becker, et al., 2014).

Based on the assumption that the Californië wells and Hastenrath quarry both show carbonate platform deposits and NE-SW strike fracture sets, it can be concluded that the carbonate formation present at both locations has been deposited in a similar time frame under similar conditions. However, the burial history is partly different. This means that the assumption concerning the analogy of both locations includes an uncertainty. For the Brees quarry, the analogy with the Californië wells cannot be determined as specifically as

for the Hastenrath quarry, because the lithology and fracture orientations within the quarry have not been studied as extensively. However, the Brees quarry is located at approximately 9 km from the Hastenrath quarry and practically in the same structural setting. The quarry also shows NW-SE trending faults and fractures, which is for now regarded as sufficient information to establish the possible analogy.

c. Data acquisition

In this study, data acquisition has been done in the Hastenrath and Brees quarry. The images below show a top view of each quarry, with the red dots indicating the location of the analyzed outcrop surfaces. To capture the variation in fracture density, the outcrop surfaces must be located at varying distance from the Sandgewand fault.

Figure 12. Map view of the Hastenrath and Brees quarry (background image from Bing maps, analyzed in Digifract)

The Hastenrath quarry presents multiple fracture sets with different orientations. In order to capture the NW-SE oriented fracture set, which is also visible in the FMI of CAL-GT-01S, the analyzed outcrop locations in the Hastenrath quarry must satisfy the following criteria:

1. The outcrop surface must be perpendicular to the Sandgewand fault
2. The outcrop surface must be as vertical and flat as possible
3. The outcrop surface must contain the least amount of artefacts (areas covered by rubble/vegetation etc.)

The Hastenrath quarry has 7 outcrop surfaces with varying dimensions. Only HAS2 is an orthophoto made in Agisoft, the other outcrop surfaces are analyzed based on photographs, scaled with markers included on the photograph. The Brees quarry has 2 outcrop surfaces with varying dimensions. Both outcrop surfaces are located on the same orthophoto. Appendix B contains the photograph of each outcrop surface.

d. Results: Scanline analysis

The scanline analysis in Digifract is performed for each outcrop surface and provides a value for the fracture density (and standard deviation), the average spacing of the fractures (and standard deviation), the length of the scanline and the number of intersects along each scanline.

The scanlines are perpendicular to the track line, which means that they are approximately parallel to the bedding (Appendix B.6). Figure 13 shows one of the walls in the Hastenrath quarry, on which several outcrop surfaces have been analyzed.

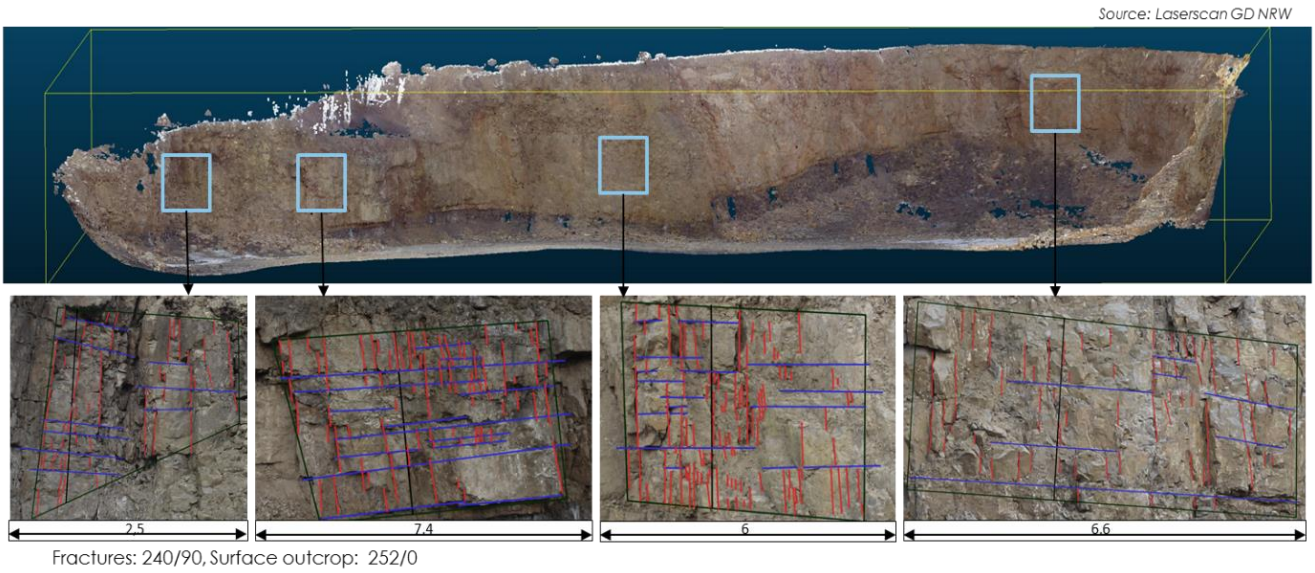

Figure 13. Laserscan image (source: Mathias Knaak, from GD NRW) of wall in Hastenrath quarry with 4 analyzed outcrop surfaces (left to right: HAS6, HAS3, HAS4 and HAS5)

Figure 14 shows the results of the scanline analysis for the HAS5 surface outcrop. The fracture density plot (yellow line) shows varying values across the outcrop. The fracture density is small along the bedding planes, which means that these planes form a boundary for fracture propagation. The results of the scanline analysis of each outcrop surface can be found in Appendix B.7 till B.11.

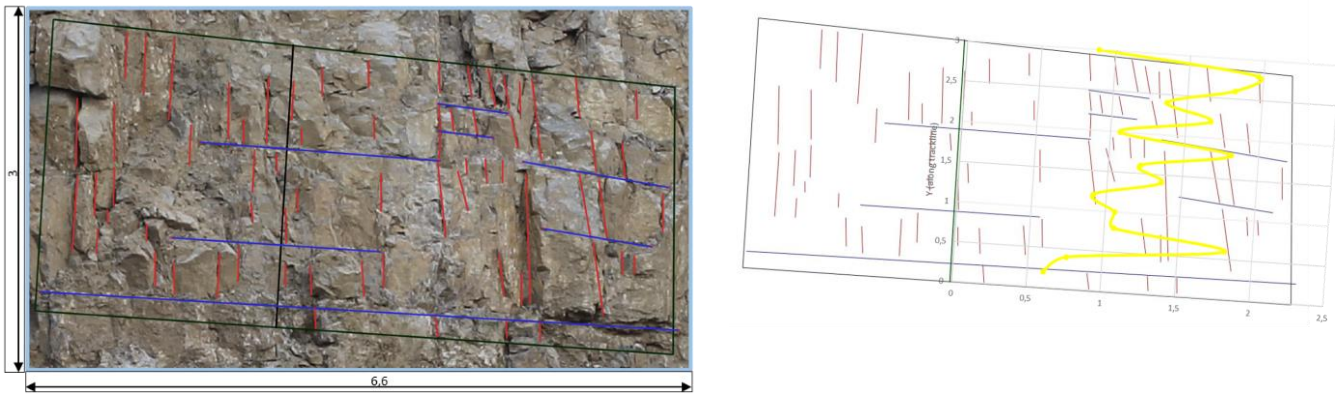

Figure 14. Scanline analysis HAS5 (red = fractures, blue = bedding planes, green = trackline, yellow line = fracture density plot).

The resulting fracture network density in each outcrop is summarized in the figure below. It becomes clear that all measured densities lie between 1 and 2,2. This is not significantly different, suggesting that all measured outcrops are located in the background fracture network and not in the damage zone of the Sandgewand fault. This means that the distance between the Sandgewand fault and outcrop HAS2 is the maximum damage zone width, because this outcrop is located closest to the Sandgewand fault. This distance is 80 meters. Important to notice is that this conclusion is only valid if we assume that the Sandgewand is the only major fault in the area with a distinctive damage zone.

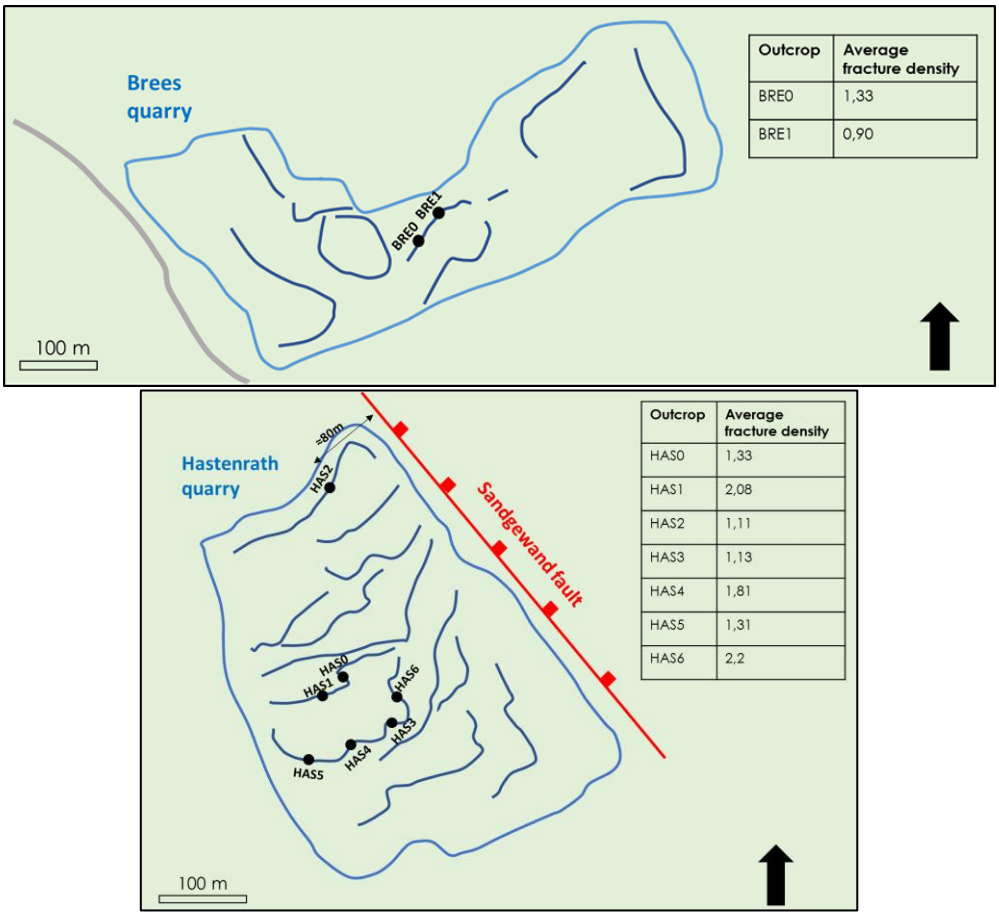

Figure 15. Overview of the calculated fracture network density in Hastenrath and Brees quarry

However, analyzing the results of (Becker, et al., 2014), it becomes clear that the damage zone of the Sandgewand zone is probably much thinner and has a value of approximately 35 m. This estimation is based on the measured fracture density along scanlines close to the fault core and an exponential declining function calculating fracture density in the damage zone (Mitchell & Faulkner, 2012). Further explanation can be found in Appendix B.12.

As previously mentioned, multiple minor faults have been observed in the Hastenrath quarry, parallel to the Sandgewand fault (Becker, et al., 2014). The measured outcrop surfaces are located between these parallel faults. The question arises whether these parallel faults are also part of the damage zone of the Sandgewand fault or if they are individual faults and their damage zones are barely visible due to their small offset. Both scenarios can be implemented in the Petrel model by varying the permeability distribution.

4. Static model

a. Input data

Seismic and well data

The input data for the static model consists of two 2D seismic lines shot in 2010 (09-01_crs_PostSTEM_fisc and 09-02_crs_PostSTEM_fisc), well log data of all wells (CAL-GT-01S, CAL-GT-02, CAL-GT-03, CAL-GT-04, CAL-GT-05) and the results of the fieldwork. Appendix C.1 provides a detailed overview of the available well data. Figure 16 is a top view of the two seismic lines and the wells. It shows the location of the seismic lines and the zoom window shows that the wells are not located on the seismic line. Next to this, the well trajectories are deviated. A combination of these two factors forms the main uncertainty in the seismic interpretation.

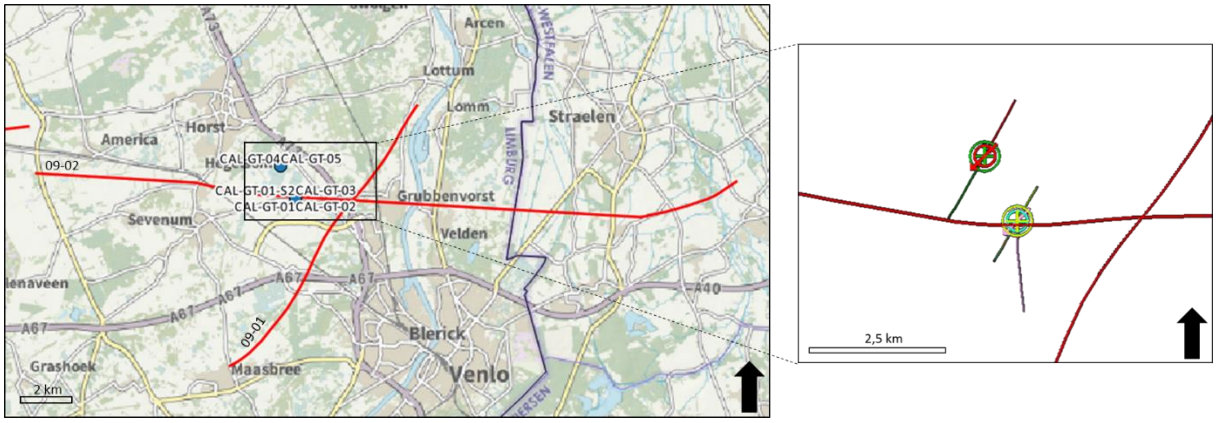

Figure 16. Top view of the two 2D seismic lines and wells (Petrel)

Well design

The tables in Appendix E.1 provide the well design for each well. CAL-GT-03 is naturally obstructed at 2390 MD, and no flow occurs below approximately 2100 meter MD, therefore a plugback at 2100 meter (MD) depth has been included in the model to prevent flow in deeper layers. The spud date has been used in Petrel as reference date for the completions. Well CAL-GT-01S and CAL-GT-05 produce/inject in an open hole section, the other two wells have perforations.

b. Methodology

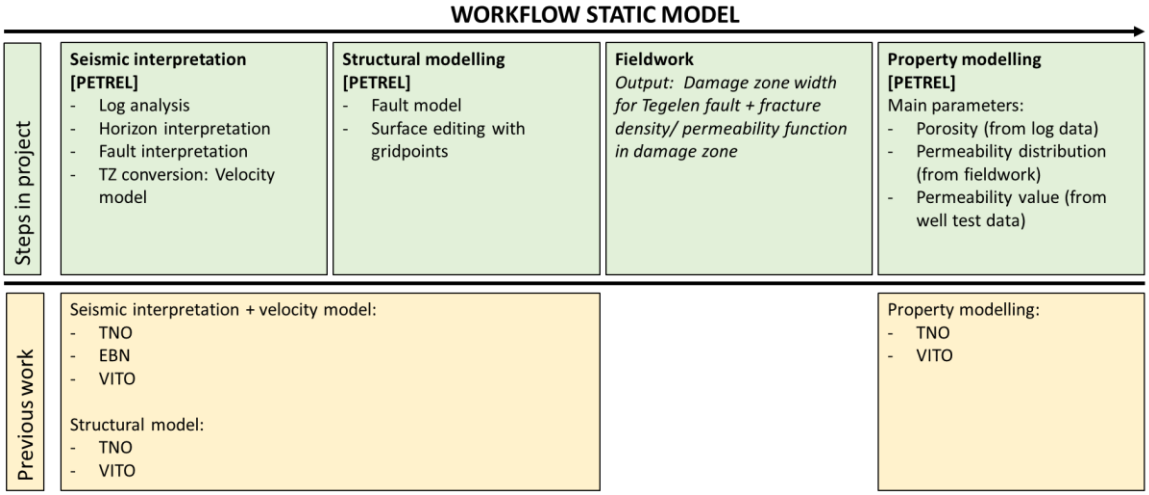

Figure 17. Workflow used in this study for the static modelling

The workflow for the static model is straightforward; well top identification based on logs, seismic interpretation, time-depth conversion, structural modelling and property modelling.

The challenge is the lack of well/log data and seismic data. Consequently, a large set of assumptions and hypothesis is necessary to estimate the missing geological parameters and create a static model that estimates the reservoir geometry as good and realistic as possible.

Well top identification

The well top interpretation is based on the Gamma Ray log (GR-log) and Litho-log. The latter provides an indication of the encountered lithology, based on the cuttings returned during drilling.

Seismic interpretation

The seismic interpretation of the horizons and faults in this Thesis are based on the interpretation of M. ter Borgh (EBN B.V.). This interpretation is based on high amplitude seismic reflectors, because a well-to-seismic tie is missing. The corresponding interval velocity is used as a check to verify the chosen seismic reflector in a qualitative way.

The seismic data in this project is shot in SEGY-convention, however, the *NON-SEGY convention* is used in Petrel. This implies the following;

- **Hard kick** = increase of acoustic impedance = positive value
- **Soft kick** = decrease of acoustic impedance = negative value

Velocity model

The velocity model consists of fixed interval velocities in a layer-cake model. The Californië wells do not have a check-shot or VSP to construct a velocity profile, so the fixed interval velocities are derived from pseudo-velocities and sonic logs from offset wells.

It is important to notice that a fixed interval velocity is not accurate for a formation that is affected by exhumation and compaction. At increasing depth the effective pressure on the rock matrix increases, which influences the pore properties. These are directly related to the seismic interval velocity. However, for simplification, a fixed interval velocity for all formations will be applied in this model. For the NSG, Chalk and Trias this assumption will not result in a large inaccuracy, because the formations are located at a relative shallow depth and have a small thickness. In contrary, the Limburg and Zeeland formation are located at large depths and have a variable thickness, which means that a fixed interval velocity will result in an inaccurate depth conversion.

For the top three horizons (Base NSG, Base Chalk and Base PU), the picked seismic reflector is assumed to be relatively accurate. Consequently, the interval velocity is based on a pseudo velocity, which is derived from seismic picks on the seismic line 09-02. The formula below is used to calculate the interval velocity. The interval velocity for a specific horizon is the average of the calculated values in each well.

$$Vint = \frac{\Delta Z * 2}{\Delta TWT} \qquad (1)$$

The interval velocity for the Limburg and Zeeland formation cannot be based on seismic picks, because the formations are dipping and the wellbore projection is inaccurate along the deviated part of the well trajectory. Instead, the interval velocity has been derived from the sonic velocity of offset wells.

An uncertainty is incorporated in this method, because a sonic velocity is not exactly equal to the seismic velocity. The sonic velocity is derived from the acoustic travel time, which is measured in the borehole by pulsing sound at a specific frequency into the subsurface. In contrary, the seismic velocity is derived from a VSP, which is created by placing a source with acoustic pulses at the surface and geophones in the wellbore. The difference in source frequency and source geometry forms one of the main reasons for differing velocities (Stewart, Huddleston, & Kan, 1984).

Structural model

The Base Bosscheveld and Base Condroz are added in the structural model. The surface of each horizon in the structural model is based on only two seismic lines. Consequently, the result shows some discrepancies with the actual structural geometry of the subsurface. For example, the Tegelen fault becomes a reverse fault, whereas the seismic lines clearly show a NE dipping normal fault. This is solved by creating additional grid point sets for each surface, to manipulate the positioning. The depth value of the grid points are based on the values observed on the seismic lines and the well tops (Appendix C.8) . In this study, the following assumptions are made for the structural modelling:

1. All structural and stratigraphic features follow the NW-SE striking orientation of the Roer Valley Graben, which is continuous in all directions in the entire Petrel model.
2. The structural high/platform geometry is present in all formations and has a constant thickness (different for each formation).
3. The Tegelen fault is a normal fault.

However, the geometry and spatial development of each formation between the seismic lines and wells cannot be defined with great confidence with the currently existing data. Additional 2D or 3D seismic data is necessary to define to what extent each formation is continuous.

Property model

In the property model, the reservoir parameters are distributed in the model. The following assumptions are applied in this study:

1. The reservoir consists of the Zeeland formation, Bosscheveld formation and Condroz group. The Limburg group and Pont d'Arcole are assumed to function as a seal and do not contribute to flow.
2. All formations are homogeneous, which means that each formation is assumed to be a single facies and is described by a single value for each property (except permeability).

The porosity of the formations is calculated with the Wyllie equation, which is based on the sonic log (available for CAL-GT-01S) and the shale volume, which is derived from the GR-log.

$$Wyllie\ Eq: \varphi = \frac{DT_{ma} - DT - V_{shale}(DT_{ma} - DT_{sh})}{DT_{ma} - DT_{fl}} \quad (2)$$

φ = porosity
DT = interval travel time (ma = matrix, sh = shale, fl = fluid)
V_{shale}= shale volume

The N/G, Sw and Vshale values are based on the distinction between reservoir and non-reservoir formation.

The permeability is dependent on the fault zone architecture of the Tegelen normal fault, which forms the main conduit for flow in the production wells. The results of the fieldwork are applied in this step, because they provide an estimate for the maximum damage zone width.
Multiple scenario's for permeability distribution are created in the upscaled structural model. The permeability function within the damage zone is based on literature. The value for background fracture network permeability is deducted from the well test data.

During permeability modelling two important assumptions are applied:

1. All reservoir formations (Zeeland fm., Bosscheveld fm. and Condroz group) are regarded as one single reservoir displaying a homogeneous distribution of permeability features
2. The reservoir model is regarded as a single porosity system. The matrix of the reservoir rocks is tight and not contributing to flow. This means that all the permeability is fracture and karst related.

c. Results: Well top interpretation

Six different horizons have been identified on each log; Base North Sea Group (Base NSG), Base Chalk, Base Permian Unconformity (Base PU), Base Limburg, Base Zeeland and Base Bosscheveld (well section in Appendix C.2).

The stratigraphic column is characterized by two hiatus, one at the base of the chalk (horizon: Base Chalk) and one at the base of the Zechstein (horizon: Base Permian Unconformity). The base Chalk is a disconformity, because multiple lithological formations are missing. The hiatus at the base Zechstein is an angular unconformity; the Zechstein is underlain by the tilted and truncated Limburg formation.

In the 'Basisregistratie' ("BR") (Registration of all onshore and offshore Dutch wells) the stratigraphy of each well has been noted with the corresponding well tops. The well top for Base North Sea group, Base Chalk and Base Permian Unconformity are deducted from BR. The well top of the deeper formations had to be re-interpreted. The following criteria have been applied for the identification of the deeper well tops:

1. Base Limburg: This is a transition from claystone to carbonates. The well top has been set below the transition zone, when the carbonates form the majority in the returned cuttings. This is characterized by a low GR signal.
2. Base Zeeland: This base is marked by the presence of the Pont D'Arcole shale layer. The well top is set where the GR significantly increases in value.
3. Base Bosscheveld: This base is marked by the presence of the first clastic, which can be defined on the Litho-log.
4. Base Condroz: Not encountered.

The resulting values are listed in the table below. For the Base Limburg, the implementation of the well top criteria leads to values that correspond to the BR values. In contrary, the base Zeeland value differs for well CAL-GT-01S, CAL-GT-02 and CAL-GT-03. The Base Bosscheveld and Base Condroz are not encountered according to BR in well 01S/02/03.

Table 2. Well tops in Californië wells (Reference level = NAP)

The well tops show that the Zeeland formation has a variable thickness. This is related to the structural setting during deposition (described in Chapter 2a) and post depositional faulting. The latter could result in a fault cut-out in CAL-GT-03, which is a possible reason for the small Zeeland formation thickness in this well.

Identification of reservoir intervals

The completion of the wells suggests that the reservoir consists of the Zeeland formation, Bosscheveld formation and Condroz group. CAL-GT-01S produces with an open hole completion from the Zeeland formation, Bosscheveld formation and Condroz group. CAL-GT-04 is perforated over a large interval covering the Bosscheveld and Condroz formation. The porosity, calculated from the sonic log, confirms that all reservoir rocks are tight. The loss zones identified in the EOWR are the main reference for the identification of the production zones, which are characterized by a higher permeability, related to fracturing and karst features. Next to this, the FMI and caliper in CAL-GT-01S and the PLT in CAL-GT-03 and CAL-GT-05 are useful.
The figure below provides an overview of the wellbores (flattened on base Limburg) with the encountered losses and the observations in the FMI log, caliper log and PLT (depth in TVD). The main conclusion from this figure is that the Zeeland fm., Bosscheveld fm. and Condroz group all show signs of high permeable regions and can therefore be regarded as a reservoir formation.

Figure 18. Overview of the losses in each wellbore based on EOWR, Caliper, FMI (only CAL-GT-01S) and PLT (only CAL-GT-03 and CAL-GT-05).

d. Results: Seismic interpretation

Horizon interpretation

The seismic character of each horizon is necessary to identify a seismic reflector. In this study, the following seismic characters have been used;

Horizon	Seismic character (Soft/Hard kick)	Reasoning
Base North Sea Group	Hard	Transition from siliclastics and clays to chalk
Base Chalk	Soft	Transition from chalk to sandstones/ claystones
Base Permian Unconformity	Soft (*)	Transition from siliclastics/marl to claystones
Base Limburg	Hard	Transition from claystones to limestone/dolomite
Base Zeeland	Soft	Transition from limestone/dolomite to shale (Pont d'Arcole)

(*=The Base PU is characterized by a mix of different lithologies; transition can be soft or hard kick. Marl to claystone is a soft kick)
Table 3. Seismic character for each horizon in the Californië model

The wells are projected along a 135 degrees azimuth onto the seismic line, which is conform to the regional NW-SE structural trend. However, the well trajectories are deviated, which means that the projection of the wells onto the seismic line does not provide an accurate positioning of the deeper well tops with regards to the seismic reflectors (no well-to-seismic tie).

The top three horizons (Base NSG, Base Chalk and Base PU) are horizontal and located in the vertical part of the well. This means that the identified well top provides a rough indication for the corresponding seismic reflector. In contrary, the base Limburg and base Zeeland are purely based on seismic reflector amplitude.

The Limburg formation onlaps the Zeeland formation and can be clearly distinguished on the seismic line. The high amplitude reflectors within the Limburg formation can be assigned to the presence of coal seams, dating from the late Westphalien. The heterogeneous Zeeland formation is characterized by bright amplitudes, which can be related to karst features. The Base Limburg (=Top Zeeland) horizon is clearly recognizable if this interpretation is applied.

The reflector for the Base Zeeland cannot be accurately traced, because the transition to the Bosscheveld formation is debatable and the seismics are diffuse and chaotic.
The Bosscheveld formation and Condroz formation are not clearly distinguishable on the seismic lines and for this reason these horizons are not interpreted. They will be added in the structural model.

The figures below show the seismic interpretation of the 09-02 line. The seismic interpretation of the 09-01 line can be found in Appendix C.3.

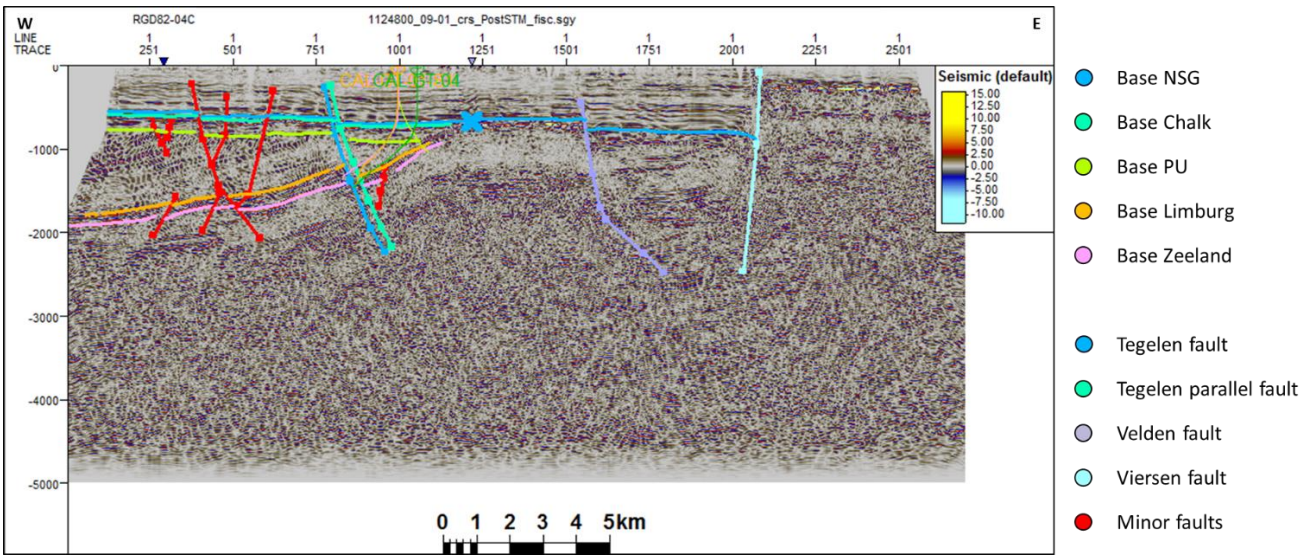

Figure 19. Interpretation of the 09-02 seismic line including all interpreted faults

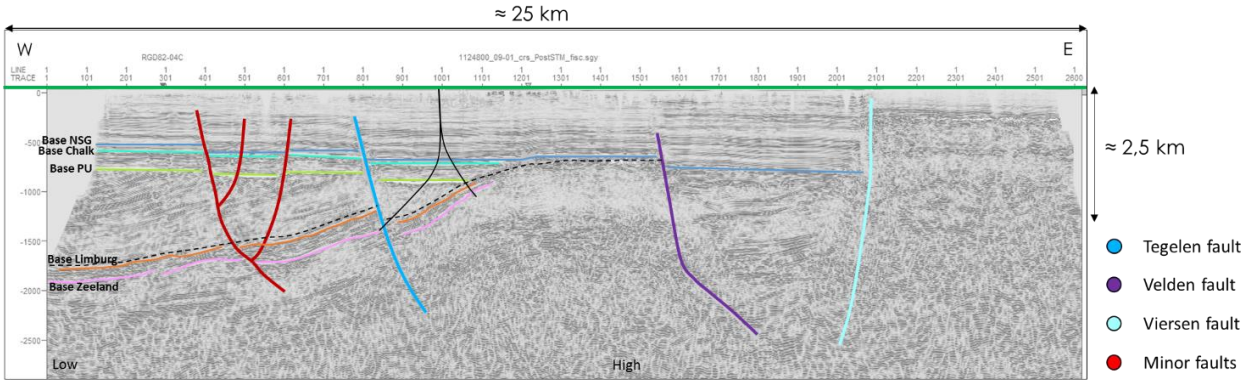

Figure 20. Simplified interpretation of 09-02 showing the conceptual model of the subsurface.

Fault interpretation

Both seismic lines show multiple large and small offset faults. Only the Tegelen fault and Velden fault are incorporated in the fault model, because these are the only two faults which are clearly visible on both seismic lines. The Tegelen 'parallel' fault is also traced on both seismic lines. This fault possibly exists, because the reflectors trail off at the end. However, this can also be due to the fact that the seismic line is not shot perpendicular to the fault.

From the structural geology of the Roer Valley Graben it is clear that the main fault orientation is approximately NW-SE. Recent studies have analyzed and interpreted 3D seismics in the Carboniferous at various locations in the Netherlands. The 3D seismics in the Northern North sea, Tilburg/Waalwijk and Doetinchem/Zutphen all showed a fault trend with a ESE-WNW strike (named "110"-trend), next to the previously established NW-SE trend. Also, a minor fault trend, in between both major fault trends was identified.

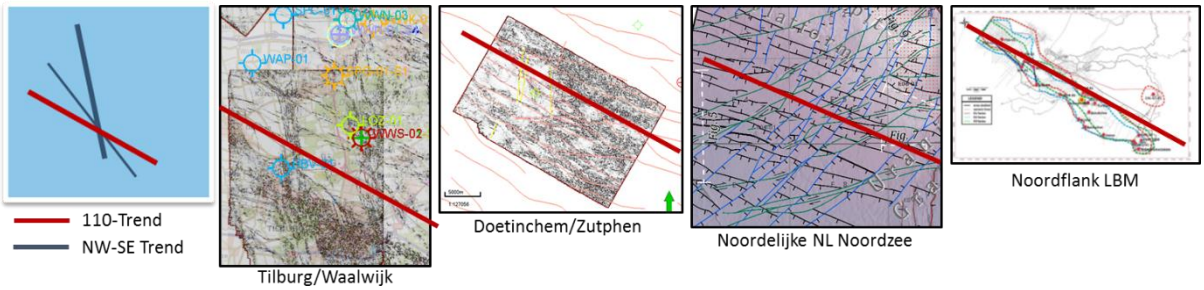

Figure 21. Result of previous studies done on 3D seismics of the Carboniferous at various locations in the Netherlands (ter Borgh, 2017)

The fault trends show that it cannot be assumed that the other faults in the Californië area (visible on a single seismic line) are per definition parallel to the Tegelen fault and Velden fault. Currently, a lack of data prevents the interpretation and reconstruction of these other faults in the Californië area confidently and therefore they are not incorporated in the fault model.

e. Results: Velocity model

The interval velocity of the top three horizons has been calculated using the seismic TWT picks in Appendix C.4. The resulting values are given in Table 4.

For the interval velocity of the Limburg and Zeeland formation, only Dutch onshore and offshore wells that have encountered both formations are taken into account. The figure below shows all wells that drill through the Dinantian. The S05-01, KTG-01, KSL-02, HEU-01S, DB-105, DB-106 and DB-123 are not taken into account, because they do not encounter the Limburg formation. For the Limburg velocity it is important that the offset well shows a thick interval of Limburg formation, because the formation is heterogeneous in terms of lithology. For a trustworthy velocity estimate, it is also important that both formations are located at large depths and that the well has a continuous sonic log. Taking this into account, the Limburg velocity has been derived from the LTG-01 and UHM-02 well and the Zeeland velocity from the LTG-01, UHM-02, O18-01 and S02-02 wells.

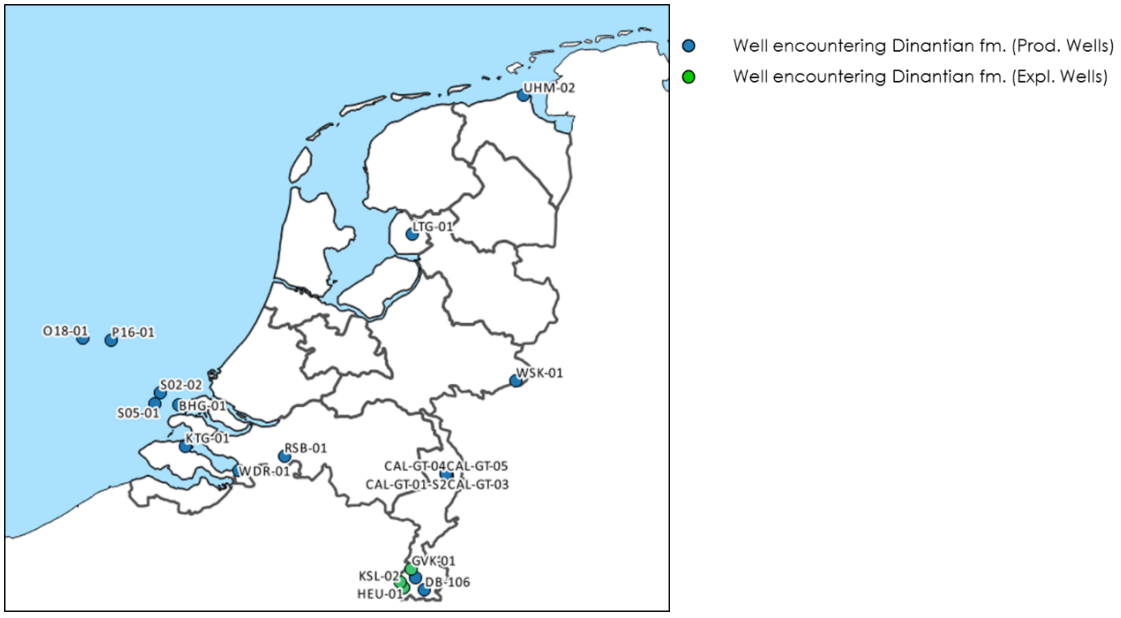

Figure 22. Dutch onshore and offshore wells that drill through the Dinantian carbonates (source: QGIS database EBN B.V.)

Horizon	Interval velocity (Vint) [m/s]	Source
Base NSG	2088	Seismic picks on 09-02 line
Base Chalk	3086	
Base PU	3224	
Base Limburg	4228	Sonic log of offset wells
Base Zeeland	6086	

Table 4. Fixed interval velocities used in the Petrel model

The conversion from time-to-depth with the velocities in Table 4 results in a large inaccuracy for the Base Limburg and Base Zeeland. The resulting horizons are too deep, which implies that the applied interval velocity is too high. To ensure correspondence with the well tops, the Base Limburg and Base Zeeland are corrected with a +200 meter correction in depth. Minor adjustments have to be made on the seismic interpretation for the depth correction, not to obtain problems with the fault modelling (Appendix C.5/6/7).

f. Results: Structural model

In the structural model, the faults, surfaces (in depth) and well tops form the main input. The base NSG and base Chalk are not incorporated in the structural model, because these formations are not part of the reservoir.

Fault model

From the two 2D seismic lines, it is impossible to define an accurate orientation and spatial development of the observed faults. Only two faults are incorporated in the fault model; the Tegelen fault and the Velden fault. The EOWR's specify a fault well top, which is used as a reference during the editing of the Tegelen fault.

Table 5. Fault well top in well CAL-GT-01S, CAL-GT-03 and CAL-GT-04 according EOWR

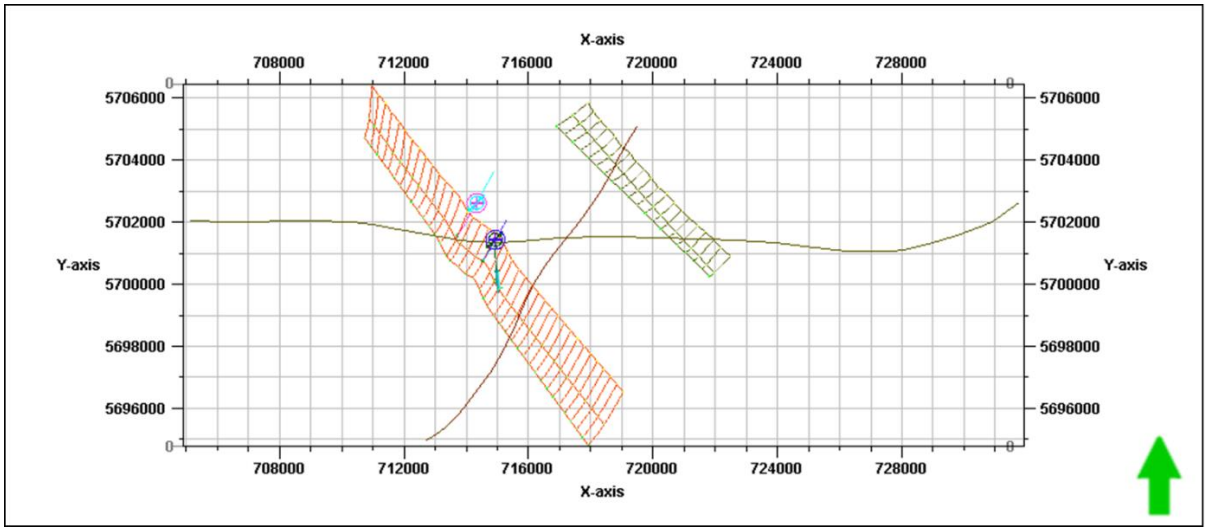

Figure 23. Top view of the Tegelen fault (left) and Velden fault (right)

Horizons

The surfaces of the Base PU, Base Limburg and Base Zeeland are extrapolated based on the two seismic lines, excluding the well tops as a correction factor.

The Base Bosscheveld horizon is made by generating a copy of the depth-converted base Zeeland horizon and displacing this by -243 meter. This value is based on the average thickness of the Bosscheveld formation

determined in well CAL-GT-01S and CAL-GT-03 (well CAL-GT-04 is not taken into account, because the interpretation of the base Bosscheveld well top is uncertain). The base Condroz is placed -900 meter below the base Bosscheveld. This value is based on trial and error, because the horizon is not encountered in the wells and can therefore not cross a well trajectory.

Figure 24 shows the configuration of the surfaces before and after adding the additional grid point sets Appendix C.8. contains all grid point sets for each surface.

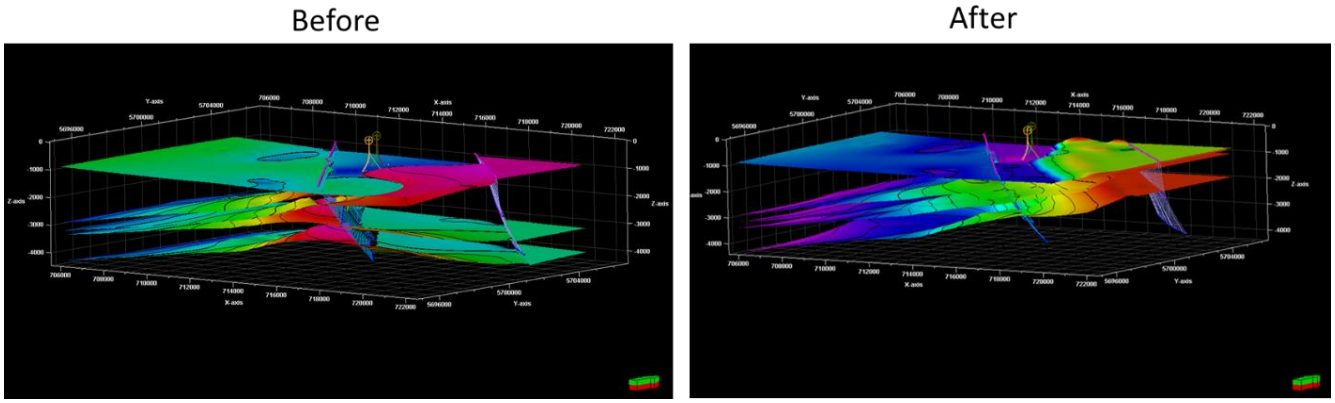

Figure 24. Base Limburg surface before (left) and after (right) of manual editing with grid point sets.

Zones & Layering

The next step in the process is zonation and layering. The Bosscheveld formation is subdivided into the Pont d'Arcole at the top (constant thickness of 40m) and the Bosscheveld formation. The thickness of the Pont D'Arcole is the average thickness encountered in the wells, excluding CAL-GT-03 in which the formation is not clearly distinguishable. The other formations equal a single zone. The layering is proportional for each zone and the amount of layers is defined based on trial and error (the match between upscaled facies log and interpreted facies log defines if the amount of layers is sufficient).

Formation	Zones	Layers
Limburg	Limburg	1
Zeeland	Zeeland	1
Bosscheveld	Pont d'Arcole	1
	Bosscheveld	1
Condroz	Condroz	2

Table 6. Zones and amount of layers for each formation in the fine grid

g. Results: Property modelling

Porosity

The porosity value calculated with the Wyllie equation is based on the sonic log response and shale volume of CAL-GT-01S. The Vshale calculation provides values >1 for the Pont d'Arcole, Limburg and Condroz formation. This value is representative for the Pont d'Arcole and Limburg fm., which are assumed to function as a seal. In contrary, the value is not accurate for the Condroz group, which forms the major part of the reservoir. The inaccuracy lies in the chosen values for the GRmin and GRmax in the formula for Vshale. Therefore the Condroz is assumed to have the same porosity as the Bosscheveld formation. For the calculation of the porosity in the Zeeland and Bosscheveld formation, a dolomite matrix has been assumed. It is important to notice that this method only provides a rough estimate for porosity (very inaccurate).

The results (Table 7) shows that all reservoir formations are estimated to have a very low porosity. Therefore it is assumed that the matrix is tight and probably not able to contribute to flow.

N/G, Sw, Vshale

In the model the following values have been applied for N/G, Sw and Vshale. The values are based on the subdivision into reservoir and non-reservoir rock.

Zone	Porosity	N/G	Sw	Vshale
Limburg	0	0	0	1
Zeeland	0,06	1	1	0
Pont d'Arcole	0	0	0	1
Bosscheveld	0,04	1	1	0
Condroz	0,04	1	1	0

Table 7. Porosity, N/G, Sw and Vshale value for each zone

h. Results: Upscaled structural model

For the dynamic modelling a coarser grid size has been used. Only the horizons have been directly upscaled in the new grid, all other properties have been individually entered and re-calculated in the property calculator.

It is important to notice that the horizontal and vertical grid cell resolution is 100 meter, this means that thicknesses below this value are upscaled to 100 meter.

For the damage zone width, this means that the defined value of 35 meter will be upscaled to 100 meter in the model. Consequently, the model does not implement a geologically representative damage zone.

Zones & Layering

In order to model the different permeability scenario's, the formations have been subdivided into more zones. The table below specifies the zonation and layering.

Formation	Zones	Layers
Limburg	Limburg	1
Zeeland	High permeable layer 1 (120m)	1
	Zone (100m)	1
	High permeable layer 2 (50m)	1
	Zone (rest)	1
Bosscheveld	Pont d'Arcole	1
	Zone (80m)	1
	High permeable layer 3 (50m)	1
	Zone (rest)	1
Condroz	Zone (40m)	1
	High permeable layer 4 (50m)	1
	Zone (80m)	1
	High permeable layer 5 (50m)	1
	Zone (rest)	1

Table 8. Amount of zones and layers for each formation in the coarse grid

The high permeable zones are based on well losses, fault well tops and PLT measurements (Figure 18). The thickness of the high permeable layers is generalized to 50 meter, apart from the top permeable layer in the

Zeeland formation, which is 120 meter thick. This is because multiple wells shows losses throughout the top interval of the Zeeland formation.

- High permeable layer 1 (Zeeland): Includes the top inflow zone (1770-1800 m MD = 1444-1463 m TVD) visible in the PLT of CAL-GT-03 and the karst cave encountered in CAL-GT-01S.
- High permeable layer 2 (Zeeland): Includes the majority of the bottom inflow zone (1950 – 2100 m MD = 1560 – 1655 m TVD) visible in the PLT of CAL-GT-03.
- High permeable layer 3 (Bosscheveld): Based on intersection of Tegelen fault with well CAL-GT-01S
- High permeable layer 4 (Condroz): Based on intersection of Tegelen fault with well CAL-GT-04 and the PLT of CAL-GT-05
- High permeable layer 5 (Condroz): Based on intersection of Tegelen fault with well CAL-GT-03 and the PLT of CAL-GT-05

Permeability

The best-case permeability configuration has been defined using a scenario-based approach. Each scenario consists of a different configuration of the permeability building blocks.

Permeability building blocks

The permeability distribution consists of three main building blocks: Low permeability background fracture network, high permeable layers and the Tegelen fault with a high permeable damage zone.
The figure below provides a conceptual model for the Californië model showing the building blocks.

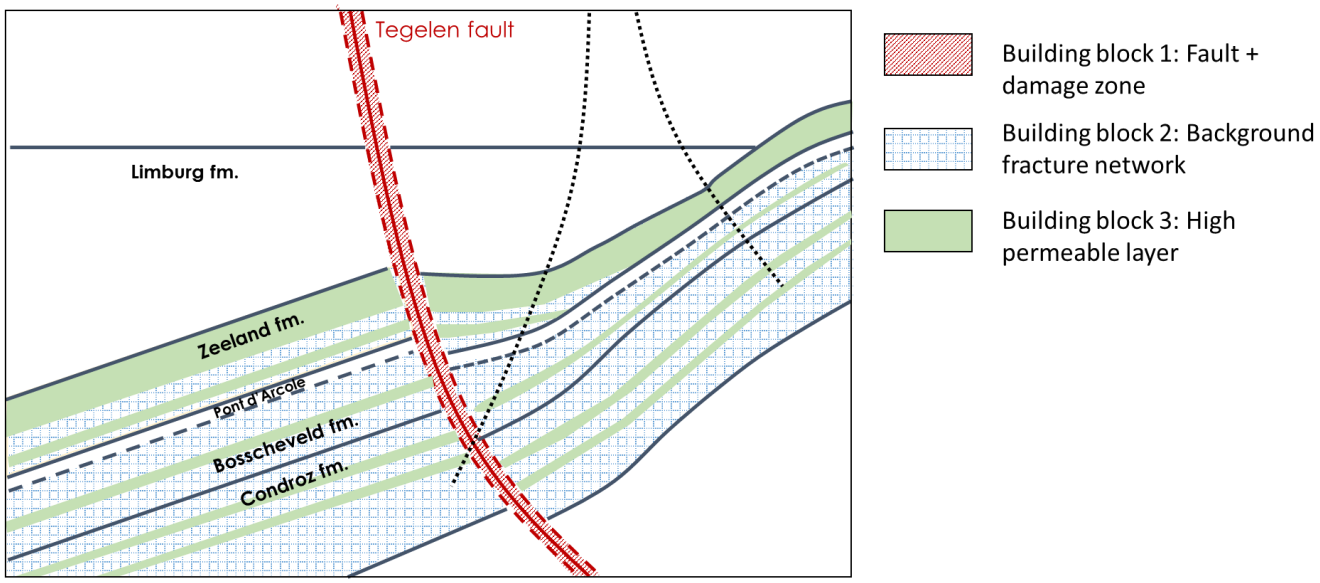

Figure 25. Conceptual model showing the main building blocks for the permeability distribution

Building block 1: Fault + Damage zone

The main fault in the Californië model is the Tegelen fault, enveloped by a damage zone. The permeability distribution in the damage zone is depended on the fracture density. The fracture density is calculated using formula (3) and the corresponding permeability using formula (4) (Mitchell & Faulkner, 2012).

$$F = e^{-\frac{x}{A}} \quad (3)$$

$$K = F^B * C \quad (4)$$

X = Distance to the fault
A = Width of the damage zone (Theoretically = 35 m; In the Petrel model = 100 m)
B = Coefficient determined by trial and error (the permeability at x=100m must equal the permeability value of the background fracture network)

C = Permeability value at the fault core

The permeability component parallel to the Tegelen fault plane (K_J) is equal to K calculated in formula (4). The permeability in this direction forms the main conduit for flow (justified by FMI, which shows that the majority of fractures is NW-SE oriented). Permeability anisotropy is assumed to be present, because the reservoir rock is a fractured medium with a preferred NW-SE oriented fracture direction. Consequently, the permeability in the I and K direction are a fraction of K_J (this fraction can be varied during simulation).

$$K_J = K \quad (5)$$

$$K_I = \frac{K_J}{10} \quad (6)$$

$$K_K = \frac{K_J}{10} \quad (7)$$

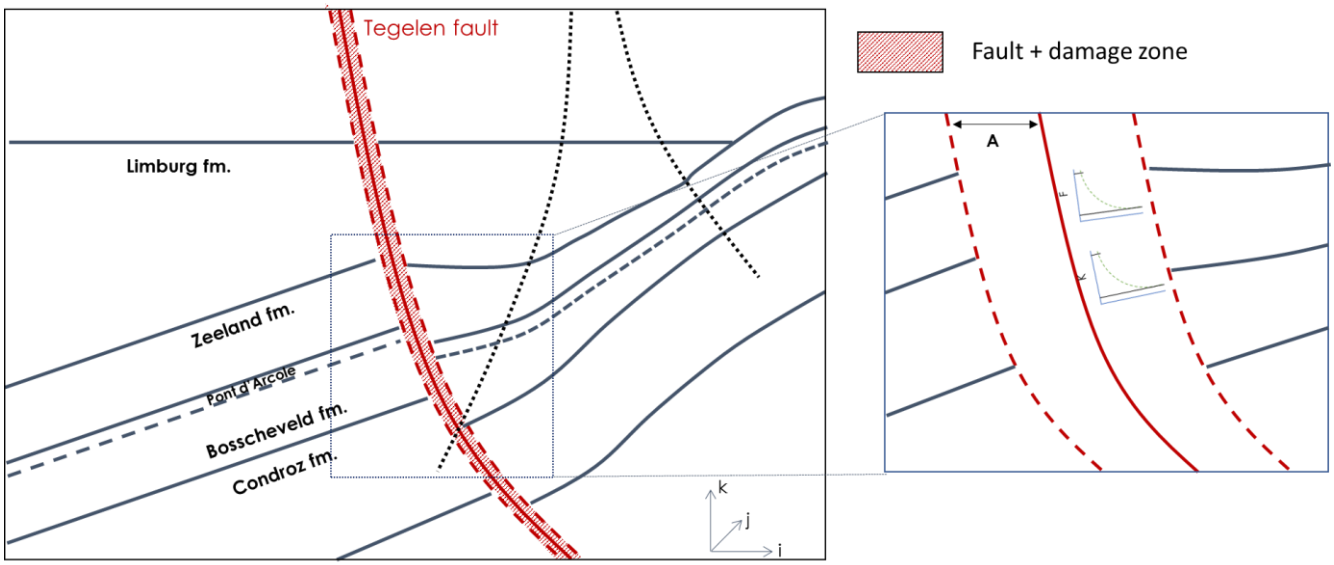

Figure 26. Fracture density and permeability distribution within the damage zone

Building block 2: Background fracture network and high permeable layers

The permeability distribution in the background fracture network is homogeneous and is characterized by a single value in I,J,K direction. The calculated value in the well test data is assumed to be a reference for the geometric average of the permeability in the I,J,K direction applied in the model. The subsurface also incorporates regions with a larger permeability value, due to high density fracture corridors or dissolution features. For this reason, high permeable layers are introduced (depth specified in 'Zones & Layering').

Permeability scenarios

The Base Case scenario for permeability distribution only includes the Tegelen fault. However, from the seismic lines and the fieldwork becomes clear that multiple minor parallel faults are present. The option exists that these parallel faults are part of the damage zone, but they can also function as separate faults with an individual damage zone. Multiple scenarios have been created to test the different permeability distributions. The figure below provides an overview of the scenarios.

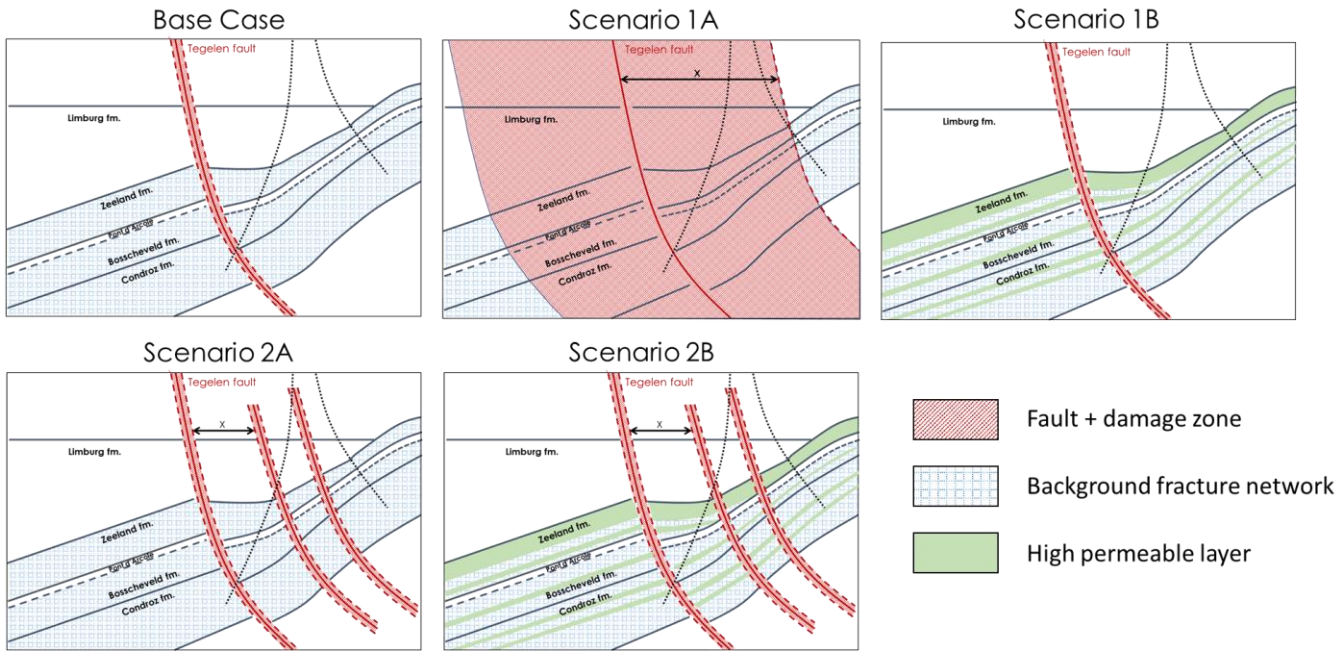

Figure 27. Overview of the scenario's for permeability distribution

Base Case

The Base Case scenario for permeability distribution includes the Tegelen fault with a damage zone of 100 meter (one grid block in the model). The rest of the formation is background fracture network with a single value for permeability.

Scenario 1A

Scenario 1A is a variation on the Base Case. The width of the damage zone has been varied, to simulate the effect of including the parallel faults in the damage zone. The maximum width is attained when all the background fracture networks have been overprinted by damage zone.

Scenario 1B

Scenario 1B is also a variation on the Base Case. In this scenario, the width of the damage zone of the Tegelen fault is fixed to a value of 100 meter (one grid block in the model), but the high permeable layers are included in the background fracture network.

Scenario 2A

Scenario 2A includes the Tegelen fault with a damage zone of 100 meter (one grid block in the model) and a variable amount of minor parallel faults, which are enveloped by a damage zone that has a smaller permeability value than the Tegelen damage zone. The width of the parallel faults is 100 meter (one grid block) and the spacing is also 100 meter. The intermediate parts are filled with background fracture network.

Scenario 2B

Scenario 2B is a combination of all elements. The fault distribution remains the same as scenario 2A, but additional high permeable layers are added in the background fracture network. The same configuration of layers is used as scenario 1B.

Permeability value

The permeability value provided by the well test data, is an average value representative for the entire producing interval in the well, which consists for the largest part of background fracture network. Therefore, this permeability value is used as a reference value for the background fracture network. The permeability value of the high permeable features (layers, parallel faults and damage zone) is based on trial and error.

Contacts, Fluid model & Rock physics functions

A contact set is necessary to define the fluids encountered in the reservoir. To ensure single phase water in the reservoir formations, an oil water contact has been set at 500m depth.

The fluid model contains the average reservoir conditions, which are necessary for Eclipse to predict the phase and behavior of the fluid during dynamic simulation. The reservoir varies in depth and thickness, so the static bottom hole measurements of CAL-GT-03 and CAL-GT-05 have been taken as a reference in this step. The static bottom hole measurements have been averaged to obtain an indication of the average reservoir conditions.

Property	Value
Average reservoir depth	2133,5 m TVD
Average reservoir temperature	81,4 C
Average reservoir pressure	211,2 Bar

Table 9. Average reservoir conditions

The fluid model also contains the salinity of the water, which has been set to 85000 ppm, which is measured in CAL-GT-04 (Laenen & Broothaers, Pump tests on geothermal well CAL-GT-04; Execution, Interpretation and Update of the Calculation for RNES, 2016). The initial conditions can be specified in the fluid model, but a constant reservoir pressure gradient has been applied in the calculator (see Chapter 5d).

Rock physics functions are necessary to define the interaction between two phases in the reservoir and the response of the rock to specific pressure. The rock physics functions include saturation curves and rock compaction. The saturation curves are created, generating a minimum relative permeability for oil . However, the relative permeability curves are excluded in the Eclipse simulation, which means that the water saturation is assumed to be equal to 1 at all times. The rock compaction function is set to the 'compacted sandstone' presets.

5. Well test analysis

a. Input data

Each well has a production and/or injection test. The quality of the well test results of the Californië wells is low (short test periods, large time interval measurements and missing parameters). The figures below provide the timeline of the well test program of each doublet. Well CAL-GT-03 does not have an individual well test, only a PLT.

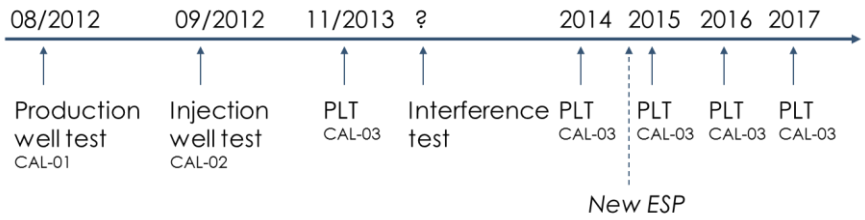

Figure 28. Timeline well testing CWG

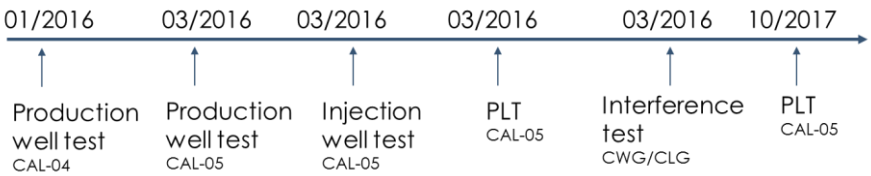

Figure 29. Timeline well testing CLG

b. Methodology

The majority of the well test data is manually analyzed using Microsoft Excel, only the production and injection well test in CAL-GT-05 are analyzed using Kappa Saphir. Pressure Transient Analysis (PTA) in Kappa Saphir can define the skin and permeability for a specific flow model (defined by input parameters for the wellbore, reservoir and boundaries). The fall-off (injection test) and build-up (production test) intervals provide an estimate of the initial pressure (P_i). The resulting value for permeability is applied in the property modelling and forms a reference for the geometrical mean of the permeability in I,J and K direction in the model. The paragraphs below provide the theory for the well test analysis. The theory has been mainly retrieved from (Houzé, Viturat, & Fjaere, 2008-2015) and (Fekete Associates Inc., 2012).

Theory: Inflow performance curve (IPR)

An IPR relationship defines the inflow behavior and productivity of a specific well type. The simplest version of the IPR formula is applicable to undersaturated reservoirs, which means that the reservoir fluid exists as a liquid in the reservoir at initial conditions.

$$Productivity\ index\ (PI) = J = \frac{q}{P_r - P_{wf}} = \frac{flow\ rate}{drawdown} \quad (8)$$

q = fluid inflow rate (m^3/s)
P_r= initial (static) reservoir pressure (Pa)
P_{wf} = flowing bottom hole pressure (Pa)

For a single phase incompressible fluid in a homogeneous reservoir in steady state flow, the IPR curve is linear. This means that the productivity is constant for a range of drawdowns. The PI can also be expressed in terms of reservoir parameters, using Darcy's law.

Darcy's law is a formulation for the momentum balance in a reservoir in the low flow rate regime. Darcy's law provides a relationship between flow rate and pressure difference in a porous medium as a function of multiple reservoir parameters, for the following assumptions:

1. Fluid flow is laminar ($Re < 3000$)
2. Fluid flow is at steady state
3. Fluid is incompressible ($\rho = constant$)
4. Temperature is constant (no changes in ρ or μ of the fluid)
5. Reservoir is homogeneous and isotropic

For radial flow, flow towards the well (producing well) is assumed to be positive. Formula 9 is Darcy's law and formula 10 the integrated version, which provides the flow rate for the pressure drop over a specified circular domain.

$$Darcy's\ law: \frac{dP}{dr} = \frac{q\mu B}{kA} = \frac{q\mu B}{k(2\pi rh)} \quad (9)$$

$$integrated: \frac{P_r - P_{wf}}{\ln(\frac{r_e}{r_w})} = \frac{q\mu B}{2\pi kh} \quad (10)$$

r_e = radius of drainage area (m)
r_w = radius of the well (m)
μ = viscosity (Pa.s)
B = formation volume factor (assumed to be constant, equal to 1)
k = permeability (m^2)
h = height of reservoir (m)

The formula for PI as a function of reservoir properties is then (only valid for Darcy conditions!);

$$J = \frac{q}{P_r - P_{wf}} = \frac{2\pi kh}{\mu B \ln(\frac{r_e}{r_w})} \quad (11)$$

Theory: Diffusivity equation

Dynamic data analysis relies on the linear diffusivity equation, which describes how the pressure in a defined rock volume, reacts in time as a function of the surrounding pressure gradient. The simplest diffusivity equation takes the following assumptions into account:

1. Horizontal flow
2. Homogeneous and isotropic reservoir
3. Single phase and slightly compressible fluid ($c_t = c_{formation} + c_{fluid} = constant$)
4. No gravity effects
5. Darcy's law applies (which means linear flow, $Re < 3000$)
6. Reservoir and fluid properties are independent of pressure

Then, the following formula (for radial flow) can be deducted:

$$Diffusivity\ eq.: \frac{dP}{dt} = 0.0002637 \frac{k}{\varphi \mu c_t} \frac{1}{r} \left[\frac{d}{dr}\left(r \frac{dP}{dr}\right)\right] \quad (12)$$

φ = porosity (fraction)
c_t = total compressibility (Pa^{-1})

For geothermal fields, the linear diffusivity equation is not an accurate estimate, because multiple assumptions are not valid in the reservoir. Due to fracture and karst driven permeability, the flow is not horizontal and the reservoir is not isotropic. This means that assumption 1 and 3 do not apply. Next to this, a geothermal field is not isothermal, which means that the fluid properties depend non-linearly on the thermodynamic conditions in the reservoir (pressure, temperature, composition and saturation). Consequently, assumption 3 and 6 are not valid. However, in the Californië reservoir the temperature is below 100 ˚C, which means that assumption 3 is valid in this specific case (McLean & Zarrouk, Geothermal well test analysis using the pressure derivative: Some common issues and solutions, 2015).
To minimize the uncertainty, the equation must be replaced with a non-linear form, but this requires numerical modelling. This is not within the scope of this Thesis and an analytical solution will be used to extract reservoir parameters.

Boundary conditions

For the analytical approach, it is assumed that at reference time 0, the reservoir is at initial reservoir pressure 'P_i'. In radial coordinates this leads to;

$$Initial\ condition: \forall r \qquad P(r, t = 0) = P_i \quad (13)$$

Next, a pressure disturbance is caused by a well with a well radius r_w. The wellbore component is given by $\left[r \frac{dP}{dr}\right]_{r,t}$ and its definition is dependent on the well condition. The inner boundary condition for a homogeneous finite radius reservoir is defined by applying Darcy's law to the sand face. This leads to the following wellbore component:

$$\left[r \frac{dP}{dr}\right]_{r_w,t} = \frac{q\mu B}{k(2\pi h)} \quad (14)$$

Other inner boundary conditions apply for more complex wellbore conditions (for example fractured or horizontal wells).
The pressure response over time is also influenced by the outer boundary conditions. These outer boundaries can be formed by constant pressure or no flow conditions. The simplest analytical model is an infinite radius reservoir, with the following outer boundary condition:

$$Outer\ boundary: \quad \lim[P(r,t)]_{r\to\infty} = P_i \qquad (15)$$

Wellbore effects

The production of a well is influenced by wellbore effects (modelled as wellbore storage) and the skin effect.

Wellbore storage causes a delay between the measurements at the sandface and surface. When the well is shut-in at the surface, the surface rate is zero, whereas the well will continue to flow bottom-hole until the wellbore is completely filled. The wellbore storage is constant if the reservoir fluid in the wellbore is incompressible.

The skin effect quantifies the difference between the well productivity in reality and in the ideal scenario. A positive skin effect implies that a larger pressure drop is necessary to produce, which means that the effective permeability around the well is lowered. In contrary, a negative skin means an enhancement of the permeability, which results in a smaller pressure drop necessary for production. The skin of a well can change over time.

Theory: Pressure transient analysis (PTA)

PTA is based on the linear diffusivity equation and requires pressure measurements (preferably down hole), flow rate measurements and additional fluid/reservoir information (fluid PVT and dimension of the reservoir).

In contrary to oil and gas fields, which are mostly characterized by short production intervals and a closed structure, geothermal fields are often open structures, where the production intervals are not necessarily bounded by specific formations. The production completion of geothermal wells is therefore often a large open hole section or interval of perforated liner containing multiple production intervals that can respond differently due to density changes of the fluid, which is depended on pressure and temperature. Consequently, the interpretation of the multi-layered reservoir response of the PTA of a geothermal well is not straight forward. In general, the resulting parameters of the PTA represent an average of the production intervals in a well.

In an impermeable well, the reservoir-wellbore pressure differential will be the same at every depth. The pressure transient will represent a scenario similar to a multi-layered reservoir with crossflow. The resulting parameters for skin and permeability will represent an average for the entire interval open for production/injection. In the case of a permeable well, the pressure in the wellbore is controlled by the major production interval. The wellbore pressure is than pinned to the reservoir pressure present at the specific depth of the main production interval. If the water level in the well falls below one of the minor production intervals, downflow can occur. (McLean & Zarrouk, Geothermal well test analysis using the pressure derivative: Some common issues and solutions, 2015).

Flow regime

In time, the flow regime of a well varies. The flow regime is a function of the well condition, shape and size of the reservoir. Each time interval is characterized by a specific flow regime (Figure 30). During the early time response, the flow regime is characterized by wellbore storage effects and skin. In the transient time interval, the flow is in horizontal radial direction and has not yet encountered any boundaries. This flow regime is named Infinite Acting Radial Flow (IARF). The outer boundaries of the reservoir are encountered in the 'Transition' time interval. When the reservoir has constant pressure boundaries (for example gas cap or aquifer support), the flow transforms into steady state flow during the late time interval. If the reservoir has no flow boundaries (for example sealing faults), the late time interval is characterized by pseudo-steady state flow. In this flow regime, the reservoir behaves as a tank (closed volume), which means that the pressure decreases throughout the reservoir at a constant rate. The analysis of this flow regime is only applicable for drawdown/injection data, when the well is flowing (Fekete Associates Inc., 2012).

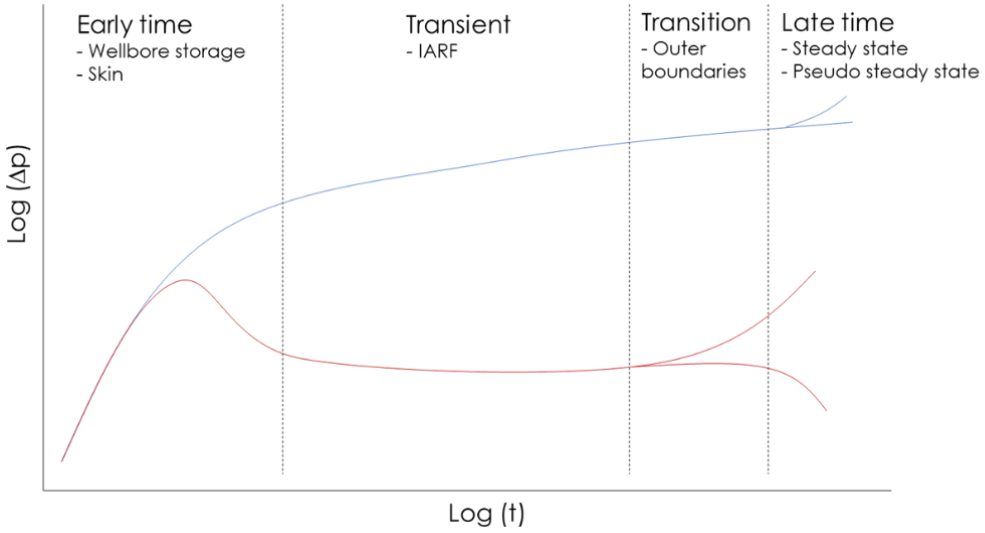

Figure 30. Flow regimes in the pressure response curve on log-log scale [Blue = pressure difference curve / Red = Bourdet derivative]

The PTA is done in the IARF regime, because this interval provides an estimate for average reservoir permeability and skin. When the PTA is performed on a build-up or fall-off well test, the analysis provides an indication of the $p_i$of the reservoir. The signature response of the Bourdet derivative for the different flow regimes and well/reservoir behavior enables to select the correct well bore effects and reservoir parameters to match the analytic solution to the real well test response.

Geothermal well test response

1. *Fractured reservoir*

In a tight reservoir, fracturing of the reservoir rock can occur during injection well tests. This is due to the low permeability, the skin damage near the well and thermal effects. When the fluid pressure exceeds the minimum principal stress of the rock during an injection test, splitting and fracturing of the rock can occur. Conventional well test analysis does not take rock mechanics into account and therefore the result will not accurately identify the reservoir parameters. A fractured well shows a typical pressure response (Figure 31), in which the breakdown pressure is the maximum pressure where the formation initiates a fracture into the reservoir rock. The fracture can propagate during injection and fluid leaks off along the fracture surface into the reservoir rock. This leak-off results in a rapid pressure drop, when the fluid injection is ceased. This point is referred to as the Instantaneous Shut-In Pressure (ISIP) and indicates the start of the fracture closing. From the moment that the fracture is closed, the pressure response transitions into pseudo-linear or radial flow (Bakar & Zarrouk, 2018).

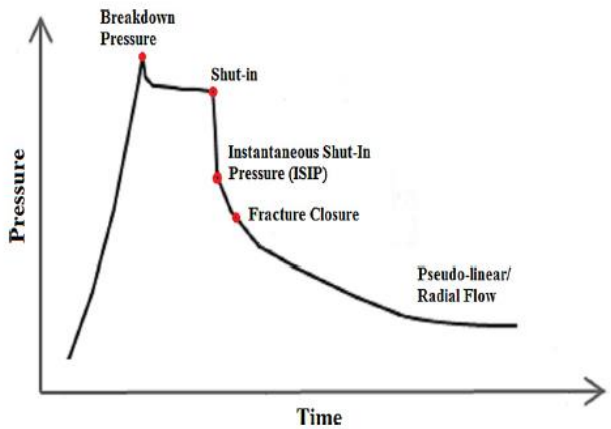

Figure 31. Typical pressure response of a fall off test in a fractured well (Bakar & Zarrouk, 2018)

The Bourdet derivative is characterized by a sharp pronounced dip in the curve at the ISIP. This dip must not be mistaken with the dip due to the downflow principle described in (McLean & Zarrouk, Geothermal well test analysis using the pressure derivative: Some common issues and solutions, 2015), which is not as distinct. Downflow can occur in a multilayered reservoir. When fluid is injected it initially enters the different permeable production zones (also zones above the water table). During fall-off, the fluid in the upper permeable zone can flow back into the wellbore, when the water level falls below this zone. This results in a water column that appears to decrease slower than expected. The downflow effect can also be recognized in the temperature profile and flow profile measured with a PLT during fall-off/build-up. In terms of temperature, the colder injected water exits the wellbore into the permeable zone, which results in a larger temperature gradient along the permeable zone.

2. *Wellbore storage response*

During an injection test, the shut-in can be achieved by closing the master valve at the surface. This results in a smoothly decreasing pressure curve. The smoothness of the curve depends on how quickly the valve is closed. The derivative is characterized by a steep spike at the start that cannot be matched by an analytical model. In a production test this results in the wellbore storage effect, which is characterized by the smooth bump in the beginning of the Bourdet derivative.

If an injection well is controlled by multiple pumps, the different pumps can be shut down one after the other, which results in a pressure drop in multiple stages. The derivative is then characterized by multiple spikes (McLean & Zarrouk, Geothermal well test analysis using the pressure derivative: Some common issues and solutions, 2015).

6. Dynamic model

a. Input data

The production data forms the main input data for the dynamic modelling. The values for pressure and flow rate are partly used as a control mode for the wells in the simulation, but also as a reference for the history match.

Production data: CWG & CLG

The available production data for CAL-GT-01S and CAL-GT-03 (CWG) contains 5-minute measurements for ESP pressure, ESP frequency, injection pressure, flow rate (at surface), production temperature and injection temperature. The data is provided for the period between 08/06/2013 and 08/05/2018, but not all parameters are measured continuously in this period. The average value and standard deviation for each parameter has been determined, dividing the data set into time intervals representative for spring/summer and autumn/winter (Appendix E.2).

The available production data for CAL-GT-04 and CAL-GT-05 (CLG) contains daily measurements of the injection pressure, flow rate (at surface), production temperature and injection temperature. The data is provided for the period between 12/06/2017 and 13/05/2018 and is relatively continuous. From the data appears that the CLG doublet has been frequently inactive, in contrary to the CWG doublet which has been continuously active. The average value and standard deviation of each production parameter is based only on the active days. The calculation of the reference values for the history match is provided in Appendix E.2.

From the production data becomes clear that for injection temperature and production flow rate, the spread (standard deviation) in values is larger in the spring/summer. This is because the energy demand is lower in this season. See Appendix E.3.
The production temperature is the parameter that characterizes the behavior of the reservoir at a specific moment. The plots below show the production temperature development for CWG (CAL-GT-01S) and CLG (CAL-GT-04). The available production data of CLG does not cover the entire production period, because it is known that the wells have been drilled and tested in 2016.
Analyzing the temperature of CWG from the beginning of 2016, it becomes clear that the production temperature decreases with approximately 4 ˚C. This is probably due to the interference with CAL-GT-04, which produces at a constant temperature of approximately 86 ˚C. However, CAL-GT-01S already showed a decreasing trend in the production temperature since 2013, so the entire temperature decrease of 4 ˚C cannot be attributed to the interference with CAL-GT-04.

Figure 32. Production temperature profile of CWG

Figure 33. Production temperature profile of CLG

b. Methodology

The aim of the dynamic modelling is to obtain a match between the simulated pressure and flow rate in the model and the actual pressure and flow rate defined in the production data.
This history match is obtained by varying the permeability configuration within the reservoir using the scenario-based approach, explained in Chapter 4h.

For each different permeability scenario, a ‘Case’ is made in Petrel (RE module). Each case can be tested with the optimum development scenario, which specifies the control mode and corresponding target value for pressure / flow rate in each well.

Petrel works with bottom hole pressures (BHP), which means that the surface pressure provided in the production data must be converted to BHP, in order to function as a reference value in the history match.

Optimum development scenario

The control mode of the wells has been based on the requirements which the well must satisfy. It is assumed that the produced water volume equals the injected water volume, which means that the flow rate of the producer and the injector correspond.

The production wells (CAL-GT-01S and CAL-GT-04) are controlled by rate and the simulated BHP is then matched to the calculated BHP (Table 15). Injection well CAL-GT-03 is controlled by BHP, because SodM has imposed not to inject a few bar above reservoir pressure. The rate has been set as a target.
Injection well CAL-GT-05 is controlled by rate and the BHP has been set as a target.

For the temperature simulation, the injection temperature has been given as an input value and the model simulates the production temperature.

The timeline of the optimum development scenario has been derived from the subdivision into spring/summer and autumn/winter time intervals of the production data. The corresponding average values deducted from the production data have been used as control values. The timeline can be found in Appendix E.4. The second doublet (CLG) has been drilled and tested in 2016. Since the production data covers the period from 12/06/2017, this has been assumed the start of production in this model.

c. BHP calculation

An estimate for BHP can be acquired by calculating the pressure drop over each wellbore. For simplicity a vertical wellbore has been assumed. The first term in formula (16) expresses the gravitational head, the second the frictional losses and the third the acceleration losses. The last is assumed to be negligible, because the wellbore fluid in this reservoir is single phase (water) and does not expand under the wellbore conditions.

$$\frac{dP}{ds} = -\rho g sin(\theta) - \frac{\rho}{2d} f v|v| - \rho v \frac{dv}{ds} \qquad (16)$$

ρ = 1035 (kg/m^3) [fluid density at reservoir condition, T=81 C & salinity = 85000ppm]
g = 9,81 (m/s^2)
μ = 0,0004 (Pa.s) [viscosity]
d = well diameter (m) [well specific]
v = fluid flow rate (m^3/s) [well specific]
ds = pipe length (m) [well specific]

The friction losses are depended on the friction factor 'f', which is explicitly approximated by (Zigrang & Sylvester, 1982). The friction factor depends on the pipe roughness (ε) and the Reynolds number (N_{Re}), which are well specific.

$$Pipe\ roughness: \varepsilon = \frac{e}{d} = \frac{0.0006}{d} \qquad (17)$$

$$Reynolds\ nr: N_{Re} = \frac{\rho v D_{in}}{\mu} \qquad (18)$$

$$Friction\ factor: f = \left\{-2 * \log_{10}\left[\frac{2\varepsilon}{3.7} - \frac{5.02}{N_{Re}}\log_{10}\left(\frac{2\varepsilon}{3.7} + \frac{13}{N_{Re}}\right)\right]\right\}^{-2} \qquad (19)$$

For the production wells, the BHP is the sum of the average pressure at the ESP and the pressure drop below the ESP. For the injection wells, the BHP is the sum of the average injection pressure and the pressure drop below the wellhead (at surface).

Table 10. Well specific parameters and resulting BHP

d. Results

The different permeability scenario's explained in Chapter 4h have been tested in separate case files. To assess the accuracy of each permeability scenario, the following criteria have to be met:

1. The simulated flow rate must match the production data
2. The simulated BHP must match the reference BHP calculated above (Table 15)
3. The simulated production temperature must match the production temperature in the production data.
4. CAL-GT-03 cannot inject below base Zeeland (based on PLT)
5. CAL-GT-05 mainly injects in the high K layers of the Condroz (only a small amount in the bottom zone) (based on PLT)
6. CAL-GT-05 injects a small amount in the high permeable layers of the Zeeland formation (1 and 2) (based on PLT)
7. The value of permeability of each 'building block' must be maintained within a realistic range

The results show that only Scenario 2B provides enough permeability for flow. Therefore this is the best case scenario and the results for the flow and temperature simulation are given below. Multiple sensitivities have been tested to check the accuracy of the results. An overview of the sensitivities and corresponding cases is given in Appendix E.5.

Best case scenario: Scenario 2B

Scenario 2B is a combination of different permeability 'building blocks', specified in Figure 45/46 and Table 16. The modelling specifics of this permeability configuration in Petrel can be found in Appendix E.7.

The injection well test of CAL-GT-05 is the last well test on the timeline of the CLG well test program. The resulting permeability of 2,8 mD provides a reference for the geometric mean of the background fracture network permeability in I,J,K direction. The geometric mean is applied, because the reservoir rock has no apparent preference for vertical or horizontal flow. The permeability in the model (3,2 mD) is slightly higher than the well test result, due to the applied permeability anisotropy ratio, which is based on trial and error. The order of magnitude of the permeability value is the same.

Based on the applied permeability configuration in Scenario 2B, the Kh for every well can be calculated, using the permeability values given in Table 16. The results are given in Table 17 and the individual Kh calculation for each layer in each well is provided in Appendix E.6. The Kh is the sum of the average permeability value of each individual zone times the corresponding height. The calculated Kh of CAL-GT-03 is clearly larger than the other wells, but this is caused by the high permeable regions included in the high permeable layers of the Zeeland formation around this particular well.
The Kh of CAL-GT-05 has been calculated using 2 different heights; the total height of the production zone (based on the completion) and the total height of the producing intervals (based on the PLT). The latter has also been applied in the well test analysis of the production and injection well test of CAL-GT-05. The calculated Kh based on a total height of 510 meter is an order of magnitude lower than the Kh calculated in the injection test of CAL-GT-05 (Figure 40). This means that the average permeability of all zones in Scenario 2B is under estimated.

An additional high permeable region is necessary around well CAL-GT-03, to assure sufficient permeability for the large volume of injected fluid. The radius and value within this region can be varied.
The applied permeability ratio is: $K_i = K_k = \frac{K_j}{10}$, which means that the permeability anisotropy is equal in I and K direction. The fault transmissibility is left at the default value of 1, which means that the faults are fully transmissible.

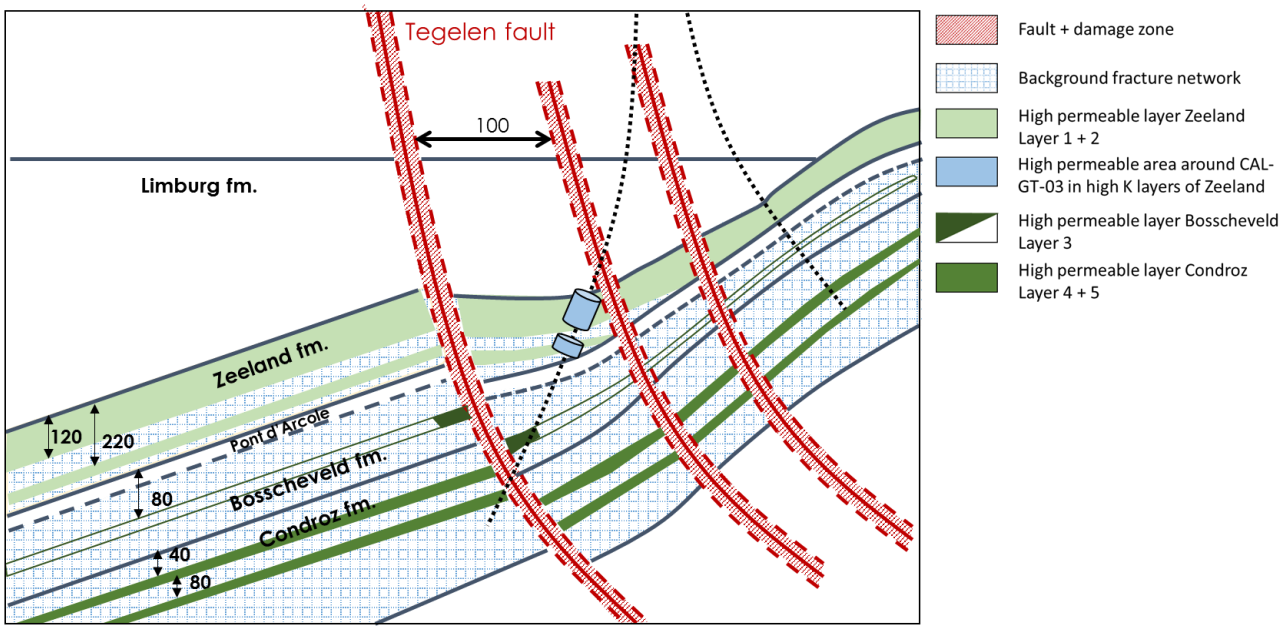

Figure 34. Conceptual configuration of permeability components in Scenario 2B

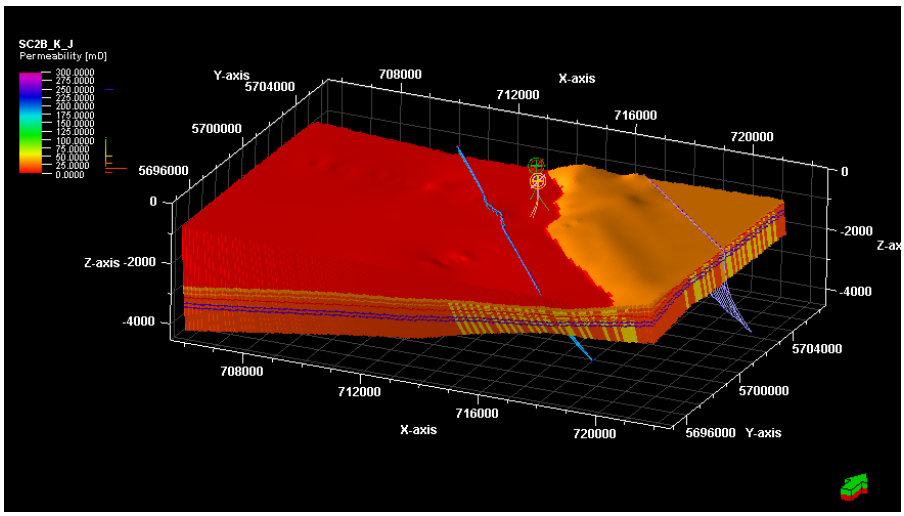

Figure 35. Configuration of permeability components in Scenario 2B in Petrel model

Component	Value Kj [mD]	Geometric mean [mD]	Configuration
High K zone around CAL-GT-03 in high K layers of the Zeeland fm.	2000	431	Within 800 meter radius of CAL-GT-03 in high K layer 1 & 2
High K layer 1 & 2 [Zeeland fm]	30	6,5	Outside 800 meter radius of CAL-GT-03
High K layer 3 [Bosscheveld fm]	250	54	Within 100 meter distance of Tegelen fault, outside this range the layer has regular background fracture network value
High K layer 4 & 5 [Condroz group]	250	54	Two continuous layers
Background fracture networks	15	3,2	Fills up the areas between other permeability components
Tegelen fault core	500	108	Value at fault core, decreases exponentially over 100m from fault core (Tegelen damage zone = 100 m on each side of the fault)
Faults parallel to Tegelen fault	50	11	Constant value for entire damage zone (parallel fault damage zone = 50 m on each side of the 'fault'). The faults have a 100 m spacing (in the Hastenrath quarry parallel faults are visible on this scale).

Table 11. Permeability value of each permeability component in Scenario 2B

Well	Kh (m^3)	Total height (m)
CAL-GT-01S	$6{,}8 * 10^{-13}$	884 (open hole section)
CAL-GT-03	$2{,}5 * 10^{-12}$	768 (perforations)
CAL-GT-04	$7{,}4 * 10^{-13}$	439 (perforations)
CAL-GT-05	$7{,}6 * 10^{-13}$	642 (open hole section)
CAL-GT-05	$7{,}2 * 10^{-13}$	510 (open hole section) > height applied in well test analysis (based on PLT)

Table 12. Calculated Kh for complete production/injection interval in each well

Flow simulation

Figure 47 shows the results for flow and BHP for Scenario 2B. All wells are initially modelled with 0 skin factor, apart from CAL-GT-01S. The modelled BHP for CAL-GT-01S is too high. To lower the BHP, CAL-GT-01S has been simulated with a skin of 7, which means that the production zones are heavily damaged. The positive skin lowers the simulated BHP with a few bar. All results described below include the skin of 7 for CAL-GT-01S.

The results for the simulated BHP show that the match is accurate for CAL-GT-04 and CAL-GT-05. However, the BHP of CAL-GT-01S is too high, which means that the permeability of the production intervals is too large. The production data (Appendix E.2) shows that the ESP pressure of CAL-GT-01S and injection pressure of CAL-GT-03 are approximately constant in time, whereas the production flow rate shows an increase over time. Assuming that the production and injection rate are equal, this means that the productivity and injectivity of the CWG doublet increases. The increasing production flow rate can be explained by the increasing injection flow rate, because the system is incompressible. The interference test of CWG and CLG (Figure 42) shows that CAL-GT-04 responds to the injection of CAL-GT-03 and CAL-GT-05. CAL-GT-01S is located next to CAL-GT-03, meaning that it most probably responds directly if the injection rate is increased. On the other hand, the increased productivity can also be partly due to enhancement of reservoir properties further in the reservoir, related to the continuous flow of water through the reservoir. This phenomenon implies a change of the static model in time, which cannot be captured in the current dynamic model.

Next to this, the simulated BHP of CAL-GT-01S is directly related to the high permeable area modelled around CAL-GT-03. This means that the interference within the CWG doublet is high. To obtain the correct order of magnitude for the permeability of CAL-GT-01S, the permeability value within the area around CAL-GT-03 should be lowered to $K_j = 500\, mD$ (Appendix E.10).

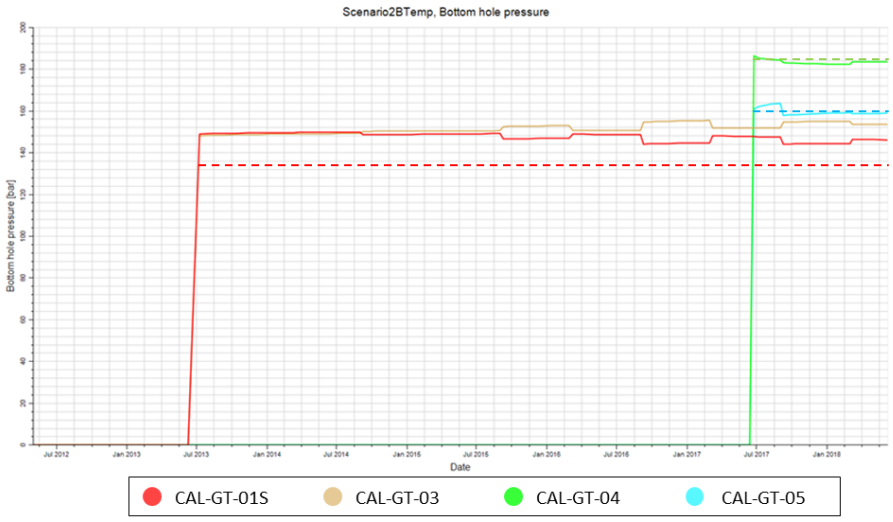

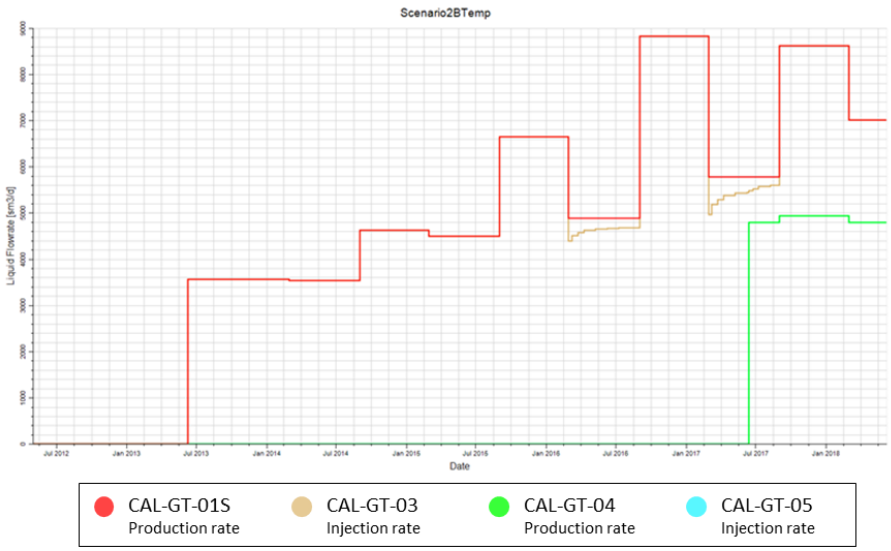

Figure 36. BHP and flowrate plot for Scenario 2B (the dotted lines provide the reference values for an history match)

To estimate the water production intervals in the model, individual tracers have been added in each zone (explanation in appendix E.8). The cumulative water production over time for each tracer is plotted in Figure 49 and the corresponding zone in the model is given in appendix E.9. It becomes clear that CAL-GT-01S produces mainly from the Zeeland formation, whereas CAL-GT-04 mainly produces from the Condroz group.

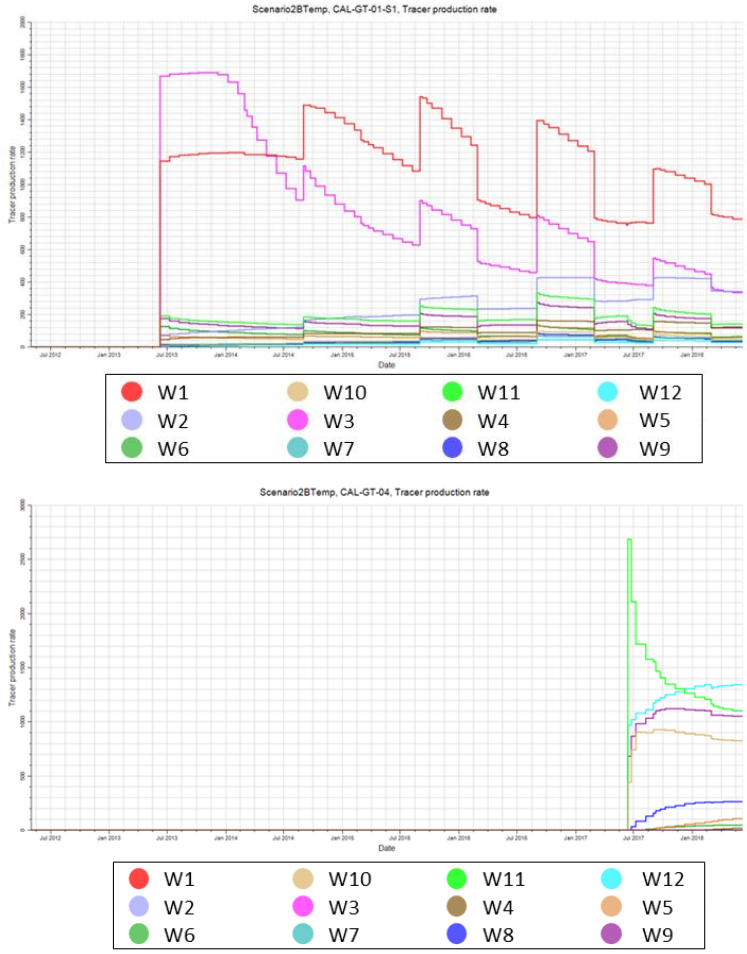

Figure 37. Tracer production indicating the produced water volume per zone for Scenario 2B

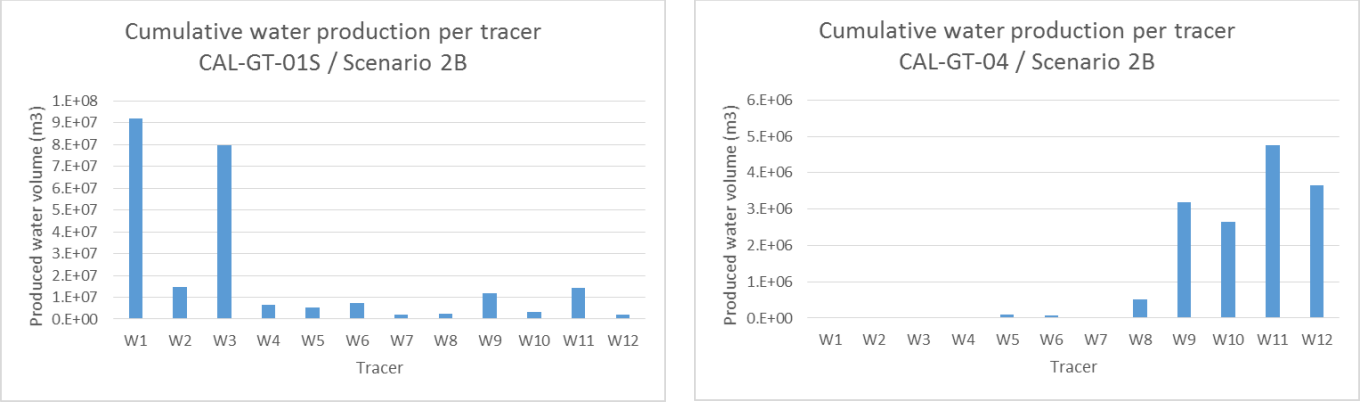

Figure 38. Cumulative production indicating the produced water volume per zone for Scenario 2B

A small interference between well CAL-GT-01S and CAL-GT-04 can be seen in the produced volume from zone 9/10/11/12. As soon as CAL-GT-04 starts producing, the volume of produced water from the Condroz group in well CAL-GT-01S decreases. This interference between both doublets can be further explored, by simulating the Scenario 2B case excluding the CLG doublet (Scenario2BTemp_CWG). The cumulative water production per zone and comparison with Scenario 2B is given in Figure 50 (see Appendix E.11/12 for other plots). It proves that CAL-GT-01S produces more water from deeper layers without the interference of CAL-GT-04, which results in a higher temperature value (1 degrees ˚C higher) at the end of the simulated time frame.

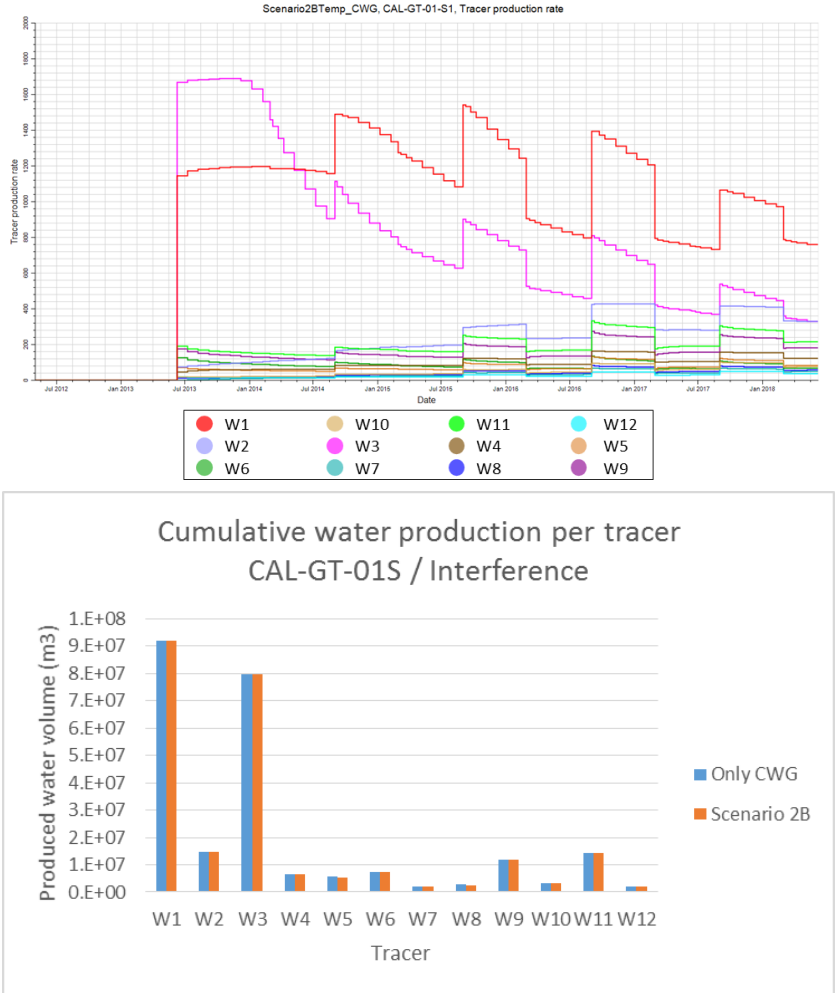

Figure 39. Trace production for Scenario2B_CWG (top) and cumulative tracer production for Scenario 2B and Scenario2B_CWG (excluding the CLG doublet) (bottom)

Analyzing the streamline plots, it becomes clear that the interference between the two doublets is minimal. The injected water by CAL-GT-03 is mainly directed to CAL-GT-01S and only a small fraction that is injected in the Zeeland formation reaches the production interval of CAL-GT-04 in the Condroz group. There is no interaction between CAL-GT-05 and CAL-GT-01S. The producer and injection well within each doublet actively communicate (Appendix E.13).

The tracers cannot be implemented to estimate the main injection zones, because Petrel assumes the tracers to be initially present in the reservoir and moved by the injected water. The injection zones can only be verified by checking the dynamic water flow results. CAL-GT-03 mainly injects in high permeable layer 1 and 2, whereas CAL-GT-05 mainly injects in the high permeable layers of the Condroz group. This corresponds with the observations from the PLT's. The injection zones are directly correlated to the production zones of the corresponding producer well in each doublet.

To check the sensitivity of the simulated BHP, flow and temperature to the implemented permeability configuration and values, a multiplier for K_i/ K_j/ K_k has been applied in the simulation case. The multiplier has a value of 1.5 (Scenario2B_multiplier). The results show that the main difference is the BHP of CAL-GT-04 and CAL-GT-05, which decrease as a function of the increasing permeability. Next to this, the flow rate of CAL-GT-03 now provides a better match (see Appendix E.14/15).

Alternative scenario: Scenario 2B*

An alternative scenario for Scenario 2B has been created, that also matches the BHP and flow rate values. The difference with the initial Scenario 2B is the radius and permeability value of the high permeable zone around CAL-GT-03. In the alternative Scenario 2B* this high permeable zone has a value for K_j of 7000 mD (geometric mean = 1508 mD) within a radius of 370 meter (the other parameters remain unaltered). This extremely high permeable region can be associated with karst features, which can generate open spaces with infinite permeability.

A smaller radius, with a larger permeability value has also been simulated. However, a smaller high permeable volume does not provide enough permeability to ensure the high flow rates of CAL-GT-03 and to capture the increasing injectivity of well CAL-GT-03. Consequently, the target value for flow rate cannot be attained in the high flow rate domain and the well shuts-in when the BHP is slightly decreased (Appendix E.16). A solution would be to increase the permeability of the remaining high permeable Zeeland zones, however this has a negative influence on the inflow zones and BHP of CAL-GT-05.

The simulated BHP of CAL-GT-01S in Scenario 2B* is still too high compared to the reference value. In contrary to the initial scenario, the simulated flow rate of CAL-GT-03 has a better match in Scenario 2B*, because it completely overlies the flow rate of CAL-GT-01S (Appendix E.17). The main difference in Scenario 2B* is the production interval in well CAL-GT-01S: the main production interval shifts towards high permeable layer 1, because CAL-GT-03 injects the largest volume of water into this layer.

Due to this shift in production interval of CAL-GT-01S, the interference effect when CAL-GT-04 starts producing is less distinctive: the decrease in produced water volume in CAL-GT-01S from zone 9/10/11/12 is smaller.

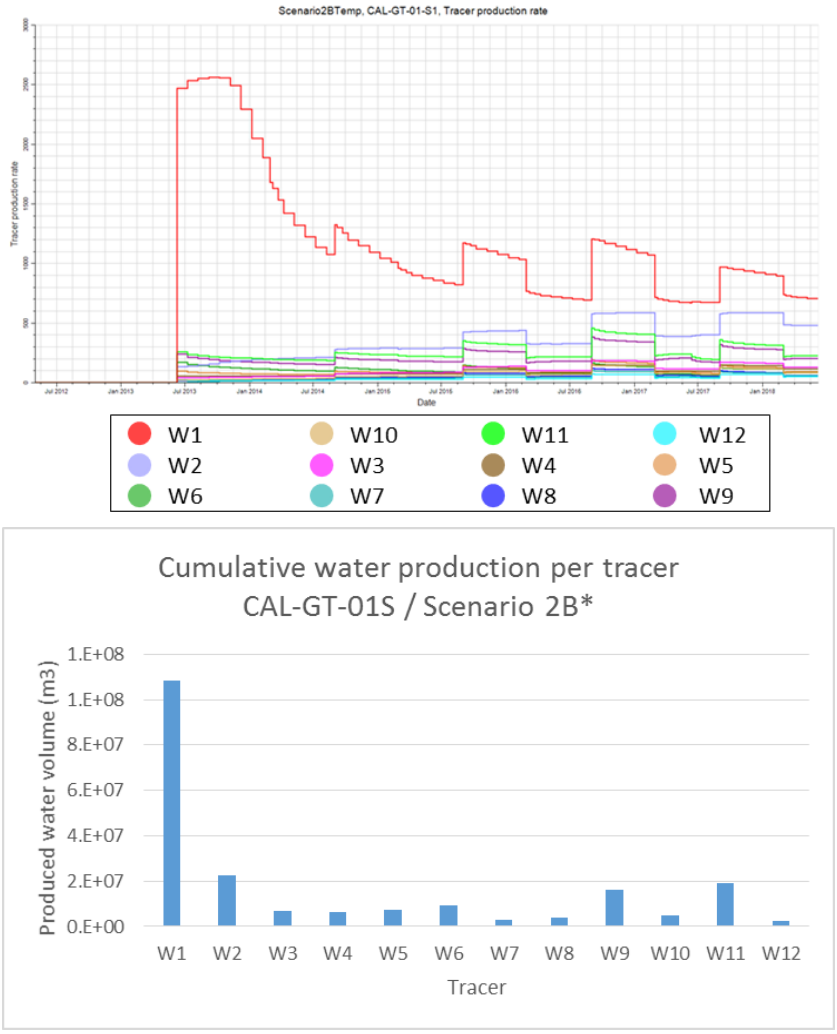

*Figure 40. Tracer production (top) and cumulative (bottom) indicating the produced water volume per zone for CAL-GT-01S in Scenario 2B**

Temperature simulation

The initial Scenario 2B is the most likely scenario and is also simulated for temperature, using the temperature option in Eclipse100 (see Appendix E.7 for explanation of the different keywords). A limitation of Eclipse100 is the fact that it does not take viscosity changes of the fluid as a function of pressure and temperature into account during dynamic simulation, whereas these two parameters influence the simulated BHP and flow rate. However, the reservoir functions in the 75-85 degrees Celsius domain, which limits the uncertainty range to a certain extent, because this low enthalpy regime is a single-phase fluid domain (the static fluid model includes an average reservoir temperature and salinity).

Figure 52 shows the temperature results for scenario 2B. The injection temperature is given as an input in the development scenario. The results show that the production temperature of CAL-GT-01S is too low; the production data shows that the initial production temperature was 76 ˚C when the doublet started producing. The simulated production temperature of CAL-GT-04 is too high; the production data shows that the production temperature was 86 ˚C when the doublet started producing. The model does capture the interference of CAL-GT-01S and CAL-GT-04. When CAL-GT-04 starts producing, the temperature of CAL-GT-01S decreases with approximately 4 ˚C. In the simulation without the CLG doublet, this drop in temperature is limited to 3 ˚C (Figure 53). This means that the temperature drop is also related to the thermal conductivity of the reservoir.

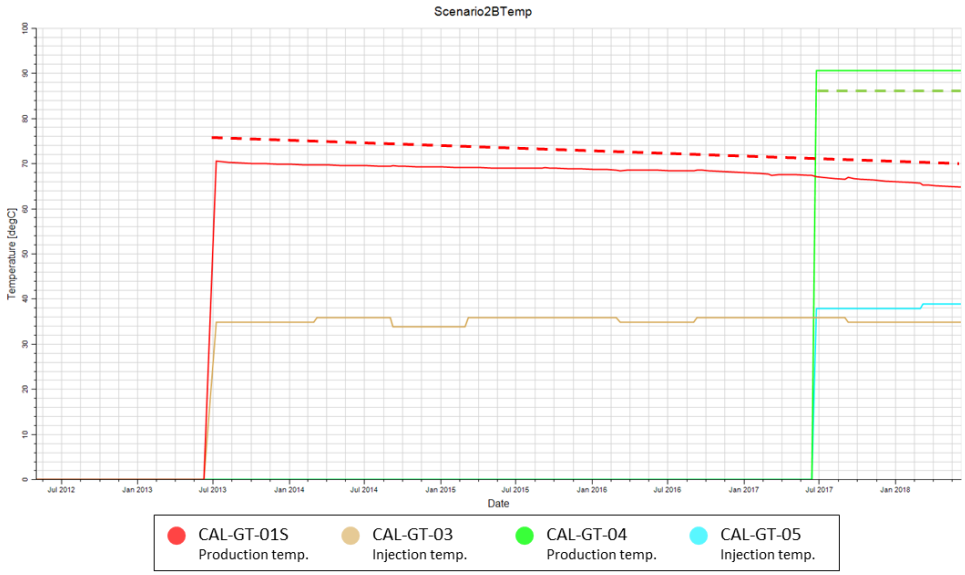

Figure 41. Temperature profile for the injection and production temperature in Scenario 2B (the dotted lines provide the reference values for an history match)

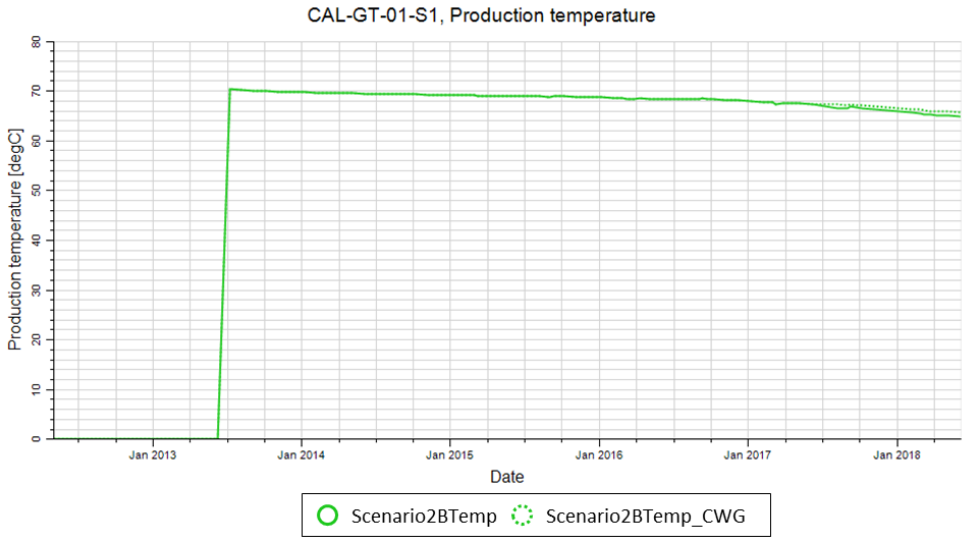

Figure 42. Temperature profile of Scenario2B and Scenario2B_CWG (excluding the CLG doublet)

The temperature distribution in the reservoir is defined by an average temperature gradient of 33 ˚C/km. The temperature results of Scenario 2B do not match the production data, which means that the production wells are probably producing from an incorrect interval. This means that the permeability configuration of Scenario 2B is adequate for the pressure and flow parameters, but not for the temperature.

In order to match the simulated production temperature to the production data, two different sensitivities can be done; the completion of the production wells can be changed to manipulate the production intervals or the temperature gradient can be altered.

Sensitivity 1: changing well completion

The simulated production temperature of CAL-GT-01S is too low, which means that the majority of produced water originates from intervals that are too shallow. To stimulate the production from deeper intervals with a higher temperature, a hydraulic fracture is introduced at 2640m MD (2388m TVD) (depth based on trial and error), which is at the bottom of zone 11. Taking the 33 ˚C/km gradient into account with an average surface temperature of 11 ˚C, the produced water from 2388 TVD has a temperature of approximately 89 ˚C. However,

the water cools down in the wellbore and interferes with water from other production intervals. The temperature of the produced water initially peaks at 79 ˚C and then decreases to 76 ˚C. This is in the range of the production temperature in the production data.

The production temperature of CAL-GT-04 is too high, which means that the majority of produced water originates from intervals that are too deep. To stimulate production from more shallow layers with a lower temperature, a plugback has been installed at 2799m MD (2546m TVD) in the Condroz group (depth based on trial and error). The temperature of the produced water then amounts to 86 ˚C, which is within the range of the production temperature in the production data.

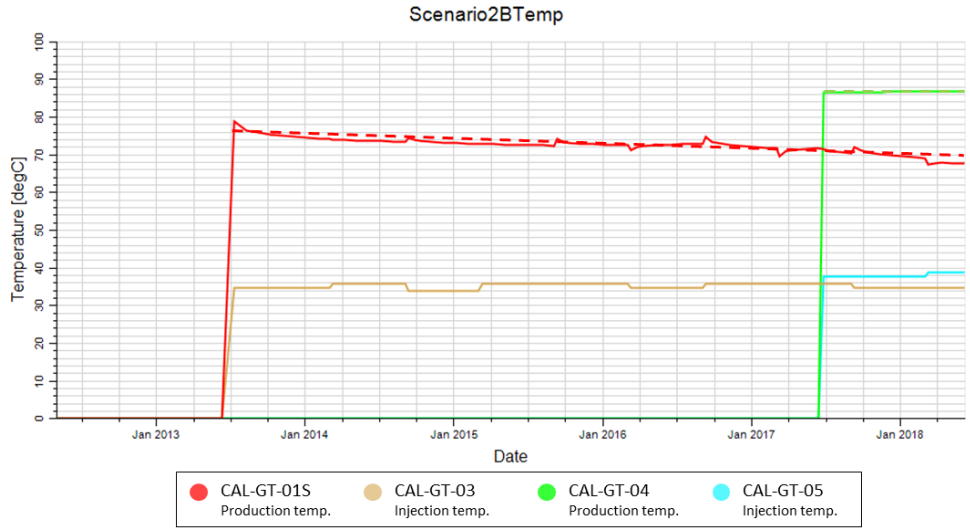

Figure 43. Temperature profile of the wells when the completion has been changed (CAL-GT-01S stimulated with a hydraulic fracture and CAL-GT-04 with a plugback)

The change in completion has an effect on the simulated BHP and flow (Appendix E.19/20). The results show that the simulated BHP of CAL-GT-04 is very low and the match between the flow rate of CAL-GT-03 and CAL-GT-01S is not as accurate.

The cumulative tracer production shows that due to the plugback, CAL-GT-04 can no longer produce a large water volume from zone 11 and 12. In order to meet the acquired flow rate, it must create an enormous drawdown. To decrease this drawdown, the permeability in zone 9, 10, 11 and 12 has to be increased.

The flow rate of CAL-GT-03 is altered due to the hydraulic fracture in CAL-GT-01S, which causes this well to produce a larger volume from zone 12 (Condroz group). Consequently, it produces less from the high permeable layers in the Zeeland formation, in which well CAL-GT-03 mainly injects.

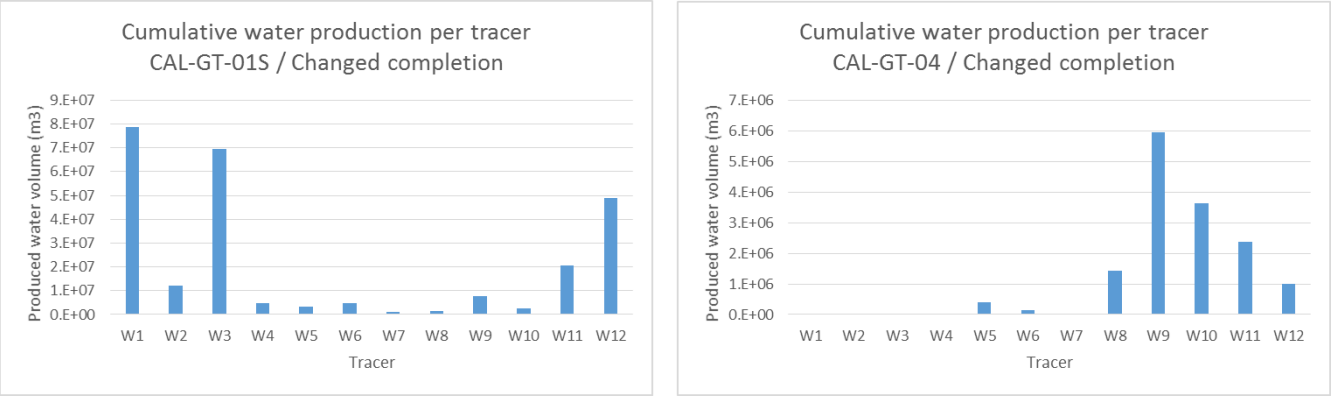

Figure 44. Cumulative water production per tracer indicating the produced water volume for each zone in Scenario 2B (altered completion)

This sensitivity provides an insight in the accuracy of the permeability configuration of scenario 2B. For CAL-GT-01S zone 11 and 12 are stimulated, whereas for CAL-GT-04 these zones are blocked for production. It can be concluded that the permeability distribution of scenario 2B with a temperature gradient of 33 C/km is not correct. Assuming that the temperature gradient is correct, the permeability distribution must be altered by adding local permeability features around each wellbore.

Sensitivity 2: changing temperature gradient

In this sensitivity the production intervals are unaltered, but the temperature gradient is changed to manipulate the simulated production temperature. This change does not affect the BHP and flow rate, because the permeability and production intervals are the same. Appendix E.21/22 provide the plots of the simulation cases.

Initially the simulated production temperature of CAL-GT-01S is too low, which means that it requires a higher temperature gradient. Trial and error shows that it requires a temperature gradient of 36 ˚C/km to produce at approximately 76 ˚C, which matches the production data.

In contrary, the initial simulated production temperature of CAL-GT-04 is too high, which means that it requires a lower temperature gradient. In this case, trial and error results in a temperature gradient of 31 ˚C/km, which leads to a production temperature of approximately 86 ˚C, which corresponds to the production data.

To estimate the accuracy of these thermal gradients, wells in the neighborhood can be used as a reference. The thermal gradient (based on surface temperature of 11 ˚C) of the surrounding wells is given in the plot below. The thermal gradient of AST-GT-02 is very low, but this well only has 2 measurements and the resulting gradient is therefore not accurate. The other 3 wells have a thermal gradient in the range of 30 and 35 ˚C. This means that the calculated thermal gradients for CAL-GT-01S and CAL-GT-04 are not out of range.

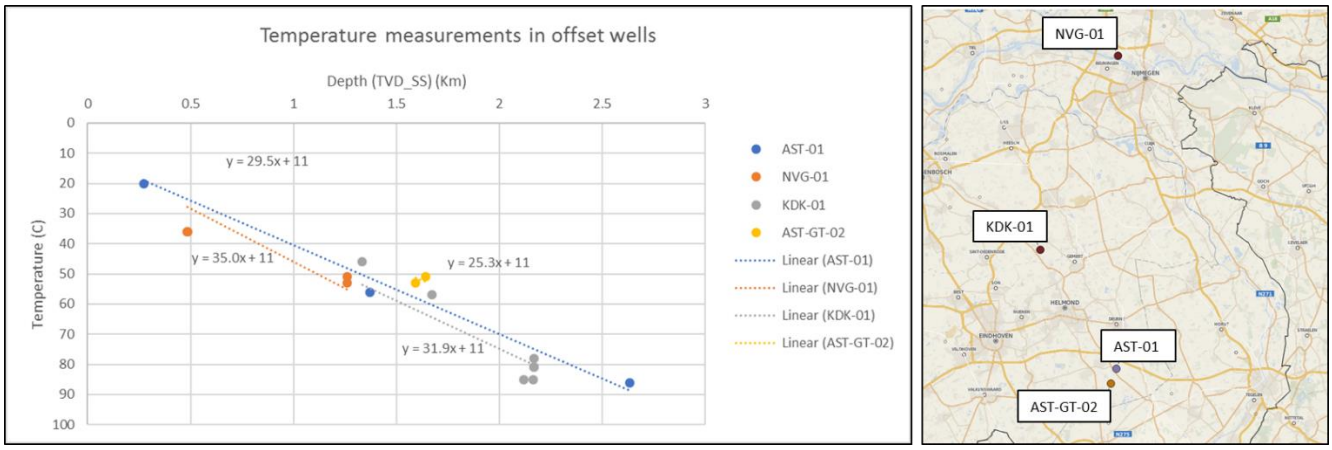

Figure 45. Temperature measurements of the wells in the neighborhood of the Californië wells (Source: Pressure database EBN in Spotfire)

However, the distance between CAL-GT-01S and CAL-GT-04 is approximately 1 km. This means that it would require structural compartmentalization and significant variation in rock properties on a small scale to attain this difference thermal gradient of 5 ˚C/km. Another hypothesis could be that CAL-GT-01S is located close to an area where high temperature water, originating from larger depths, wells up along a high permeable zone. This would require zones with a localized increase of vertical permeability. However, these hypothesis seem less realistic than an incorrect permeability configuration in Scenario 2B.

7. Uncertainty analysis

The fieldwork, static model and dynamic model are characterized by many uncertainties due to the limited amount of available input data. The challenge of this reservoir model is to map out the different uncertainties and create assumptions that minimize the uncertainty range in the result. It is important that these assumptions are well founded and that they fit into the geological framework that defines the subsurface in the Californië area.

All encountered uncertainties are named throughout the chapters. The tables below provide an overview of the uncertainties and corresponding assumptions, impact and recommendations for further work.

Table 13. Overview of the uncertainties encountered in the fieldwork

FIELDWORK

Uncertainty	Available data	Assumption	Impact	Mitigation/Suggested work
General: Available data				
Limited outcrop surface data (inaccurate georeferencing and low quality imaging)	- 7 outcrop surfaces in Hastenrath quarry - 2 outcrop surfaces in Brees quarry		Limited accuracy and applicability of results	Use an UAV for data acquisition (automatic georeferencing and higher resolution) and acquire more outcrop data by visiting multiple quarries in Stolberg area
Analogy between California wells and Hastenrath/Brees quarry				
Difference in burial history	- Regional geological history - FMI CAL-GT-01S - Fine cuttings CAL-GT-01S - Literature: Becker et al. 2014	California and Hastenrath/Brees quarry are analogue	Applicability of resulting damage zone width is not justified	- Core analysis of cores originating from both locations - Additional analysis of fractures (corridors/clustering/ presence of veins etc)
Data acquisition				
Identification of fractures in quarries related to correct geological event	- FMI CAL-GT-01S	The fractures visible on the walls perpendicular to the Sandgewand fault are related to the same geological event causing the fractures in the California wells	Traced fractures can be folding-related (Variscan orogeny), resulting in incorrect fracture density	Accurate determination of orientation of each traced fracture
Fracture digitization				
Distinction between fractures and mining effects		Minimize uncertainty by applying tracing criteria	Misinterpretation of fractures, resulting in incorrect fracture density	Acquire higher resolution data by using a UAV

STATIC MODEL (1)

Uncertainty	Data	Assumption	Impact	Mitigation/Suggested work
General: Available data				
Limited data	- Two 2D seismic lines - All wells: GR, Litho-log - CAL-GT-01S: Caliper, FMI, CMR, Sonic, SP, Resistivity		Limited input data for static model	- Additional 2D/3D seismic lines - Additional wire line logs in all wells - Core data
Well tops				
Well top for Base Zeeland, Base Bosscheveld and Base Condroz	- GR and Litho-log	Apply well top criteria	Incorrect positioning of well tops, resulting in incorrect formation thicknesses and depth	Additional wireline logs
Seismic interpretation				
No well-to-seismic tie: Difficult to pick correct reflector for each well and to identify faults	- Two 2D seismic lines - 4 deviated wells not located on the seismic line	1. Picked reflector is based on seismic character and checked with interval velocity 2. Project wells along 135 degrees angle on seismic line: well top provides reference for top 3 layers	- Incorrect positioning of seismic horizons, resulting in incorrect formation thicknesses and depth (in TWT) - Impossible to trace Base Bosscheveld and Base Condroz - Incorrect positioning of faults	Additional seismic lines through well trajectory
Velocity model				
No checkshot or VSP: inaccurate velocity for all formations	- Two 2D seismic lines - Sonic log CAL-GT-01S - Sonic log offset wells	1. Apply fixed interval velocity for each formation 2. Use pseudo velocity for Base NSG, Base Chalk and Base PU 3. Use interval velocity derived from sonic log of offset wells for Base Limburg and Base Zeeland (this method also has an intrinsic uncertainty, because sonic velocity ≠ seismic velocity)	Incorrect velocity for Base Limburg and Base Zeeland (require depth correction)	Checkshot or VSP

Table 14. Overview of the uncertainties encountered in the static model (1)

Table 15. Overview of the uncertainties encountered in the static model (2)

STATIC MODEL (2)

Uncertainty	Data	Assumption	Impact	Mitigation/Suggested work
Structural model				
Geological history of the California area - Unknown depositional system - Unknown structural geometry (spatial distribution of formations and faults)	- Two 2D seismic lines - Well log data - Fault orientation trend of lower carboniferous in the Netherlands	1. No assumption can be made on depositional system. Two possibilities exist for the Dinantian carbonates: - Carbonate platform - Structural high 2. All structural features follow the NW-SE trend of the Roer Valley Graben 3. Formations dip West and follow the NW-SE trend	- Incorrect spatial geometry of formations, resulting in incorrect volumes - Incorrect placement of faults, which has an impact on the permeability distribution	Additional 2D/3D seismic lines
Unknown production intervals in reservoir formations	- Well losses - PLT CAL-GT-03 - PLT CAL-GT-05	The Zeeland formation, Bosscheveld formation and Condroz group are part of the reservoir	**Unknown/Incorrect reservoir volume**	- Additional PLT's in all wells - Tracer in injection wells
Unknown reservoir properties	- Sonic log: indication of porosity	1. All reservoir formations are homogeneous 2. The value for porosity, N/G, Sw, Vshale is constant for each formation 3. The matrix does not contribute to flow, so the permeability is completely karst and fracture driven	Oversimplification of the reservoir; no distinction between different layers, properties and mechanisms that drive flow. Resulting in a single porosity system.	- Additional wireline logs
Variation in time of static model	- Yearly PLT in CAL-GT-03 - PLT CAL-GT-05 - Well test data	Work with one static model	The mechanisms driving flow (karst and fractures) change in time; this cannot be captured in the model	- Additional PLT's on regular basis

Table 16. Overview of the uncertainties encountered in the well test analysis and dynamic modelling

WELL TEST ANALYSIS

Uncertainty	Data	Assumption	Impact	Mitigation/Suggested work
General: Available data				
Limited and low quality well test data: - Short build-up/fall-off periods - Irregular time interval measurements - Missing parameters	Multiple production and injection tests (see well test overview)	The resulting permeability is an average value for the background fracture network permeability for all production intervals	- Inaccurate resulting values - Unknown initial pressure condition in reservoir	New production/injection well tests for all wells Requirements: - Long build-up/fall-off interval - P/Q measurements at regular (short time) intervals - BHP measurements - PLT
Well test analysis				
Kappa Saphir: Analytical solution of PTA based on linear diffusivity equation (not an accurate estimate for geothermal fields)		No assumption, use Kappa Saphir	Inaccurate resulting values	Use numerical solution with non-linear form of the diffusivity equation

DYNAMIC MODEL

Uncertainty	Data	Assumption	Impact	Mitigation/Suggested work
General: Available data				
Limited production data: (provided by operator) - Flow rate measurements at surface - No BHP measurements	- CWG: Injection/production temperature, production flow rate (not complete), ESP pressure, injection pressure - CLG: injection/production temperature, production flow rate, injection pressure	1. For flow history match: Production rate = injection rate 2. For pressure history match: Calculate BHP with the formula for pressure loss in wellbore	- Unknown injector behavior - Unknown BHP conditions	- Install bottom hole gauge (pressure/temperature measurements) in production wells - Acquire: injection flow rate (CWG/CLG), ESP pressure (CLG)
Simulation				
E100 simulator: density/viscosity changes of fluid not taken into account		No assumption, use E100	The simulated BHP and flow rate in the well not completely correct	Use a more refined temperature simulator suitable for single phase (water) flow in geothermal fields

8. Discussion

This research project focusses on the dynamic simulation of a (partly) Dinantian carbonate geothermal reservoir, which is of large interest for the quickly developing geothermal industry in the Netherlands. The Californië wells are currently the only doublets producing from this formation.

Table 17. Comparison of the VITO, TNO and EBN Californië reservoir model (1)

Table 18. Comparison of the VITO, TNO and EBN Californië reservoir model (2)

In short, the set-up of the VITO and TNO models are relatively similar to the set-up of the model in this research project. The main difference is the permeability configuration and corresponding permeability values applied in the model, which is based on specific assumptions and hypothesis concerning the distribution of the formations and flow mechanisms.

Detailed information on the TNO model can be found in (Geel, 2017) and (Fonseca & Peters, 2017) and detailed information on the VITO model in (Broothaers, 2013), (Laenen & Broothaers, Pump tests on geothermal well CAL-GT-04; Execution, Interpretation and Update of the Calculation for RNES, 2016) and (Laenen & Broothaers, Pump tests on geothermal well CAL-GT-05; Execution, Interpretation and Impact on the performance of the geothermal doublet and update of calculation for RNES, 2016).

a. Software limitations

The modelling of a fractured reservoir involves many challenges. Many (inter)national companies are currently facing these challenges and developing new techniques to model the reservoirs more accurately. This research project uses a combination of Petrel 2016 and Eclipse100 to model the static and dynamic reservoir model of the Californië doublets. Kappa Saphir is used to analyze the well test data.

Kappa Saphir provides a pressure transient analysis of the build-up and fall-of tests, using an analytical solution to match the pressure response and corresponding derivative. However, the analytical solution is based on the linear diffusivity equation. This equation is not valid for fractured geothermal reservoir, which are heterogeneous and do not meet the assumptions of the equation. For a more accurate solution, a numerical approach with a non-linear diffusivity equation must be applied. The paper of McLean & Zarrouk provides a framework for this numerical modelling, but this is not within the scope of this research project (McLean & Zarrouk, Pressure transient analysis of geothermal wells: A framework for numerical modelling, 2017). In case of an analytical solution, it is recommended to subdivide a pressure response of a well test into different parts to capture the time dependent effects (Zarrouk, 2018).

Eclipse100 is a 3-phase, 3-dimensional, black oil petroleum reservoir simulator that models the progression of reservoir and fluid properties as a function of time and space. It is a numerical simulator based on the finite difference method. The simulator provides the option to model single phase water flow.
The temperature option in Eclipse100 is very simplistic, because the simulator was initially set up to simulate the injection of cold water into a reservoir. As a result, the thermodynamic fluid properties are independent of pressure. The viscosity of water is calculated based on temperature, but not on pressure. However, the temperature effect on viscosity is much larger than the pressure effect, so the resulting inaccuracy is not significant.

Eclipse300 is a more advanced simulator, that includes a thermal option that takes into account multiple thermal effects. For high enthalpy systems, this is a more adequate simulator, because it also allows a vapor phase. However, the disadvantage is that it requires input for 3 phase flow, because it was initially designed for specialized processes like steam injection. This means that in case of low enthalpy single phase fluid flow,

multiple dummy functions have to be set up, specifying the additional phases in a very low quantity. For this research project this approach is too complex, because it will not result in a better solution for this system.

b. Validation of results

Validity of Scenario 2B

Scenario 2B forms the final deliverable of this research project, because it is the scenario that provides the most accurate match with the production data (flow/pressure) for the associated assumptions. In terms of temperature, the match is less accurate and the tested sensitivities point out that either the permeability configuration is not completely correct or the temperature gradient is not constant in space.
Scenario 2B takes into account all the available data and the permeability configuration accounts for multiple mechanisms for flow (fractures, karst, damage zone and parallel faults).
However, the reservoir of the Californië wells is extremely heterogeneous and complex. Consequently, it is most probable that other permeability scenarios (containing different permeability configurations or values) will also match the production data (Scenario 2B* is one example).

Apart from the uncertainties named in the uncertainty analysis and the software limitations, these are the most important limitations of scenario 2B:

1. The model does not incorporate the upwelling of (warmer) water from deeper layers and the interaction with groundwater flow.
2. The model assumes all flow mechanisms (karst/fractures/parallel faults) to have a homogeneous distribution in space, characterized by a constant value for permeability. This is considered to be unlikely.
3. The simulations in the dynamic model are based on a single static model; the changing reservoir properties over time are not taken into account.

Recommendations

Currently, the most important unknown parameters are the reservoir geometry and the reservoir properties (porosity/permeability), because these parameters are necessary to create a realistic reservoir simulation. From the uncertainty tables and limitations named above it becomes clear that additional data is highly necessary for this reservoir simulation. High quality 2D or 3D seismics have a high priority, because it not only provides information on the reservoir geometry including faults, but also on the distribution of specific features within the reservoir, such as karst. Additional wireline logs and well tests are also highly necessary to obtain more information on the properties (porosity/permeability) of the different reservoir formations. The well tests in the production wells should be supplemented with a PLT, to define the production intervals. Regular PLT's are required to capture the heterogeneity of the reservoir and the possibly changing production intervals as a result of this.

Apart from additional well data, the analogy between the Californië reservoir and the Hastenrath/Brees quarry can be further established, by analyzing the rock and fracture behavior more thoroughly. Cores from both locations should be acquired and compared in terms of mineralogy. Next, the statistical analysis of the fracture geometries observed in the quarry can be extended. Higher resolution and quality data enables to analyze the clustering of fractures, which gives an insight in the distribution of permeability in the reservoir. Also, the fault corridors created by the minor parallel faults (parallel to Sandgewand fault) should be studied, as they provide an insight on the permeability distribution and anisotropy on a smaller scale.

Next to this, the methodology and approach of simulating fractured carbonate reservoirs can also be optimized by extending the workflow. Currently, the reservoir is modelled as a single porosity system, which is an oversimplification. Additional insights are necessary to model the reservoir as a dual permeability system, in which both matrix and fractures interact. Primarily, a geomechanical model is necessary to simulate the fracture apertures as a function of state of stress in the area. This provides a more accurate insight in the

distribution of fracture permeability characterized by different orientated fracture sets. Next, one must take into account that a fractured rock is affected by thermal effects. Using an analytical solution, the heat transfer in the rock can be approximated, which provides an insight in the thermal breakthrough moment. Therefore, coupled modelling of flow and the mechanical rock properties as a function of pressure and temperature is necessary to estimate the long term development of a geothermal field (Shaik, Rahman, Tran, & Tran, 2011).

9. Conclusion

In this research project, a dynamic reservoir model has been created that approximates the current production and injection behavior of the geothermal Californië wells in Limburg, the Netherlands. The main challenge in this project was the lack of well and seismic data, which required a large number of assumptions for the geometry of the reservoir and the reservoir properties. Due to the assumed tight matrix of all reservoir formations, the main drivers for permeability are the Tegelen fault damage zone, parallel faults, background fracture network and high permeable features (for example karst). The cuttings of well CAL-GT-01S suggest meteoric and hydrothermal dissolution. The different permeability drivers form building blocks, which can be arranged, resulting in a specific permeability configuration. The configuration is unknown and therefore a scenario-based approach has been applied to derive the permeability distribution that is most likely (considering the available data) and that matches the production data.

Due to the complexity of the reservoir and the lack of data, multiple permeability scenarios can approach a history match with the production data. This Thesis presents 2 scenarios (Scenario 2B and Scenario 2B*) of which Scenario 2B is the best case scenario. Scenario 2B matches the production data relatively well, but the history match is not yet optimal. This is due to a few important limitations which prevent the simulated reservoir from capturing the dynamic behavior of the Californië reservoir.
An important limitation is the unknown 3D reservoir geometry and boundaries, which (probably) leads to an incorrect volume of every reservoir formation. On top of this, the specific production intervals in the producing wells are unknown, which means that it is unclear from which depth the produced water originates.
Next to this, the well test analysis proves that the reservoir is heterogeneous and that the reservoir properties change over time. This implies that the static model changes over time, which is a feature that cannot be captured in the current simulation. Also, the heterogeneous distribution of reservoir features (for example karst) is difficult to include in the model. In Scenario 2B all permeability components have a homogeneous distribution. From the results for BHP and flow rate it becomes clear that this concept does not comply to the reality, because the different wells require local features with higher or lower permeability to match the production data.
The temperature simulation result is directly related to the production intervals in each well. Due to an inaccurate permeability configuration, the production zones are not exact, resulting in a simulated temperature profile which does not completely match with the production data. For production well CAL-GT-01S the simulated production temperature is too low, which means that the temperature gradient is higher (36 ˚C/km) or the main production interval is deeper (bottom zone of Condroz group). For production well CAL-GT-04 the simulated production temperature is too high, which means that the temperature gradient is lower (31 ˚C/km) or the main production interval is shallower (top high K layer of the Condroz group).

Taking the limitations into account, the results of this project still provide valuable knowledge on the simulation of a tight geothermal reservoir, in which the permeability is driven by a heterogeneous distribution of fractures, faults and karst features. First of all, this Thesis proves the geothermal potential of the Dinantian carbonates. For the CWG doublet, the fractures and karst features in this formation form the main conduit for flow. The permeability configuration in the best case scenario proves that the Zeeland formation contains features with an average permeability value above 400 mD. More importantly, the reservoir model also proves the geothermal potential of the Bosscheveld and Condroz group. The permeability configuration shows that high permeable layers (>50 mD) are necessary in the Condroz group to obtain a correct history match for the BHP and flow rate (especially in CAL-GT-04 which produces mainly from the Condroz group). Next to this, the permeability configuration in the best case scenario also proves that the background fracture network has a

very low average permeability value (< 5 mD) and that parallel faults with a slightly higher permeability are necessary for flow within the reservoir.
The model also captures the interference between each injection and production well (within a single doublet) and the interference between the CWG and CLG doublet, which expresses itself in the temperature profile.

To optimize and validate the current best case scenario with reality, additional data acquisition is highly necessary. Additional seismic lines (2D or 3D) give information on the extent and development of the different formations and faults, which provides a more definitive answer on the geological history of the area. Next to this, wireline logs and cores are necessary to acquire more information on the depositional system and reservoir properties. For an estimation of the permeability, well tests are necessary. At last, a VSP is required to convert the seismic data from time to depth and regular PLT's are necessary to capture the injection/production intervals and the reservoir heterogeneity in time.

The results of this Thesis prove that the Dinantian and Devonian formations have a high geothermal potential and are therefore very interesting for future development of deep geothermal systems in the Netherlands. The Californië reservoir model is the first reservoir simulation of these heterogeneous and tight reservoirs in the geothermal industry in the Netherlands. The current reservoir model approaches the production data relatively well, however it currently does not have a predictive power. The large set of assumptions and uncertainties shows that the behavior of this reservoir cannot be captured with the limited amount of input data. If additional data is acquired, the Californië model can be optimized and validated, which may result in a larger predictive power for the life-cycle of the reservoir and for future field development. In that case, the reservoir model will also function as an adequate test case for the UDG program, which forms a first step in the energy transition in the Netherlands.

References

Bakar, H., & Zarrouk, S. (2018). Transient pressure analysis of geothermal wells fractured during well testing. *Elsevier; Geothermics*, 26-37.

Becker, S., Nguyen, H., Nollet, S., Fernandez-Steeger, T., Laux, D., & Hilgers, C. (2014). Methods to analyse fracture orientation patterns in a Lower Carboniferous carbonate reservoir analogue in the Voreifel, Germany. *German Journal of Geology*, 319-330.

Benson, R., & Yuhr, L. (2016). *Site characterization in karst and pseudokarst terraines.* Springer.

Berg, S., & Skar, T. (2005). Controls on damage zone asymmetry of a normal fault zone: outcrop analyses of a segment of the Moab fault, SE Utah. *Elsevier*, 1803-1822.

Bertotti, G., de Graaf, S., Bisdom, K., Oskam, B., Vonhof, H., Bezerra, F., . . . Cazarin, C. (2017). Fracturing and fluid-flow during post-rift subsidence in carbonates of the Jandaira Formation, Potiguar Basin, NE Brazil. *Basin Research*, 836-853.

Bezirksregierun Köln. (n.d.). *Tim-Online*. Retrieved from Bezirksregierun Köln: https://www.bezreg-koeln.nrw.de/brk_internet/tim-online/index.html

Bisdom, K., Bertotti, G., & Bezerra, F. (2017). Inter-well scale natural fracture geometry and permeability variations in low-deformation carbonate rocks. *Elsevier: Journal of Structural Geology*, 23-36.

Bisdom, K., Bertotti, G., & Nick, H. (2016). The impact of different aperture distribution models and critical stress criteria on equivalent permeability in fractured rocks. *Journal of Geophysical Research: Solid Earth*.

Bisdom, K., Bertotti, G., & Nick, H. (2017). An integrated workflow for stress and flow modelling using outcrop-derived discrete fracture networks. *Elsevier: Computers & Geosciences*, 21-35.

Boxem, T., Veldkamp, J., & Van Wees, J. (n.d.). *Ultra-diepe geothermie: Overzicht, inzicht & to-do ondergrond.* TNO.

Broothaers, M. (2013). *Het geothermieproject Nieuw Erf/Californie (Horst a/d Maas, NL); Geologische rapportage voor de SDE en SEI garantieregeling.* VITO.

Camelbeeck, T., Vanneste, K., Alexandre, P., Verbeeck, K., Petermans, T., Rosset, P., . . . Van Camp, M. (2007). Relevance of active faulting and seismicity studies to assessments of long term earthquake activity and maximum magnitude in intraplate northwest Europe, between the lower Rhine Embayment and the North Sea. *The geological society of America*.

Choi, J., Edwards, P., Ko, K., & Kim, Y. (2016). Definition and classification of fault damage zones: A review and a new methodological approach. *Elsevier*, 70-87.

DAGO. (2018). *DAGO homepage*. Retrieved from DAGO: https://www.dago.nu/

de Jager, J. (2007). Geological development. In E. Wong, D. Batjes, & J. de Jager, *Geology of the Netherlands* (pp. 5-26).

Duchesne, J., & al., e. (2006). *Geologica Belgica.*

European Commission. (n.d.). *Paris Agreement*. Retrieved from European Commission: https://ec.europa.eu/clima/policies/international/negotiations/paris_en

Faulkner, D., Jackson, C., Lunn, R., Schlische, R., Shipton, Z., Wibberley, C., & Withjack, M. (2010). A review of recent developments concerning the structure, mechanics and fluid flow properties of fault zones. *Journal of Structural Geology*, 1557-1575.

Fekete Associates Inc. (2012). *Fast Welltest: Theory and equations*. Retrieved from Fekete: http://www.fekete.com/SAN/TheoryAndEquations/WellTestTheoryEquations/Theory_and_Equations.htm

Fonseca, R., & Peters, L. (2017). *Reservoir Simulation Analysis Report; Californie Geothermal Project.* TNO.

Geel, K. (2017). *Reservoir-geological model of the geothermal plants in glastuinbouwgebied Californie, Limburg.* TNO.

Geluk, M. (2007). Permian. In T. Wong, D. Batjes, & J. de Jager, *Geology of the Netherlands* (pp. 63-83).

Geluk, M., Duin, E., M.Dusar, Rijkers, R., Berg, M. v., & Rooijen, P. v. (1994). Stratigraphy and tectonics of the Roer Valley Graben. *Geologie en Mijnbouw*, 129-141.

Geluk, M., Dusar, M., & de Vos, W. (2007). Pre-Silesian. In T. Wong, D. Batjes, & J. de Jager, *Geology of the Netherlands* (pp. 27-42).

Guerriero, V., Mazzoli, S., Iannace, A., Vitale, S., Carravetta, A., & Strauss, C. (2013). A permeability model for naturally fractured carbonate reservoirs. *Elsevier*, 115-134.

Hartmann, A., & Baker, A. (2017). Modelling karst vadose zone hydrology and its relevance for paleoclimate reconstruction. *Elsevier, Earth-Science reviews*, 178-192.

Houtgast, R., Van Balen, R., Bouwer, L., Brand, G., & Brijker, J. (2002). Late Quaternary activity of the Feldbiss Fault Zone Roer Valley Rift System, The Netherlands, based on displaced fluvial terrace fragments. *Elsevier Tectonophysics*, 295-315.

Houzé, O., Viturat, D., & Fjaere, O. (2008-2015). *Kappa Saphir: Dynamic Data Analysis.*

Kaufmann, G. (2016). Modelling karst aquifer evolution in fractured, porous rocks. *Elsevier, Journal of Hydrology*, 796-807.

Klimchouk, A. (2016). *Types of hypogene speleogenesis.*

Klimchouk, A., Palmer, A., Waele, J., Auler, A., & Audra, P. (2017). *Hypogene karst regions and caves of the world.*

Kombrink, H. (2008). The Carboniferous of the Netherlands and surrounding areas; a basin analysis.

Kombrink, H., Doornenbal, J., Duin, E., Den Dulk, M., Gessel, S., ten Veen, J., & Witmans, N. (2012). New insights into the geological structure of the Netherlands; Results of a detailed mapping project. *Netherlands Journal of Geosciences*, 419-446.

Laenen, B., & Broothaers, M. (2016). *Pump tests on geothermal well CAL-GT-04; Execution, Interpretation and Update of the Calculation for RNES.* VITO.

Laenen, B., & Broothaers, M. (2016). *Pump tests on geothermal well CAL-GT-05; Execution, Interpretation and Impact on the performance of the geothermal doublet and update of calculation for RNES.* VITO.

Lamarche, J., Lavenu, A., Gauthier, B., Guglielmi, Y., & Jayet, O. (2012). Relationships between fracture patterns, geodynamics and mechanical stratigraphy in Carbonates (South-East Basin, France) . *Elsevier: Tectonophysics*, 231-245.

McLean, K., & Zarrouk, S. (2015). Geothermal well test analysis using the pressure derivative: Some common issues and solutions. *Elsevier; Geothermics*, 108-125.

McLean, K., & Zarrouk, S. (2017). Pressure transient analysis of geothermal wells: A framework for numerical modelling. *Elsevier*, 737-746.

Michie, E., Haines, T., Healy, D., Neilson, J., Timms, N., & Wibberley, C. (2014). Influence of carbonate facies on fault zone architecture. *Elsevier*, 82-99.

Ministry of economic affairs and climate policy. (2017). *Energy Agenda: Towards a low-carbon energy supply*. Retrieved from Government of the Netherlands: https://www.government.nl/documents/reports/2017/03/01/energy-agenda-towards-a-low-carbon-energy-supply

Mitchell, T., & Faulkner, D. (2012). Towards quantifying the matrix permeability of fault damage zones in low porosity rocks. *Earth and planetary science letters*, 24-31.

Platform Geothermie. (2017). *Green Deal Ultra-diepe geothermie (UDG) getekend*. Retrieved from Platform Geothermie: https://geothermie.nl/index.php/nl/actueel/nieuws/194-green-deal-ultra-diepe-geothermie-udg-getekend

Poty, E. (2014). *Report on cuttings from the CAL-GT-01S borehole.*

Reijmer, J., ten Veen, J., Jaarsma, B., & Boots, R. (2017). Seismic stratigraphy of Dinantian carbonates in the southern Netherlands and northern Belgium. *Netherlands Journal of Geoscience*.

Schlumberger. (2012). *FMI Rush Dip Picking Results.*

Shaik, A., Rahman, S., Tran, N., & Tran, T. (2011). Numerical simulation of fluid-rock coupling heat transfer in naturally fractured geothermal system. *Elsevier; Applied Thermal Engineering*, 1600-1606.

SodM. (2017). *Staat van de Sector Geothermie.*

Stewart, R., Huddleston, P., & Kan, T. (1984). Seismic versus sonic velocities; A vertical seismic profiling study. *Geophysics, 49(8)*, 1153-1168.

ter Borgh, M. (2017). *Internal reporting EBN B.V.*

Van Adrichem Boogaert, H., & Kouwe, W. (1993-1997). *Stratigraphic nomenclature of the Netherlands.*

van Adrichem-Boogaert, H., & Kouwe, W. (1993-1997). *Stratigraphic Nomenclature of the Netherlands.*

Van Hulten, F., & Poty, E. (2008). Geological factors controlling Early Carboniferous carbonate platform development in the Netherlands. *Geological Journal*.

Wong, T., Batjes, D., & de Jager, J. (2007). *Geology of the Netherlands.*

Zarrouk, S. (2018). *Geothermal reservoir engineering (short course).* IGA.

Ziegler, P. (1991). North Sea rift System. *Tectonophysics*, 55-75.

Zigrang, D., & Sylvester, N. (1982). Explicit approximations to the solution of Colebrook's friction factor equation. *AlChe Journal* , 514-515.

Appendix

Appendix A: General

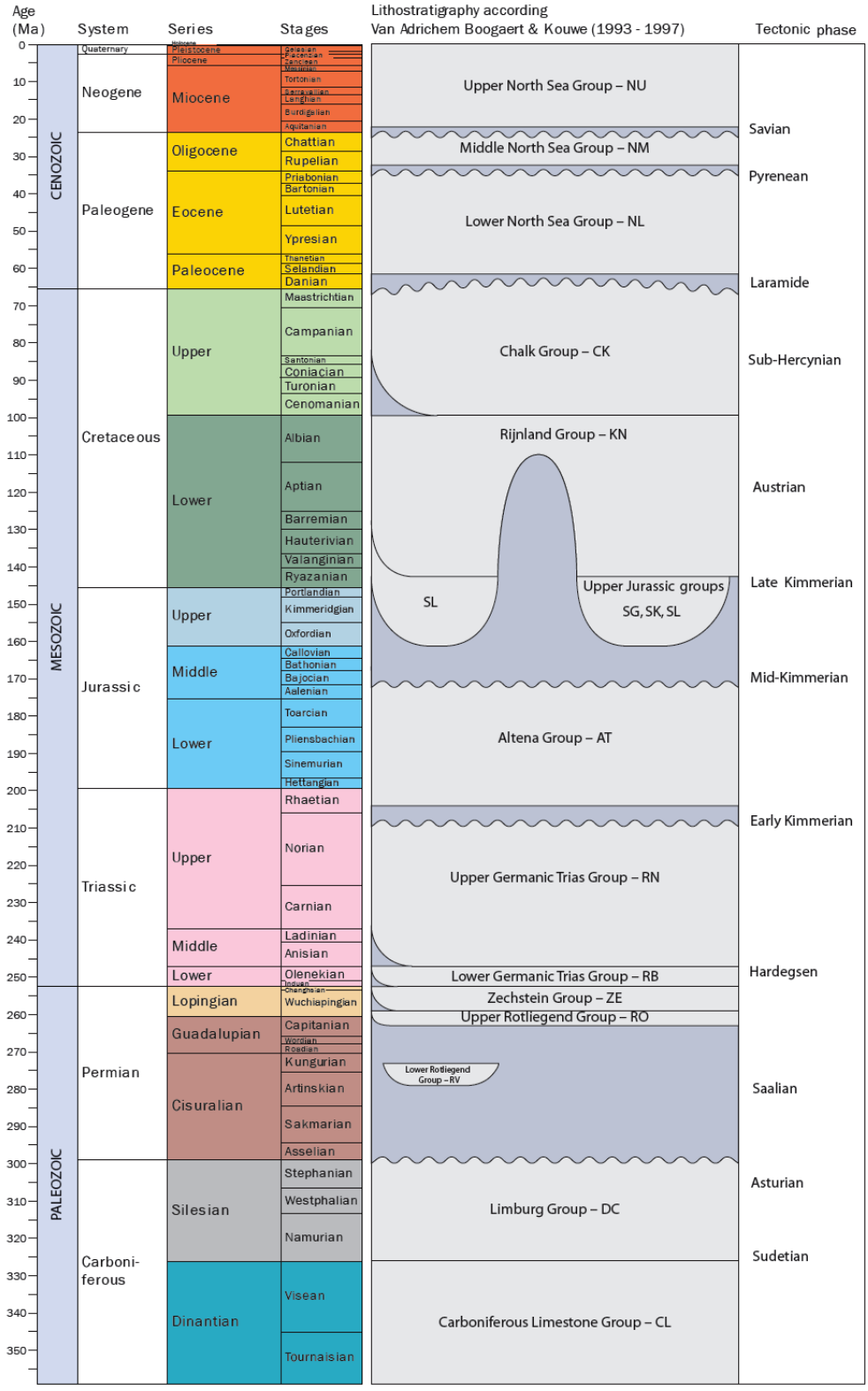

Appendix A. 1. Geological timescale specifying the different eras, periods, subperiods (or epochs), ages, lithostratigraphic groups, tectonic phases and orogeny's (Van Adrichem Boogaert & Kouwe, 1993-1997)

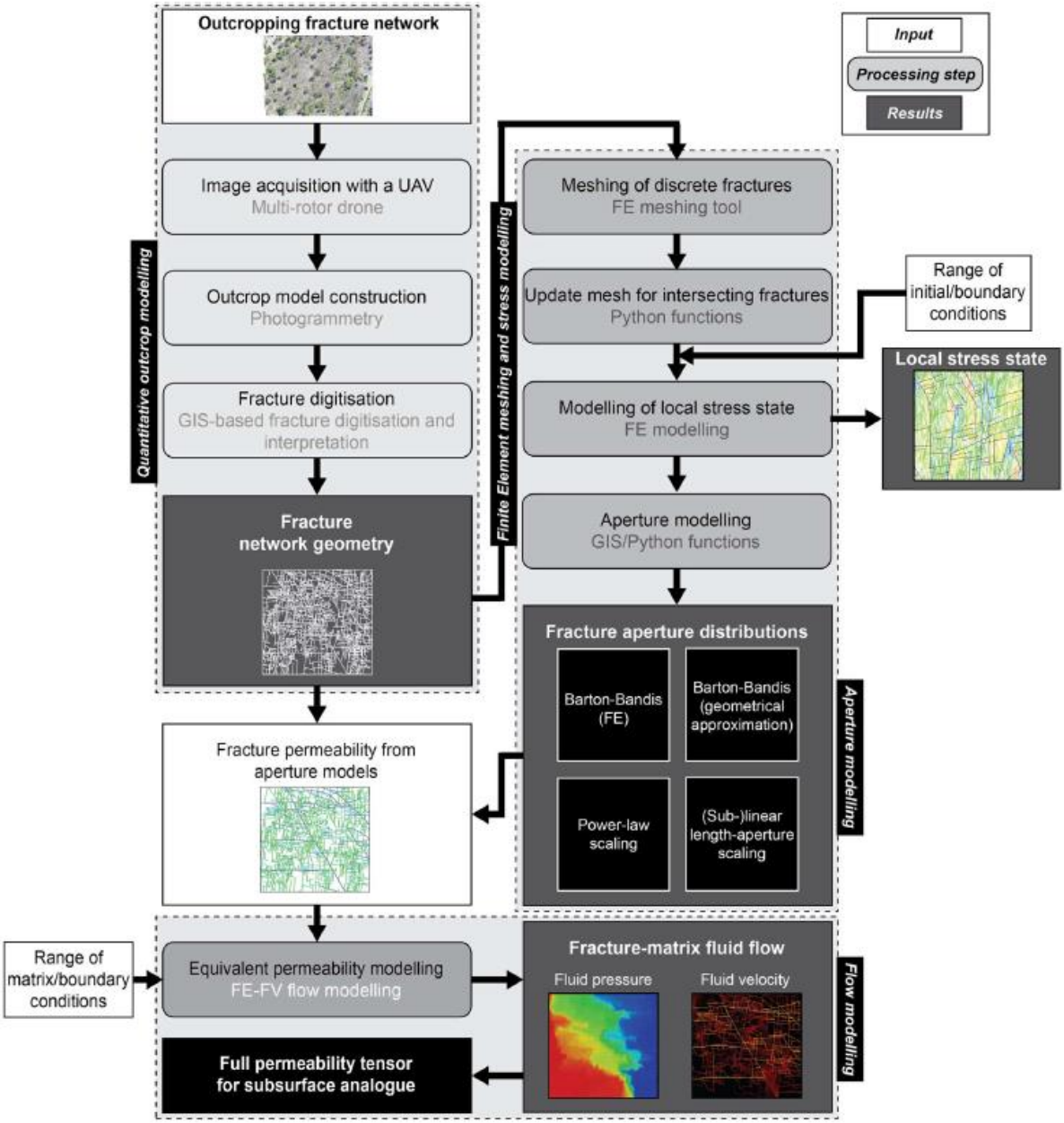

Appendix A. 2. Workflow for obtaining flow based principal permeability from outcropping networks that are analogue to a specific subsurface reservoir stress and pressure conditions, by taking into account the impact of stress on aperture and flow (Bisdom, Bertotti, & Nick, An integrated workflow for stress and flow modelling using outcrop-derived discrete fracture networks, 2017)

Appendix B: Fieldwork

Appendix B. 1. FMI results interpreted by Schlumberger

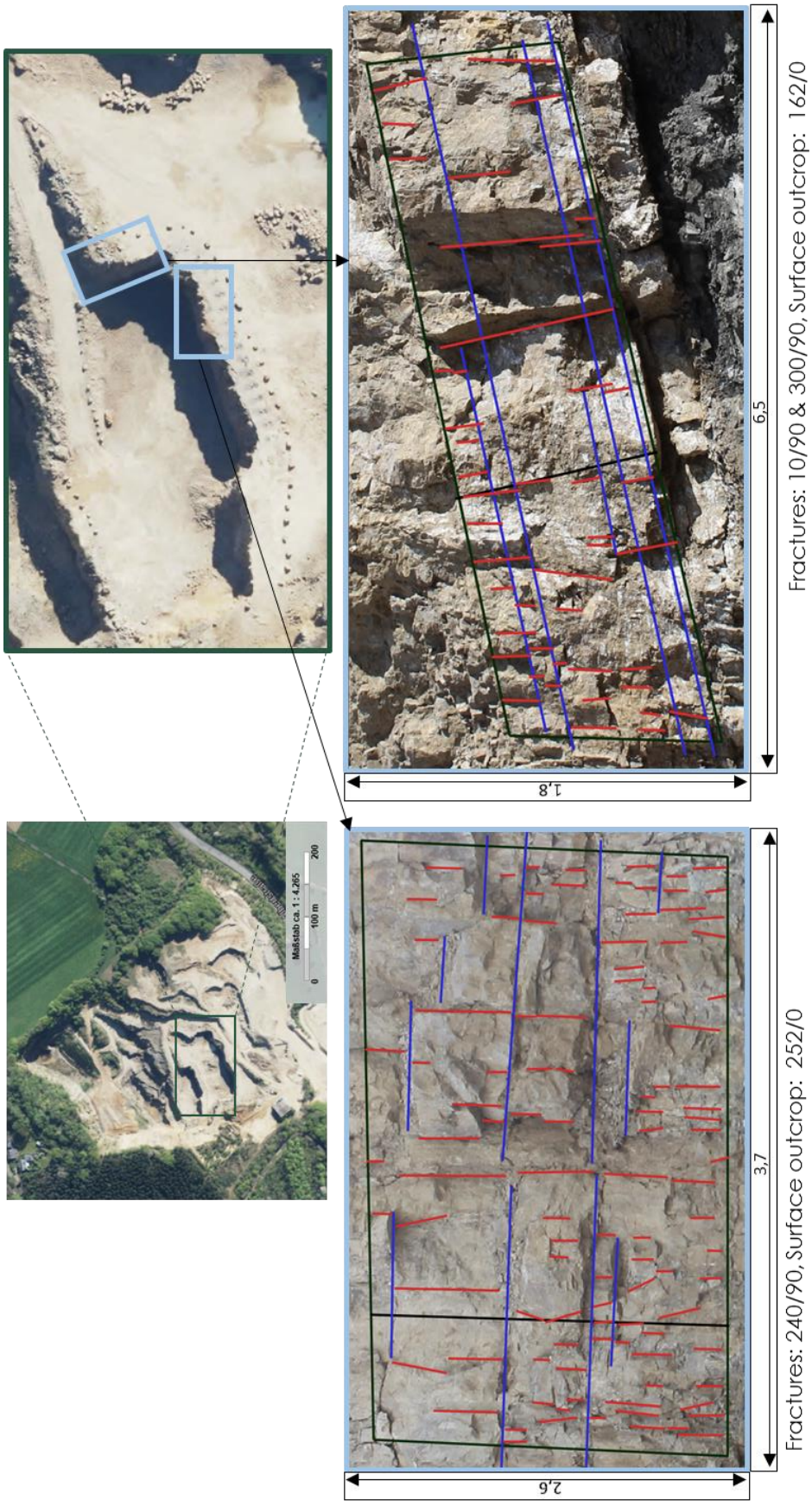

Appendix B. 2. Outcrop surface HAS0 & HAS1. Length indicates width of analyzed outcrop (horizontal) and length of the trackline (vertical)

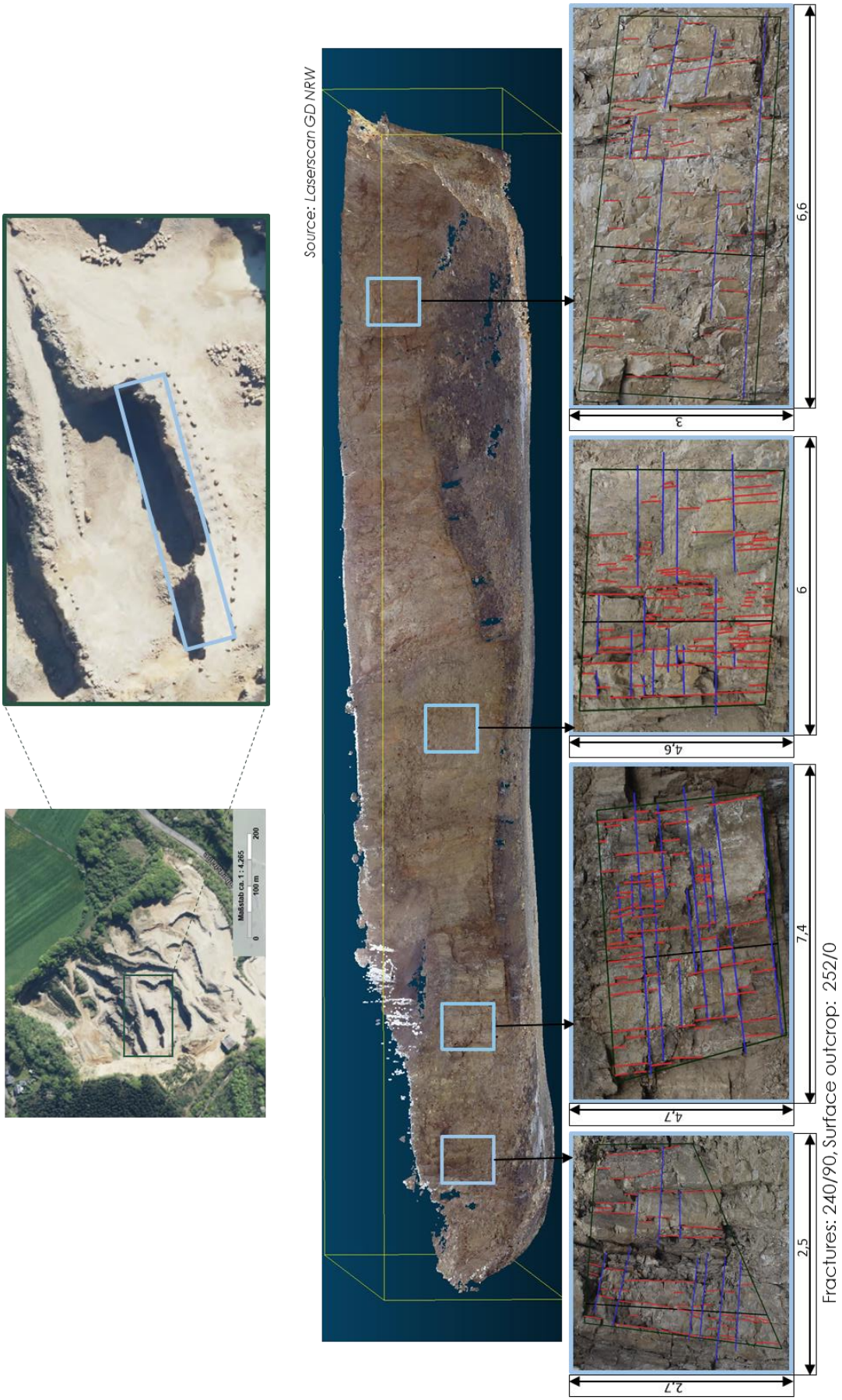

Appendix B. 3. Outcrop surface HAS 6/3/4/5. Length indicates width of analyzed outcrop (horizontal) and length of the trackline (vertical)

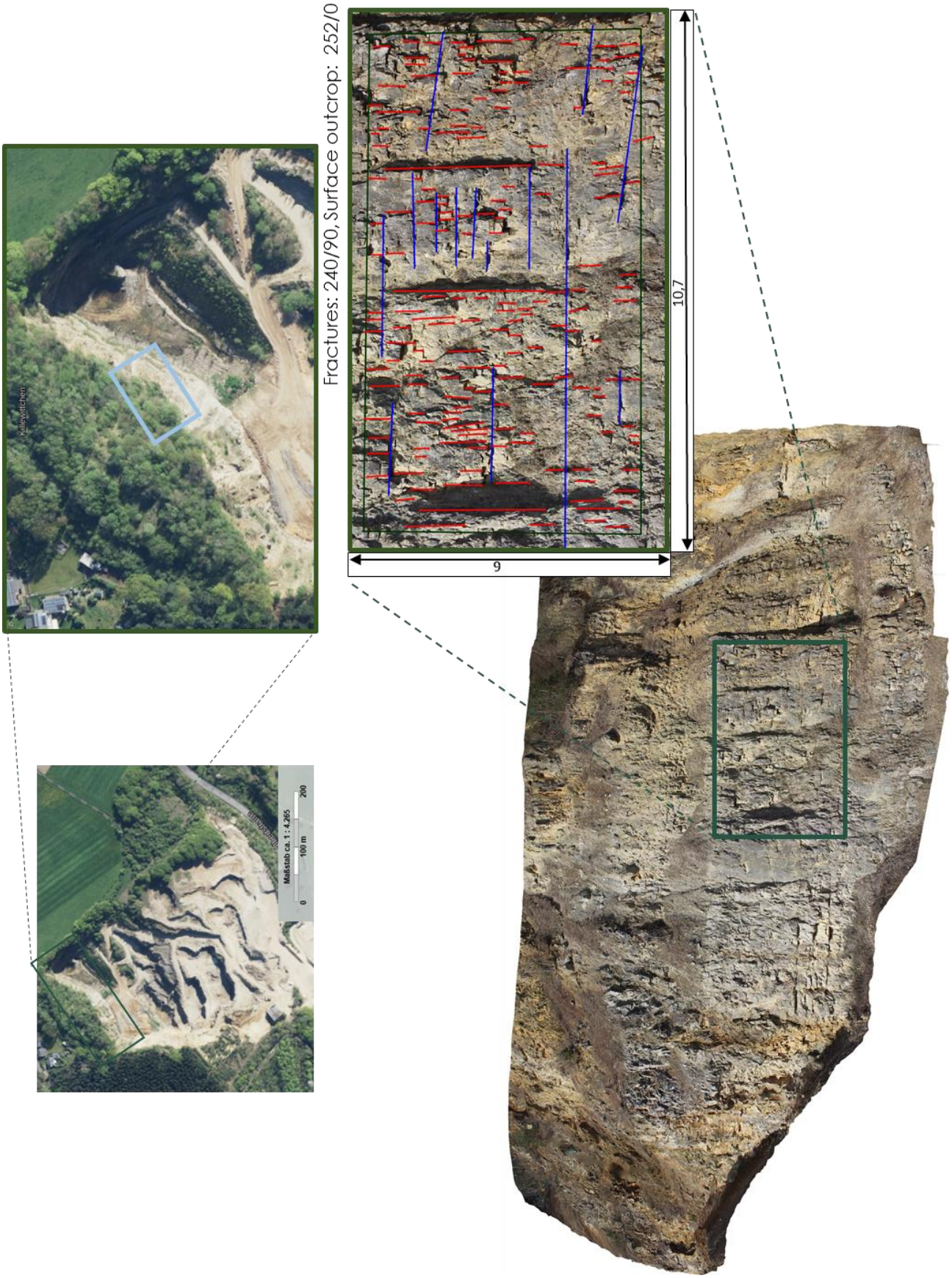

Appendix B. 4. Outcrop surface HAS 2. Length indicates width of analyzed outcrop (horizontal) and length of the trackline (vertical)

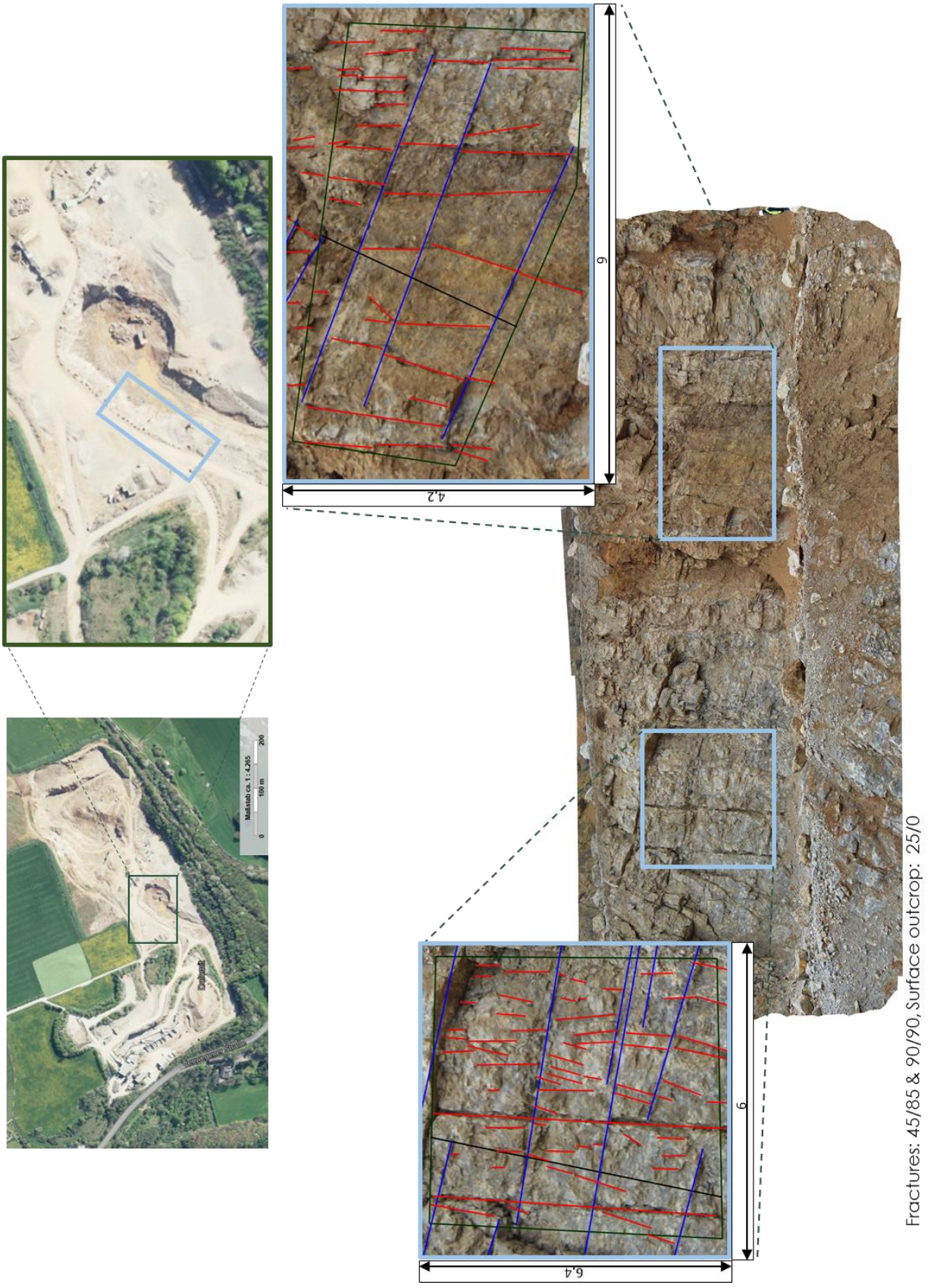

Appendix B. 5. Outcrop surface BRE0 and BRE1. Length indicates width of analyzed outcrop (horizontal) and length of the trackline (vertical)

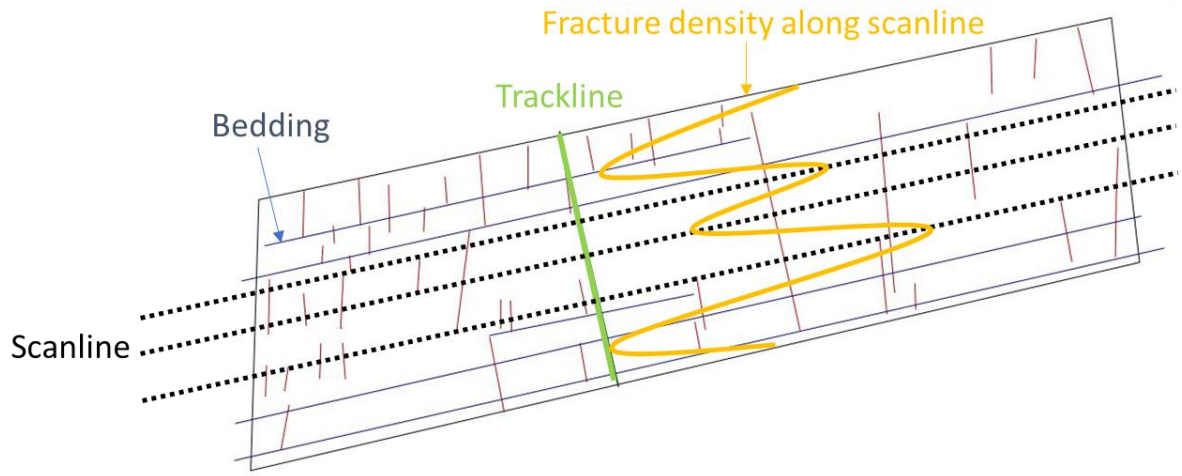

Appendix B. 6. Schematic overview of scanline analysis

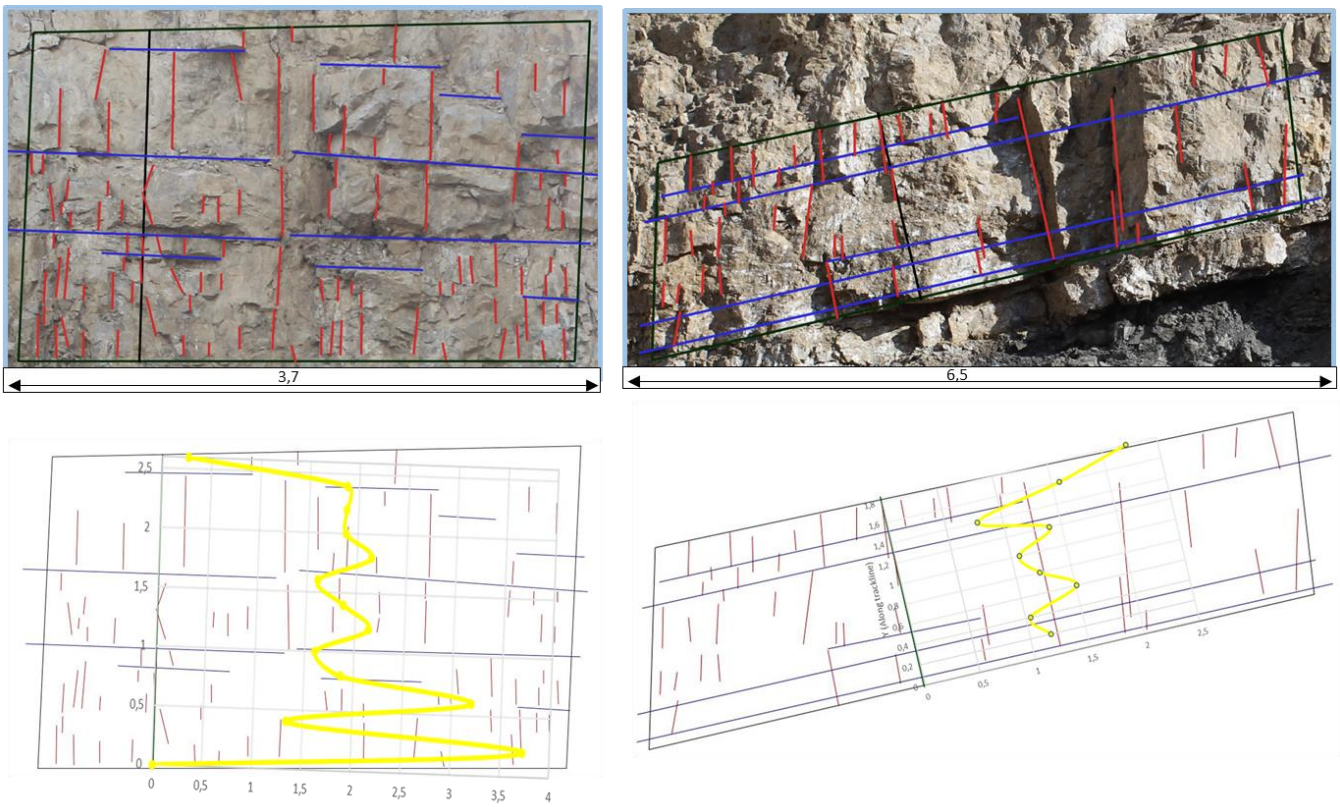

Appendix B. 7. Scanline analysis of HAS0 and HAS1

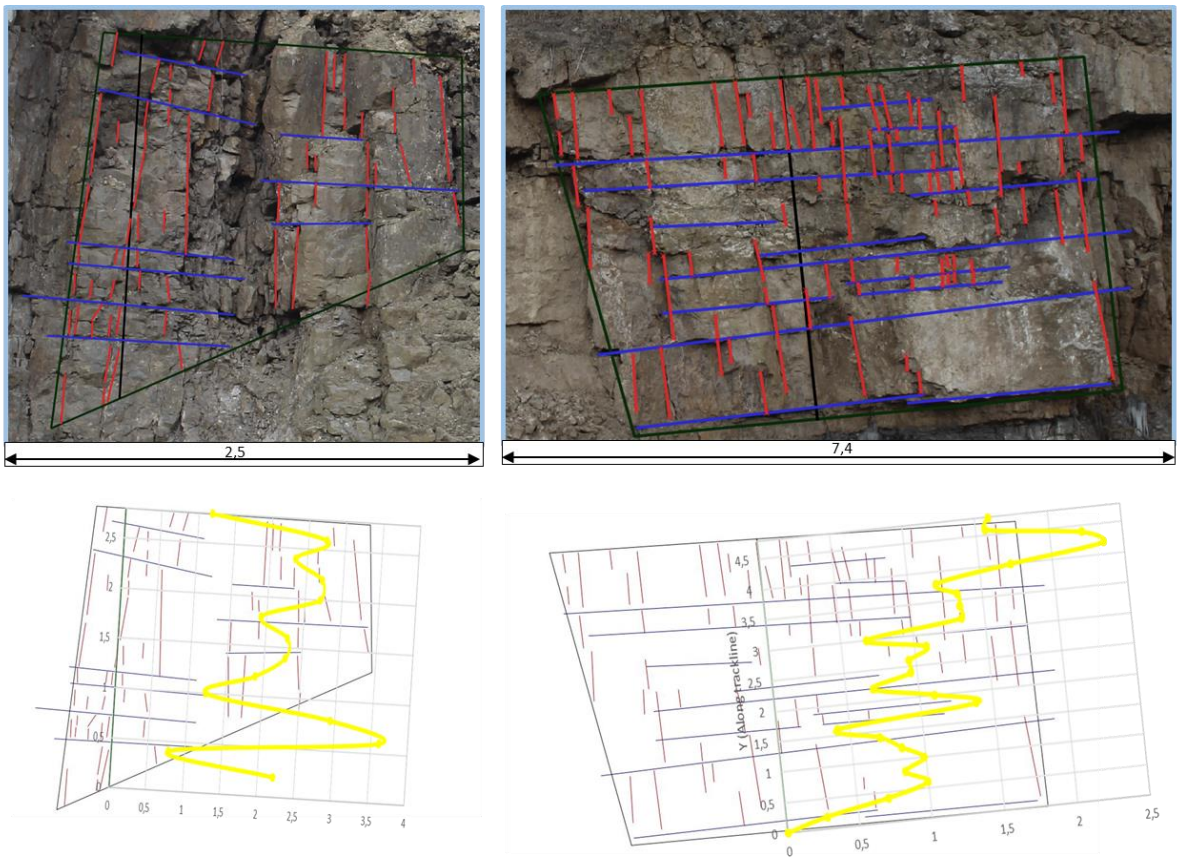

Appendix B. 8. Scanline analysis of HAS6 and HAS3

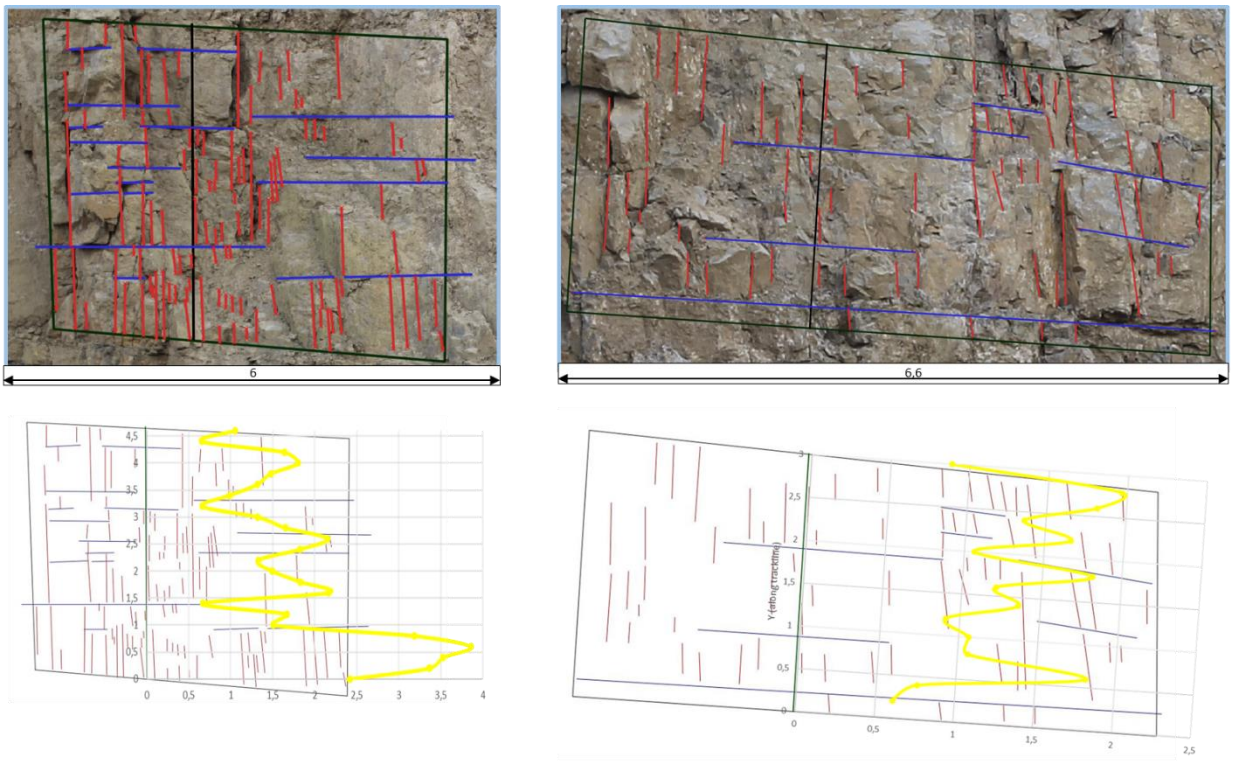

Appendix B. 9. Scanline analysis of HAS4 and HAS5

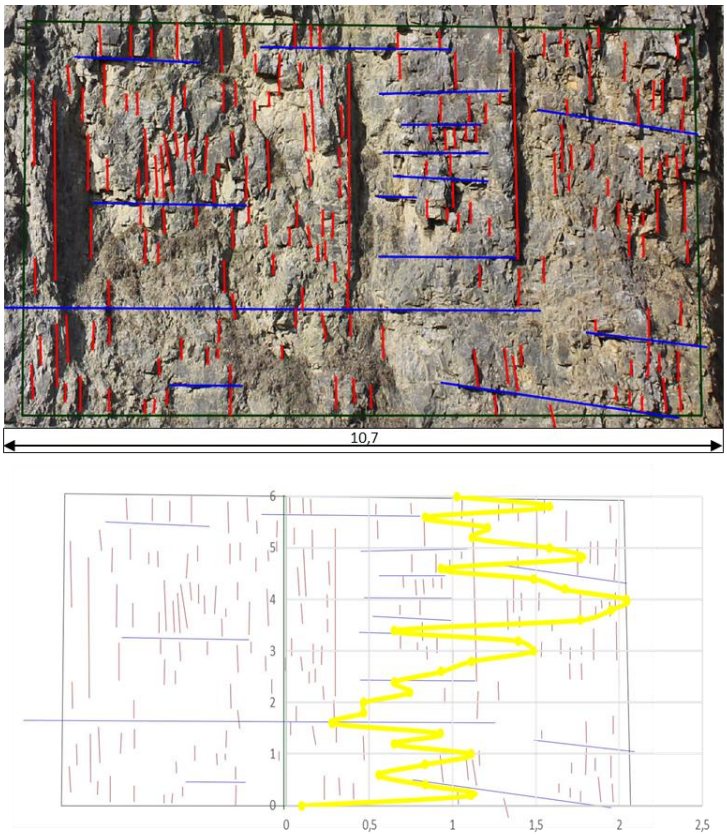

Appendix B. 10. Scanline analysis of HAS2

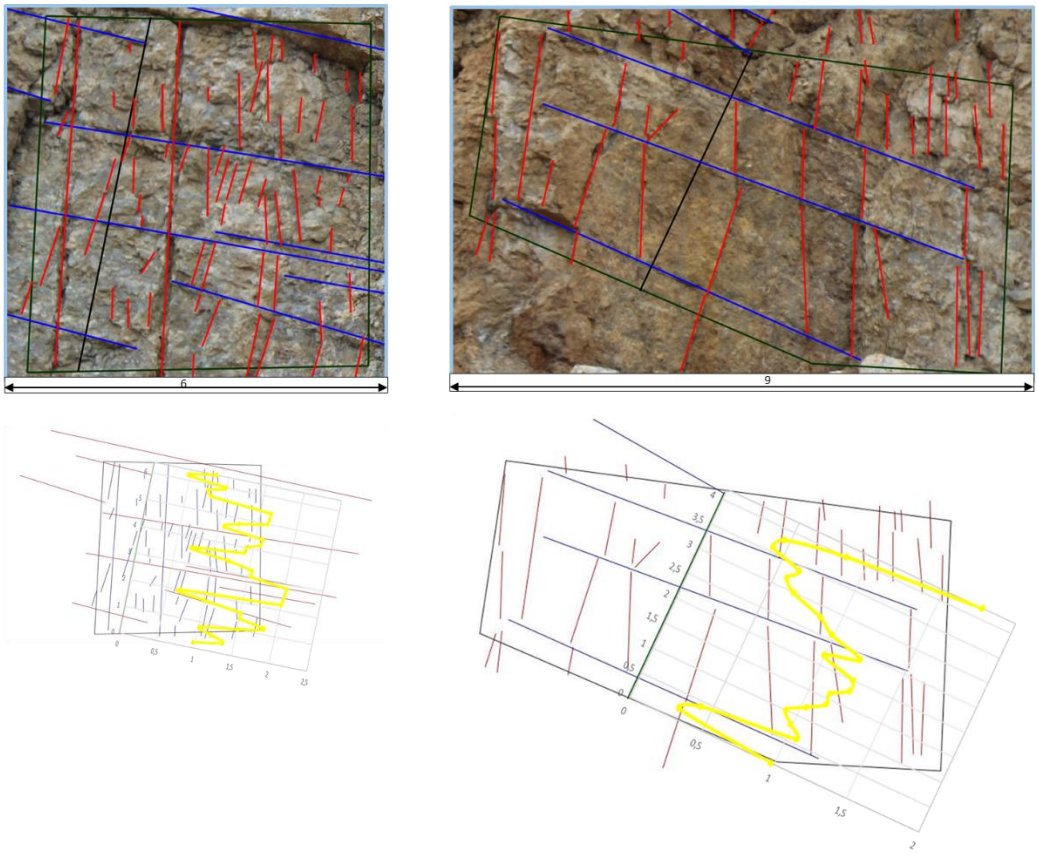

Appendix B. 11. Scanline analysis of BRE0 and BRE1

Appendix B. 12. Calculation of the damage zone based on the previous work done in the Hastenrath quarry (S.Becker et al) and literature on fault zone fracture density distribution

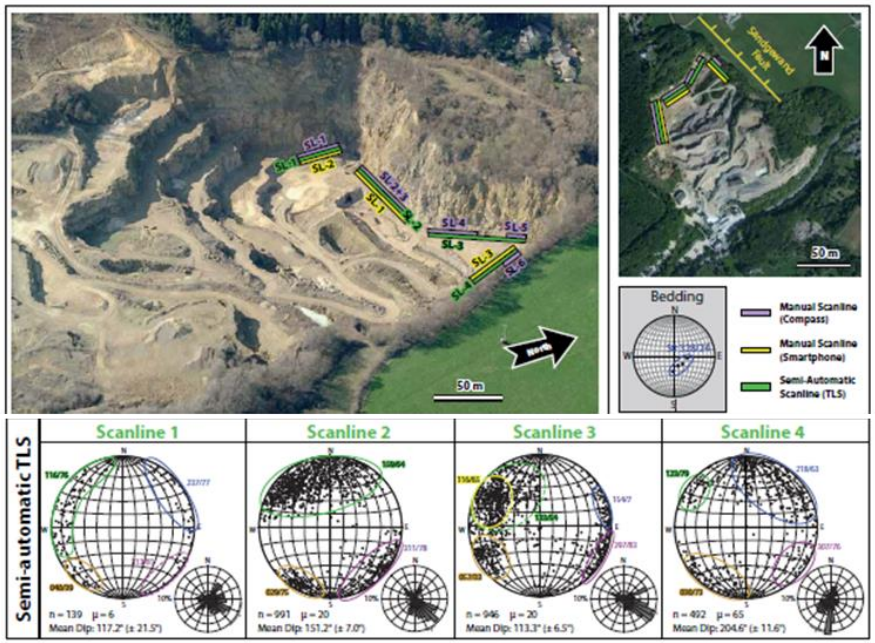

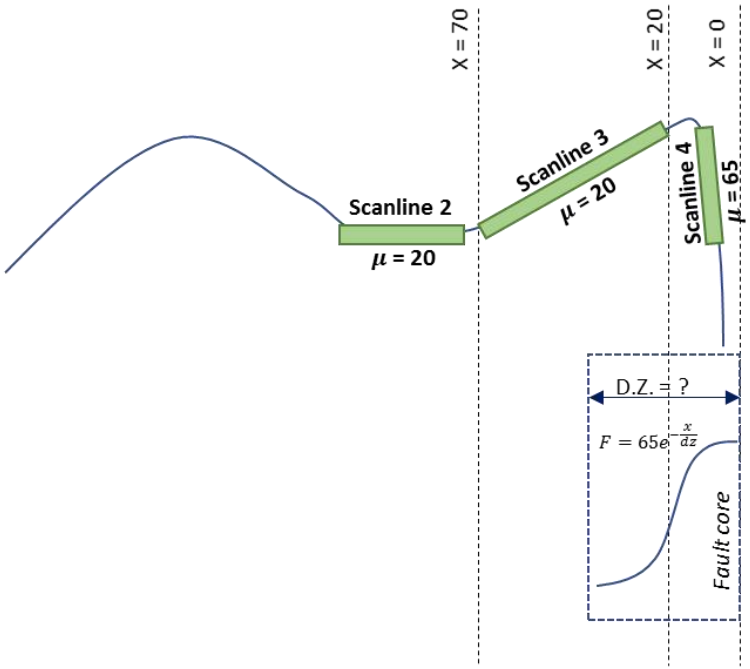

Explanation: Scanline 3 covers the distance between x=20 and x=70, which gives the distance to fault core. Assuming that the background fracture network is characterized by an average fracture density of 20 along this scanline, the damage zone width can be defined based on trial and error with the given equation.

1. Use the equation to calculate the fracture density based on distance to fault.
2. Generate the average fracture density between x=20 and x=70.
3. Vary the D.Z. and check when the average is approximately equal to 20. This gives a D.Z. width value of 35 meter.

Appendix C: Static model

Appendix C. 1. Well data available for each well (NE=not encountered, yellow = not found on Livelink EBN) (Geel, 2017)*

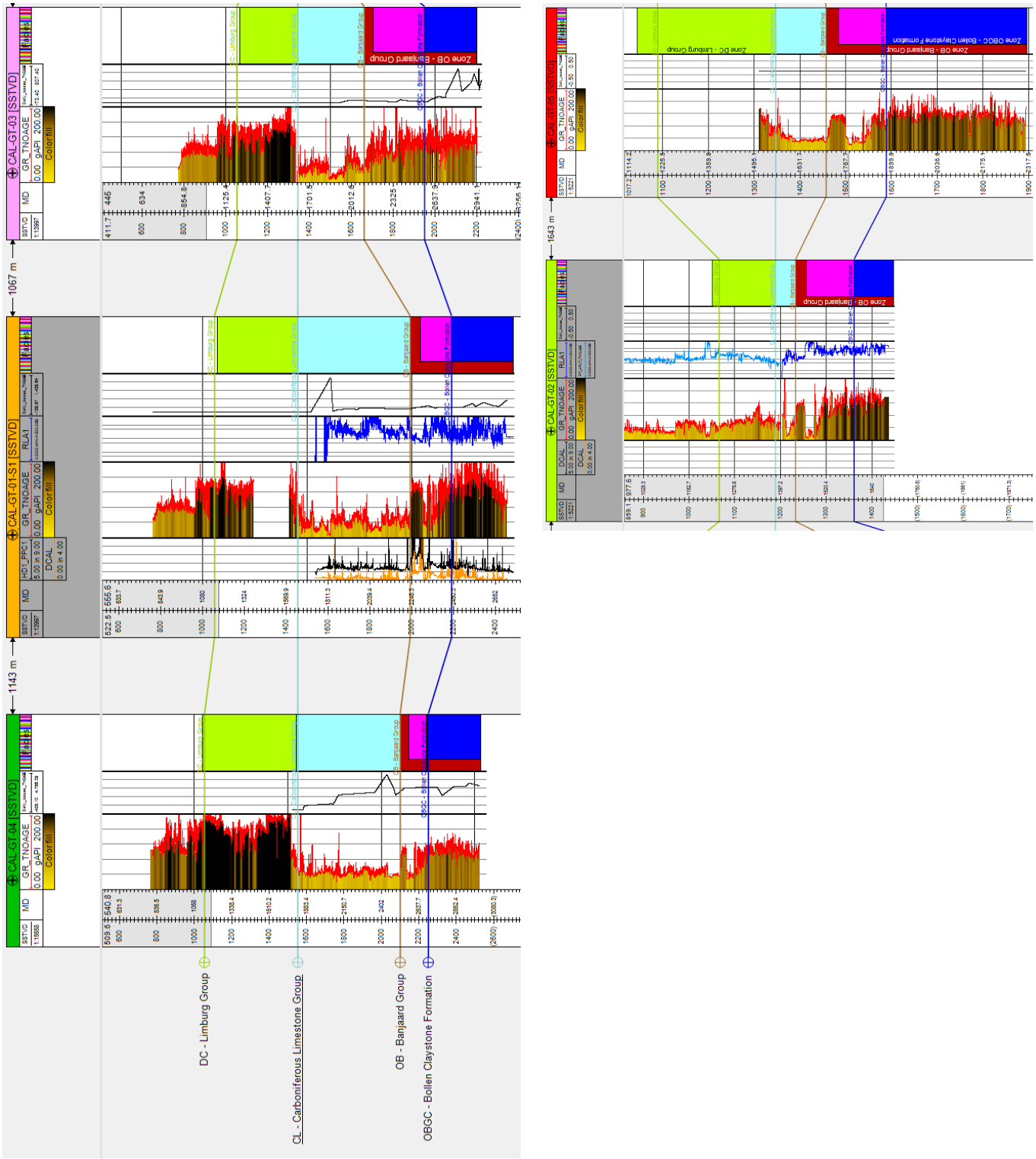

Appendix C. 2. Well section window (Petrel)

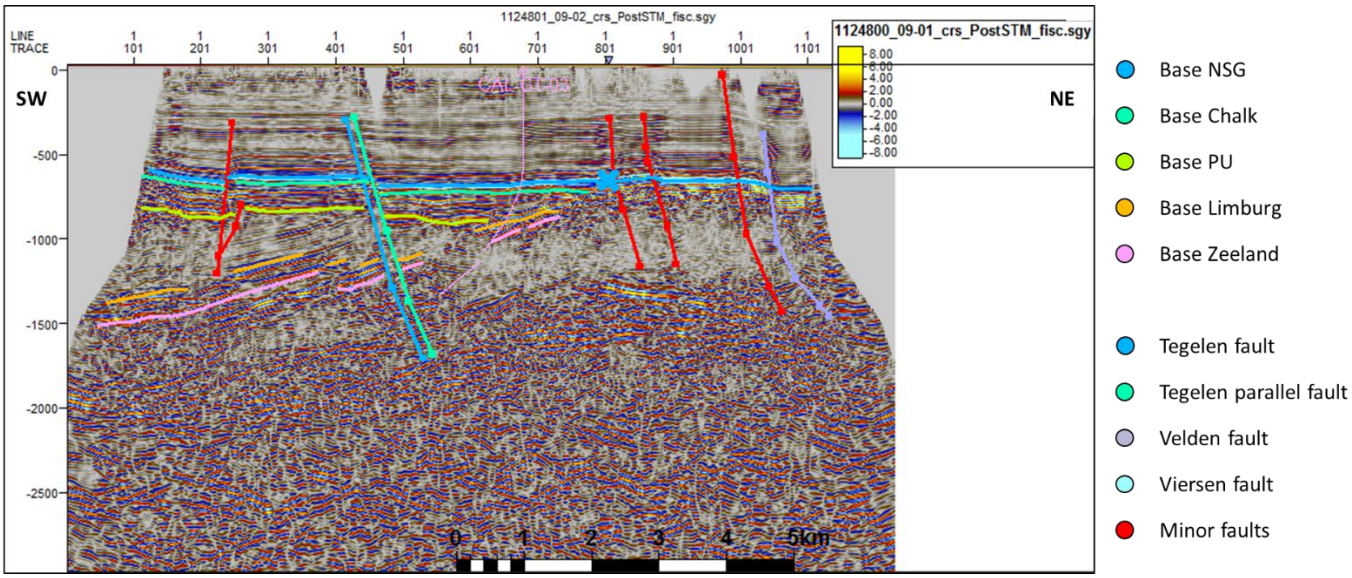

Appendix C. 3. Interpretation of the 09-01 seismic line including all the faults

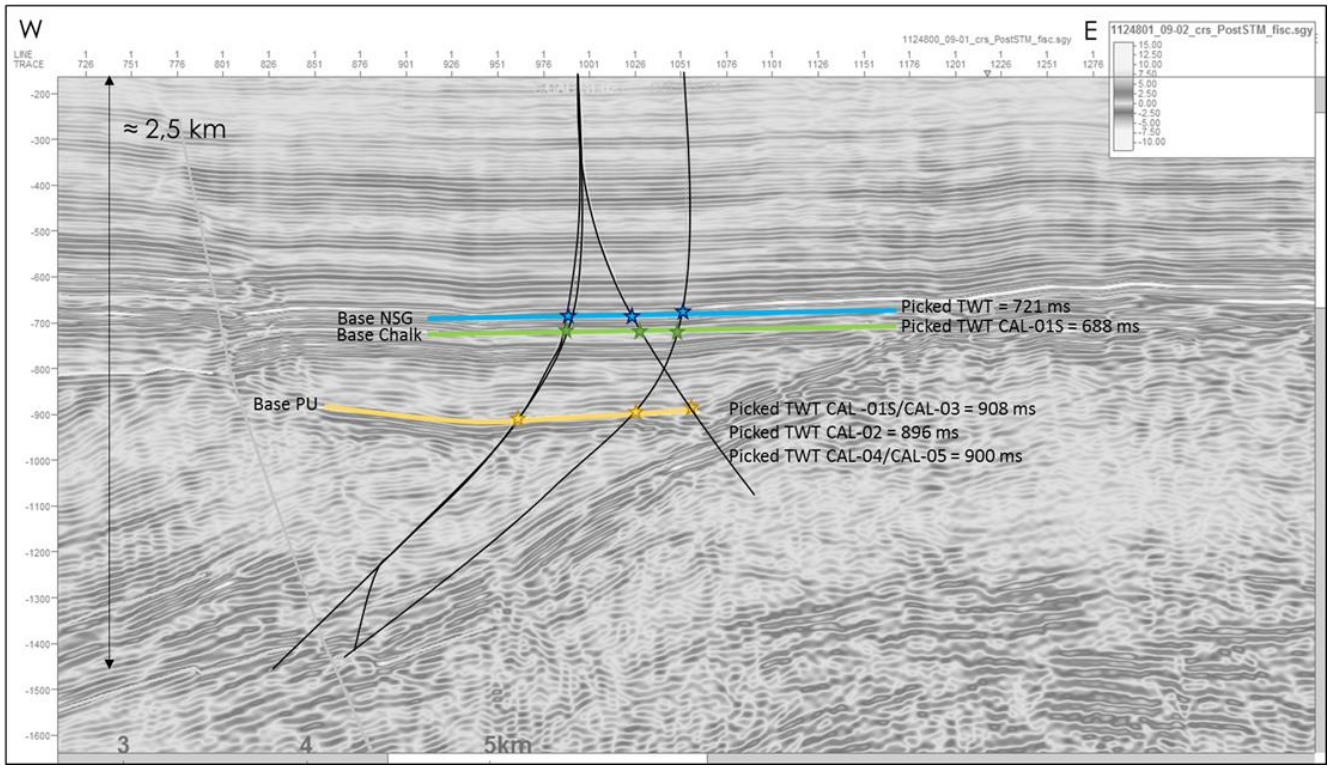

Appendix C. 4. TWT picks for the calculation of the pseudo interval velocity for the Base North Sea Group, Base Chalk and Base Permian Unconformity. The top two horizons show the same TWT in every well.

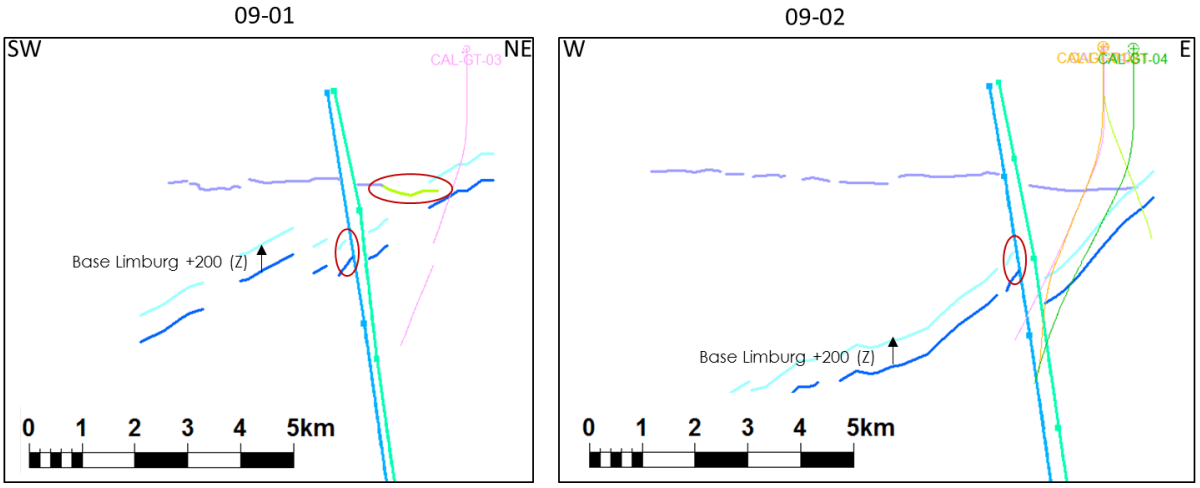

Appendix C. 5. The Base Limburg has a depth correction of +200m. To ensure no intersection with Base PU and the fault (which causes a problem in the structural modelling), the base PU and corrected base Limburg are slightly corrected (indicated by red circle).

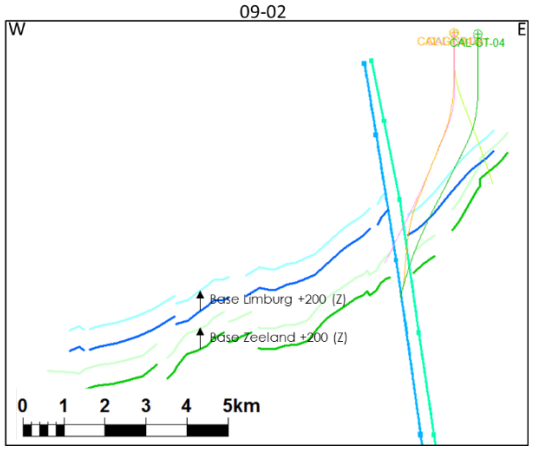

Appendix C. 6. Resulting depth corrected base Limburg and base Zeeland

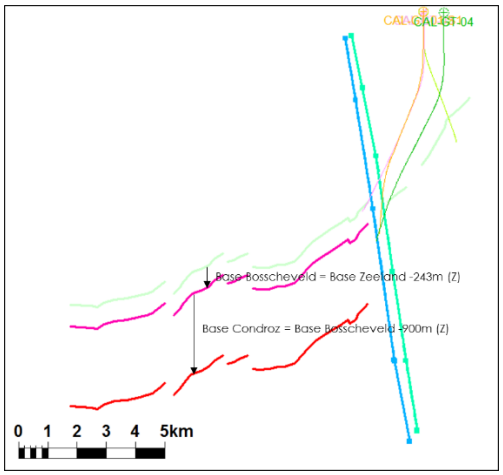

Appendix C. 7. Base Bosscheveld and Base Condroz are created based on the depth corrected Base Zeeland horizon.

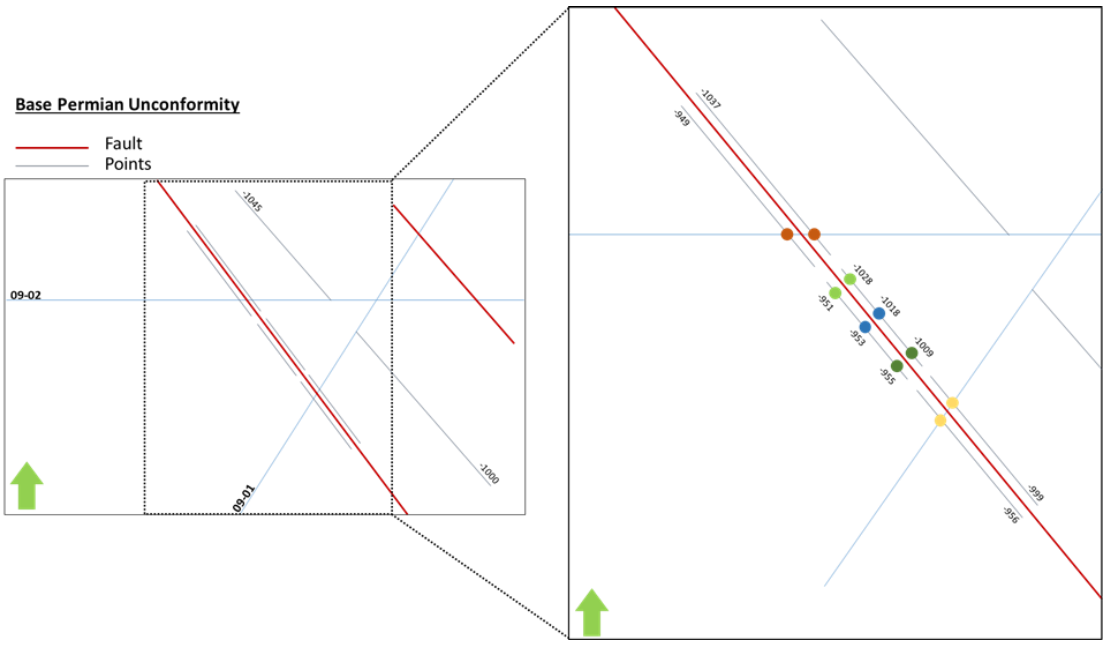

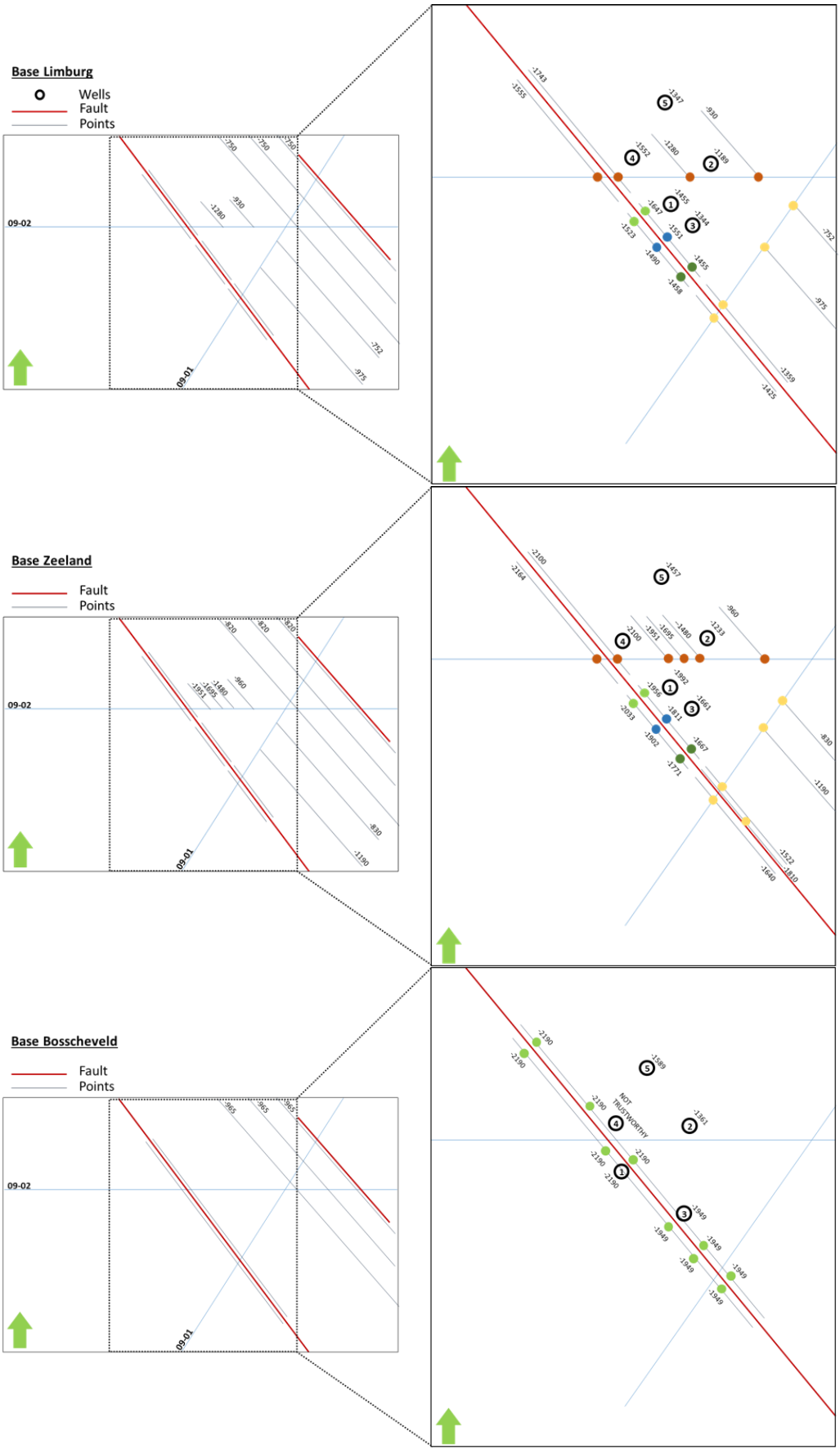
Base Limburg
Wells
Fault
Points
09-02
09-01
Base Zeeland
Fault
Points
09-02
09-01
Base Bosscheveld
Fault
Points
09-02
09-01
NOT TRUSTWORTHY

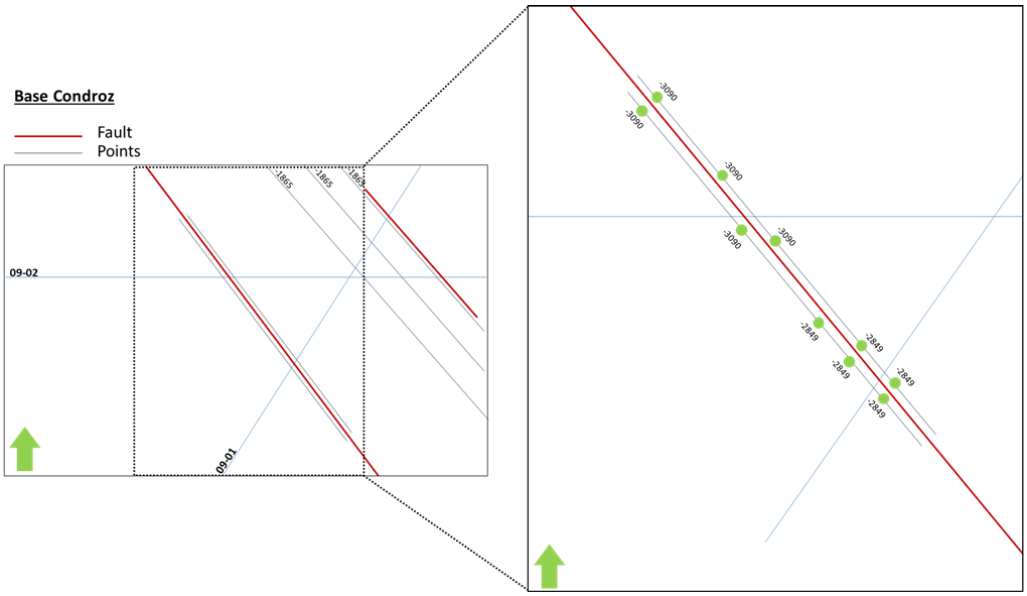

Explanation:
Use depth-corrected horizons as input for the structural model. Add grid points to edit the horizons in the structural model. The source of te values given to the grid points is given below:

1. Base PU/Base Limburg/Base Zeeland:
   - orange circle: value based on 09-02 line
   - yellow circle: value based on 09-01 line
   - Blue circle: average of yellow and orange value
   - Light green circle: average of blue and orange value
   - Dark green circle: average of blue and yellow value
   - Black circle: well top value
2. Base Bosscheveld:
   - Green circle: based on well top in CAL-GT-01S and CAL-GT-03
   - Black circle: well top value
3. Base Condroz:
   - Green circle: 900 meter below grid points of base Bosscheveld

Appendix C. 8. Schematic overview of grid point sets added to each surface in the structural model

	Fine grid	Coarse grid
Grid cell size (X,Y)	50m x 50m	100m x 100m
Total size model (X,Y)	16,2 km x 11,4 km	16,2 km x 11,4 km
J-direction	Parallel to Tegelen fault	Parallel to Tegelen fault
Fault type	Zig-zag	Zig-zag

Appendix C. 9. Fine grid and coarse grid properties

Appendix D: Well test analysis

Appendix D. 1. Interference test CWG

Parameters	Value	unit
h	884	m
u	0.0004	Pa.s
B	1	
re	3000	m
rw	0.1524	m

35 Hz		
Qav	0.0413	m3/s
delta Pav	157545	Pa
J	2.62349E-07	m3/s.Pa
K	1.86809E-13	m2
	0.187	D
	187	mD
40 Hz		
Qav	0.0480	m3/s
delta Pav	219333	Pa
J	2.18936E-07	m3/s.Pa
K	1.55897E-13	m2
	0.156	D
	156	mD
45 Hz		
Qav	0.0546	m3/s
delta Pav	288667	Pa
J	1.89042E-07	m3/s.Pa
K	1.3461E-13	m2
	0.135	D
	135	mD

50 Hz		
Qav	0.0607	m3/s
delta Pav	363500	Pa
J	1.66914E-07	m3/s.Pa
K	1.18854E-13	m2
	0.119	D
	119	mD
55 Hz		
Qav	0.0653	m3/s
delta Pav	428600	Pa
J	1.52455E-07	m3/s.Pa
K	1.08557E-13	m2
	0.109	D
	109	mD
60 Hz		
Qav	0.0675	m3/s
delta Pav	456125	Pa
J	1.47904E-07	m3/s.Pa
K	1.05317E-13	m2
	0.105	D
	105	mD

Explanation: Using formula (11) the permeability for each production step can be defined, assuming a constant drainage area. The flow rate and Δp have been deducted from the production data.

Appendix D. 2. Production test CAL-GT-01S

Appendix D. 3. Pressure, flow rate and PI curve as a function of time for the injection test CAL-GT-05.

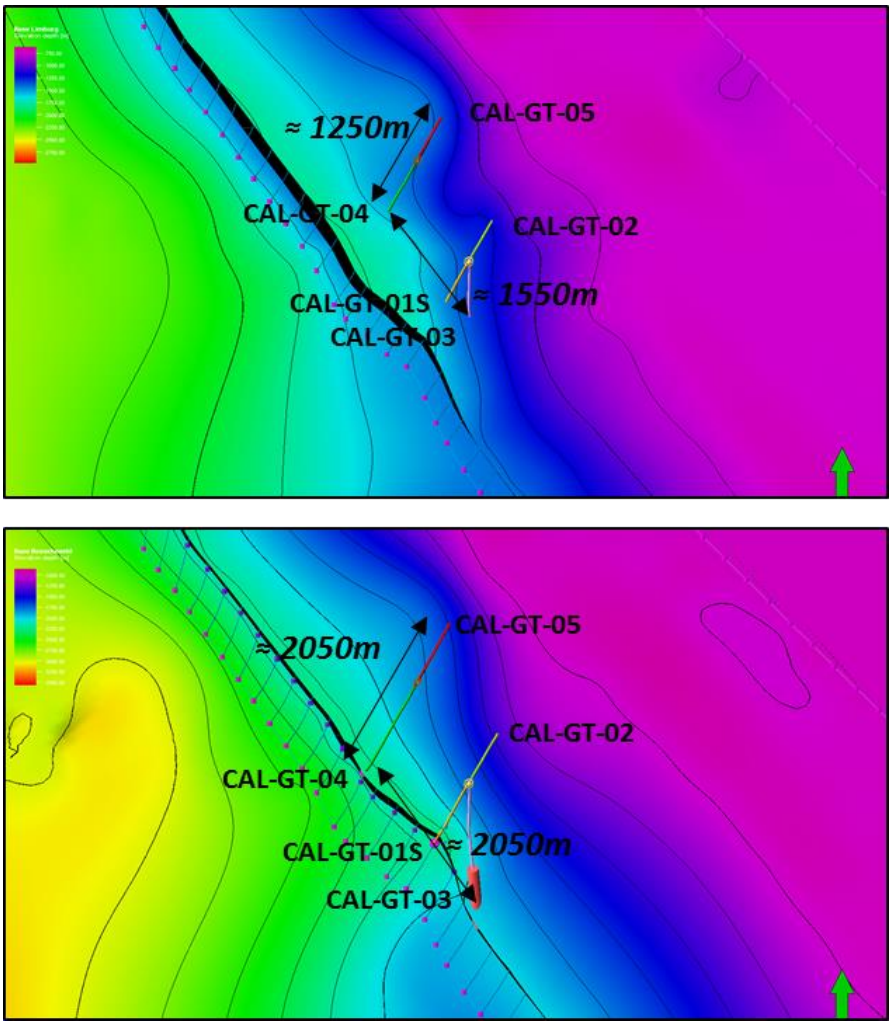

Appendix D. 4. Top view of wells on Base Limburg (top) and Base Bosscheveld (bottom)

Appendix E: Dynamic model

CAL-GT-01S	Top (MD)	Base (MD)
13 5/8 casing	0	826
9 5/8 liner	718	1576
7 liner	1508	1802

CAL-GT-03	Top (MD)	Base (MD)
13 5/8 casing	0	858
9 5/8 liner	744	1621
7 liner	1564	2410
perforations	1770	2410
plugback	2100	

CAL-GT-04	Top (MD)	Base (MD)
20 casing (24 not available in Petrel)	0	200
13 5/8 casing	0	809
9 5/8 liner	660	1730
7 liner	1632	2799
Perforations (5x6m)	1. 2547 2. 2557 3. 2747 4. 2759 5. 2771	1. 2553 2. 2563 3. 2753 4. 2765 5. 2776

CAL-GT-05	Top (MD)	Base (MD)
20 casing (24 not available in Petrel)	0	207
13 5/8 casing	0	825
9 5/8 liner	724.5	1547

Appendix E. 1. Well design for all wells

Appendix E. 2. Production data CWG and CLG (Main reference for history match) (1)

Appendix E. 3. Production data CWG and CLG (Main reference for history match) (2)

Appendix E. 4. Timeline development scenario2B

	Case	Development scenario	Components	Note
Scenario2B	Scenario2B	Development strategy 6	Standard 2B scenario: - No tracers - No temperature simulation	
Scenario 2B + alternative scenario 2B*	Scenario2BTemp	Development strategy 6_temp	Standard 2B scenario: Including tracers and temperature simulation	- Use this combination to model Scenario 2B and Scenario 2B* (the distance and value for CAL-GT-03 can be modified within the Kj formula) - Use this combination to model the temperature sensitivity (changing completion and changing temperature gradient)
Scenario 2B: excluding the CLG doublet	Scenario2BTemp_CWG	Development strategy 7_CWG	Variation on Scenario2BTemp: excluding CLG doublet	Use this combination to model the sensitivity of interference
Scenario2B: multiplying Ki/Kj/Kk by 1,5	Scenario2BTemp_multiplier	Development strategy 6_temp	Variation on Scenario2BTemp: including multiplier for Kj/Ki/Kk	Use this combination to model the sensitivity of a multiplier for Kj/Ki/Kk

Explanation: Scenario2B is the best case scenario with the final permeability configuration. The remaining scenario's (Base Case, Scenario 1A, Scenario 1B, Scenario 2A) have also been tested in Petrel. Each scenario has it's own case name, corresponding with the scenario name. The table above specifies the different cases made for scenario 2B, because these were necessary to include different components or test different sensitivities.

Appendix E. 5. Overview of cases

			Kh					
			Reference (max thickness *K)	CAL-01	CAL-03	CAL-04	CAL-05	CAL-05
		Total height		884	768	439	642	510
Zones	*Zeeland*	High permeable layer 1 (120m)	*780*		3879		715	715
		Zone (100m)	*320*	262.4	320			
		High permeable layer 2 (50m)	*325*	325	21550			
		Zone (rest)		854.4	150.4			
	Bosscheveld	Pont d'Arcole		0	0	0	0	0
		Zone (80m)	*256*	256	256	256	256	256
		High permeable layer 3 (50m)	*160*	160	160	160	160	160
		Zone (rest)		217.6	505.6	64	6.4	6.4
	Condroz	Zone (40m)	*128*	128	128	128	128	128
		High permeable layer 4 (50m)	*2700*	2700	2700	2700	2700	2700
		Zone (80m)	*256*	256	256	256	256	256
		High permeable layer 5 (50m)	*2700*	2700	2700	2700	2700	2700
		Zone (rest)		342.4	300.8	416	675.2	252.8
		Average Kh (mD.m)		683.48	2531.22	742.22	759.66	717.42
		Average Kh (m3)		6.83E-13	2.53E-12	7.42E-13	7.60E-13	7.17E-13

Explanation: Kh is the average of the individual Kh's calculated for each zone in each well. Not every well is completely open hole or perforated along the Zeeland formation.

Appendix E. 6. Kh calculation

Component scenario 2B	Petrel parameter
High K zone around CAL-GT-03 in high K layers of the Zeeland fm.	SC2B_K_J=If(Zone=0 And Facies=385,If(**Distance_from_CAL_GT_03<800,2000**,30),
High K layer 1 & 2 [Zeeland fm]	SC2B_K_J=If(Zone=0 And Facies=385,If(Distance_from_CAL_GT_03<800,2000,**30**),
High K layer 3 [Bosscheveld fm]	SC2B_highKlayerBosscheveld=If(Distance<100,250,15)
High K layer 4 & 5 [Condroz group]	SC2B_highKlayer=250
Background fracture networks	SC2B_background=15
Tegelen fault core	If(Distance<100,Pow(SC2A_Fracture_density,5)*500
Faults parallel to tegelen fault	SC2B_parallelfaults=50

Petrel Explanation: Scenario 2B consists of multiple components, the table above provides an overview of the component and the corresponding petrel parameter in the calculator. In order to distinguish the different zones, they have been numbered in the "Zone" property. All high permeable layers are characterized by zone=0. The "Distance" property defines the distance to the fault.

The figure below provides an overview of the calculator. All different zones are bundled in the SC2B_K_J property. For the temperature modelling, the thermal conductivity of rock+fluid has to be created as a property. This property can be added in the grid subsection in the simulation case in the keyword (THCONR).

Eclipse100 explanation: To model temperature multiple keywords have to be manually added in the Eclipse100 directory;

- TEMP (in the RUNSPEC section)
- SPECHEAT (specific heat of the fluid, in PROPS section)
- SPECROCK (specific heat of the rock, in PROPS section)
- RTEMPVD (specifies temperature gradient, in SOLUTION section)
- WTEMP (specifies injection temperature, must be added below WELSPECS in SCHEDULE section).

SC2B_Fracture_density=If(Zone=0 OR Zone=1 OR Zone=4, 0, If(Distance>0 And Distance<100,Exp(-Distance/100),If(Distance>200 And Distance<300,0.6,If(Distance>400 And Distance<500,0.6, If(Distance>600 And Distance<700,0.6,If(Distance>800 And Distance<900,0.6,If(Distance>1000 And Distance<1100,0.6,If(Distance>1200 And Distance<1300,0.6,If(Distance>1400 And Distance<1500,0.6,If(Distance>1600 And Distance<1700,0.6,If(Distance>1800 And Distance<1900,0.6,If(Distance>2000 And Distance<2100,0.6,If(Distance>2200 And Distance<2300,0.6,If(Distance>2400 And Distance<2500,0.6,If(Distance>2600 And Distance<2700,0.6,0))))))))))))))

SC2B_highKlayer=250

SC2B_highKlayerBosscheveld=If(Distance<100,250,15)

SC2B_parallelfaults=50

SC2B_background=15

SC2B_K_J=If(Zone=0 And Facies=385,If(Distance_from_CAL_GT_03<800,2000,30), If(Zone=0 And Facies=399,SC2B_highKlayerBosscheveld, If(Zone=0,SC2B_highKlayer, If(Zone=1 or Zone=4,0, If(Distance>0 And Distance<100,Pow(SC2A_Fracture_density,5)*500,If(Distance>200 And Distance<300,SC2B_parallelfaults,If(Distance>400 And Distance<500,SC2B_parallelfaults, If(Distance>600 And Distance<700,SC2B_parallelfaults,If(Distance>800 And Distance<900,SC2B_parallelfaults,If(Distance>1000 And Distance<1100,SC2B_parallelfaults,If(Distance>1200 And Distance<1300,SC2B_parallelfaults,If(Distance>1400 And Distance<1500,SC2B_parallelfaults,If(Distance>1600 And Distance<1700,SC2B_parallelfaults,If(Distance>1800 And Distance<1900,SC2B_parallelfaults,If(Distance>2000 And Distance<2100,SC2B_parallelfaults,If(Distance>2200 And Distance<2300,SC2B_parallelfaults,If(Distance>2400 And Distance<2500,SC2B_parallelfaults,If(Distance>2600 And Distance<2700,SC2B_parallelfaults,SC2B_background))))))))))))))))))

SC2B_K_I=SC2B_K_J/10

SC2B_K_K=SC2B_K_J/10

Thermal_cond=If(Zone=1 Or Zone=4,0,224)

THCONR: 224 kJ/m/day/K (source: TNO model by R.Fonseca)

SPECROCK: specific heat for dolomite (source: TNO model by R.Fonseca)
60.0 2650
80.0 2700
100.0 2750
/

SPECHEAT: specific heat for water (source: thermodynamic properties of water, booklet from IGA course)
10.0 0.5 4.20 0.5
50.0 0.5 4.18 0.5
100.0 0.5 4.22 0.5
/

RTEMPVD: temperature gradient (33 C/km with 11 C surface temperature)
1 11
1000 44
2000 77
3000 110 /

WTEMP : based on production data

Appendix E. 7. Modelling specifications for permeability scenario 2B (and variations) in Petrel

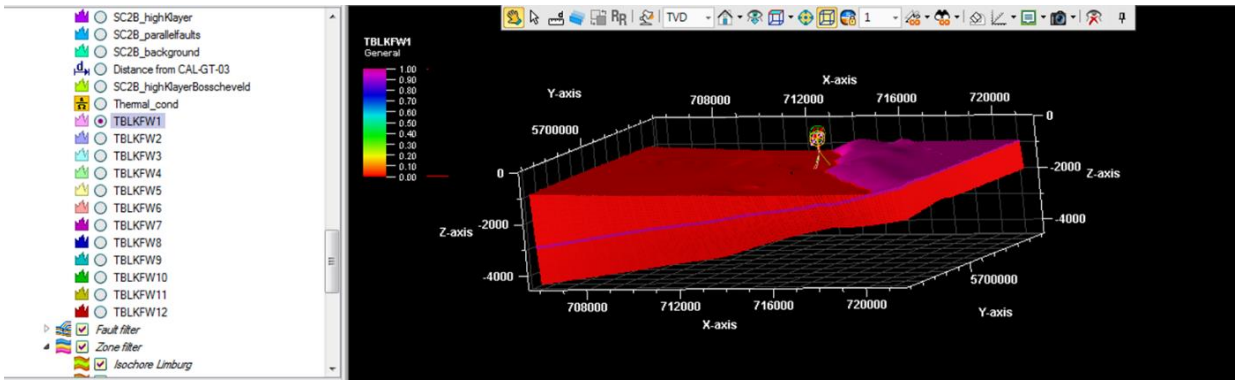

Petrel Explanation: The tracers are added for every zone by using the property calculator in combination with the filter. The tracer has a value of 1 for a specific zone and a value of 0 for the other zones. Petrel assumes the tracer to be initially in place in the reservoir and the injected water moves the tracer. This means that it provides an indication for produced water per zone, but not for injected water. Each tracer can be added in the grid subsection of the simulation case in the keyword TBLKF*. The * changes into the name of the tracer, which cannot exceed 3 characters.

Eclipse Explanation: To model the tracers mulitple keywords have to be manually added in the Eclipse100 directory;

- TRACERS (in RUNSPEC)
- TRACER (in PROPS)
- WTPR* (tracer production rate, in SUMMARY)
- WTPT* (tracer production total, in SUMMARY)
- RUNSUM / SEPARATE (tabulates data in separate RSM file, can be imported in excel, in SUMMARY section)

Appendix E. 8. Modelling specifications for adding tracers in Petrel

Tracer	Zone
	Limburg
W1	High permeable layer 1 (120m)
W2	Zone (100m)
W3	High permeable layer 2 (50m)
W4	Zone (rest)
	Pont d'Arcole
W5	Zone (80m)
W6	High permeable layer 3 (50m)
W7	Zone (rest)
W8	Zone (40m)
W9	High permeable layer 4 (50m)
W10	Zone (80m)
W11	High permeable layer 5 (50m)
W12	Zone (rest)

Appendix E. 9. Tracer and corresponding zone in the model (Limburg and Pont d'Arcole do not require tracer, because N/G=0)

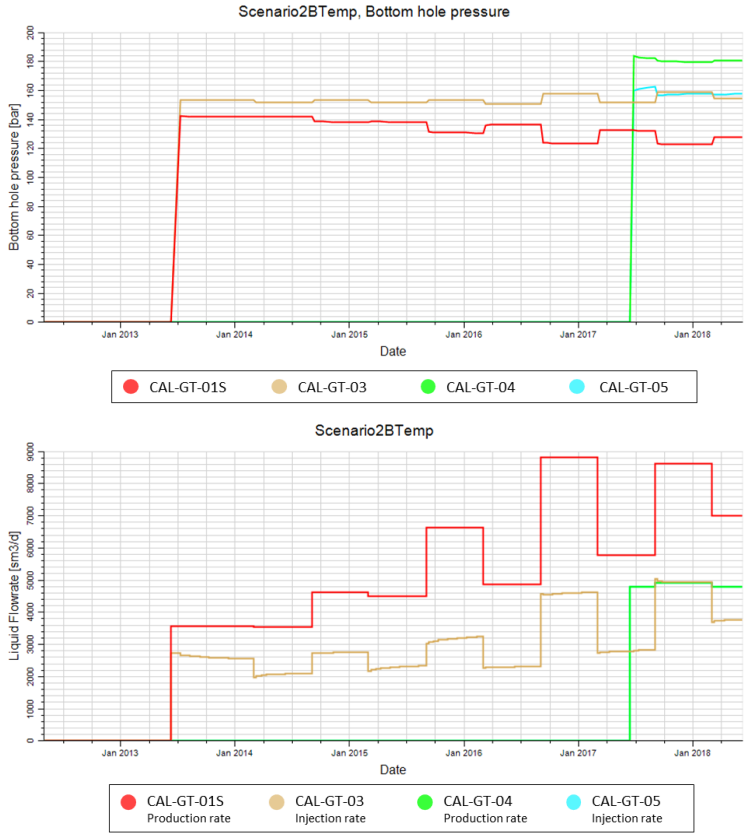

Appendix E. 10. Case: Scenario2BTemp. BHP and flow rate plot of Scenario 2B with an equal radius (800m) and a low permeability value (Kj=500 mD)*

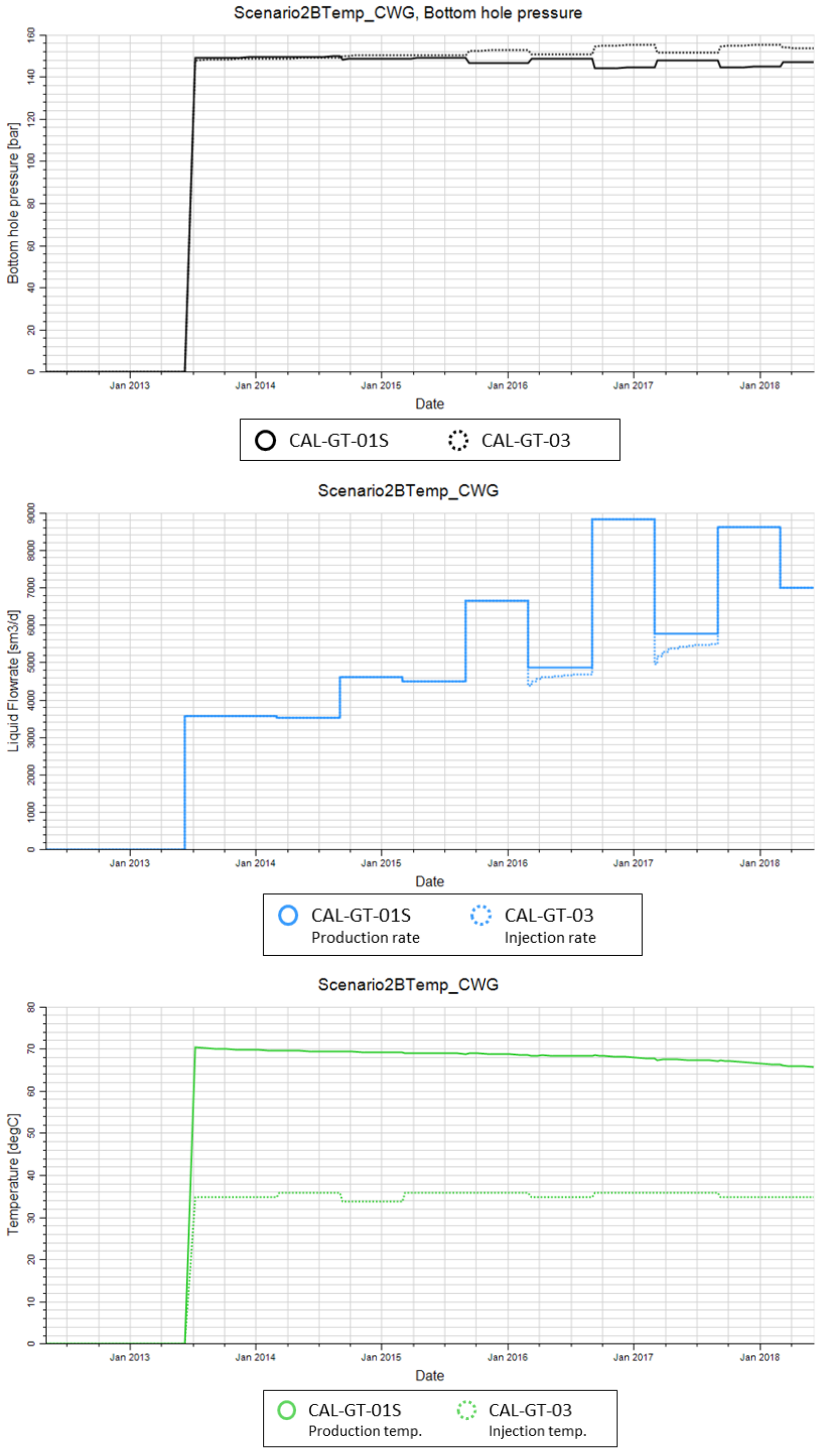

Appendix E. 11. Case: Scenario2BTemp_CWG. BHP, flowrate and temperature plot

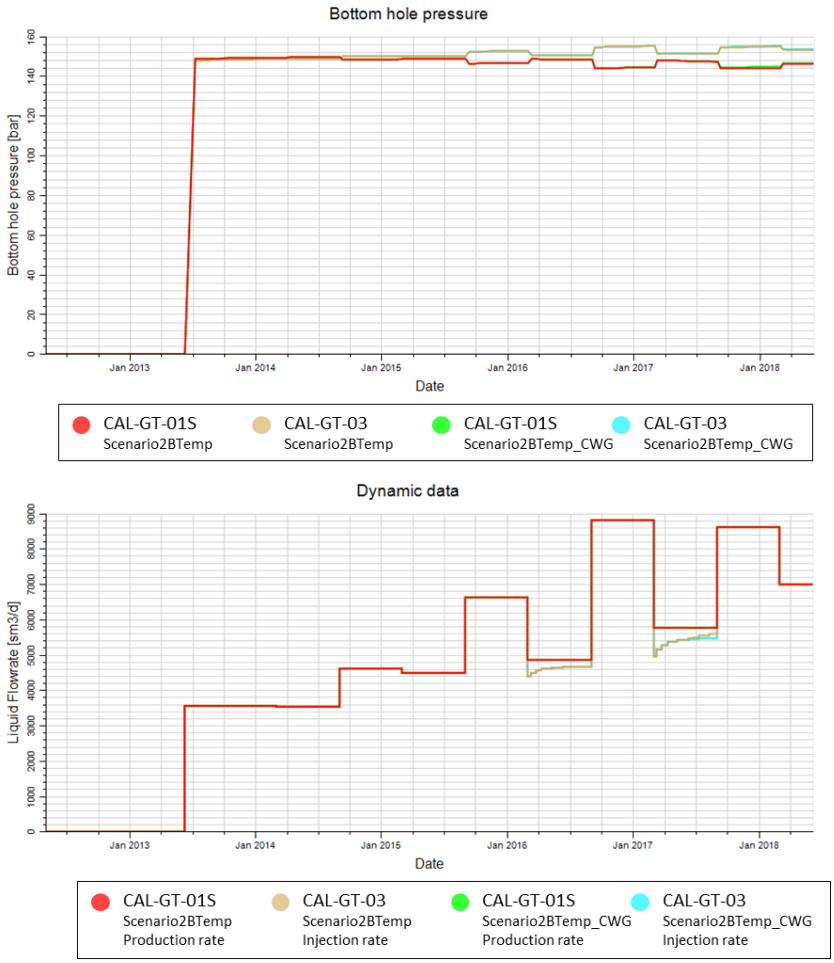

Appendix E. 12. Case: Scenario2BTemp_CWG & Scenario2BTemp. Comparison of BHP and flow rate plot

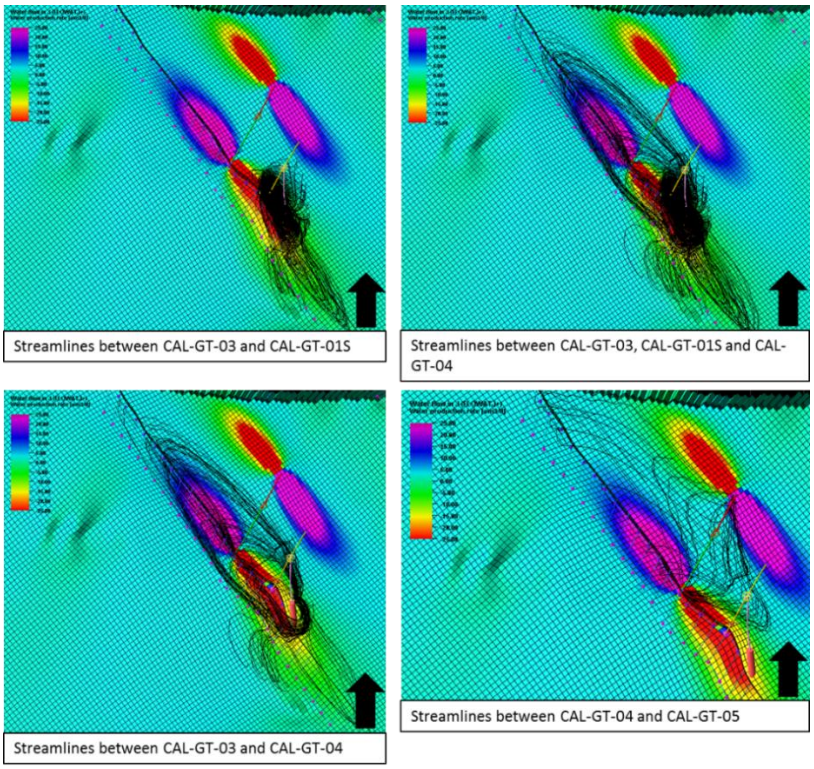

Appendix E. 13. Case: Scenario2BTemp. Streamline plot on 08/07/2017 showing the interference between the different wells in Scenario2B (background is the waterflow in J direction in high permeable layer 4 in the Condroz group)

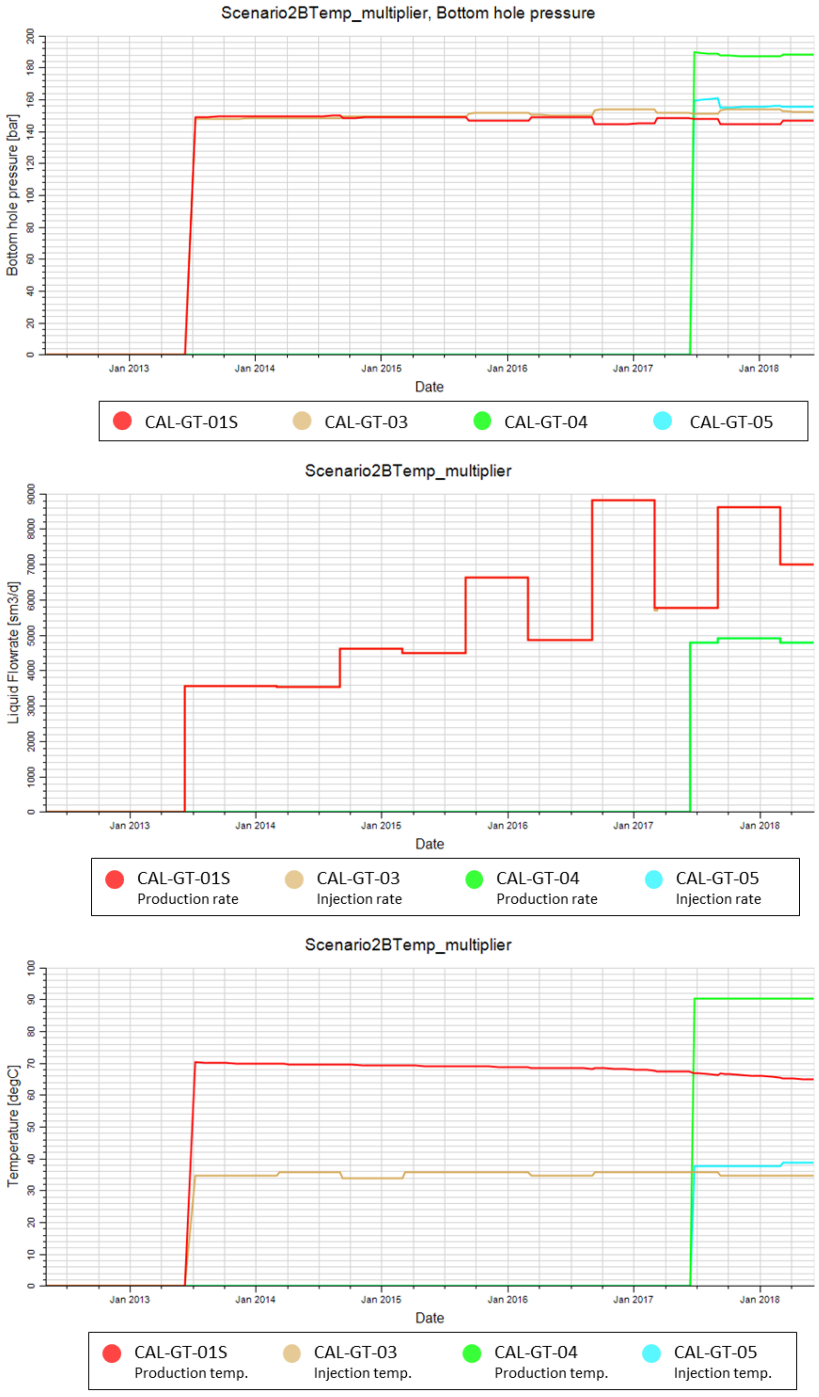

Appendix E. 14. Case: Scenario2BTemp_multiplier. BHP, flow rate and temperature plot

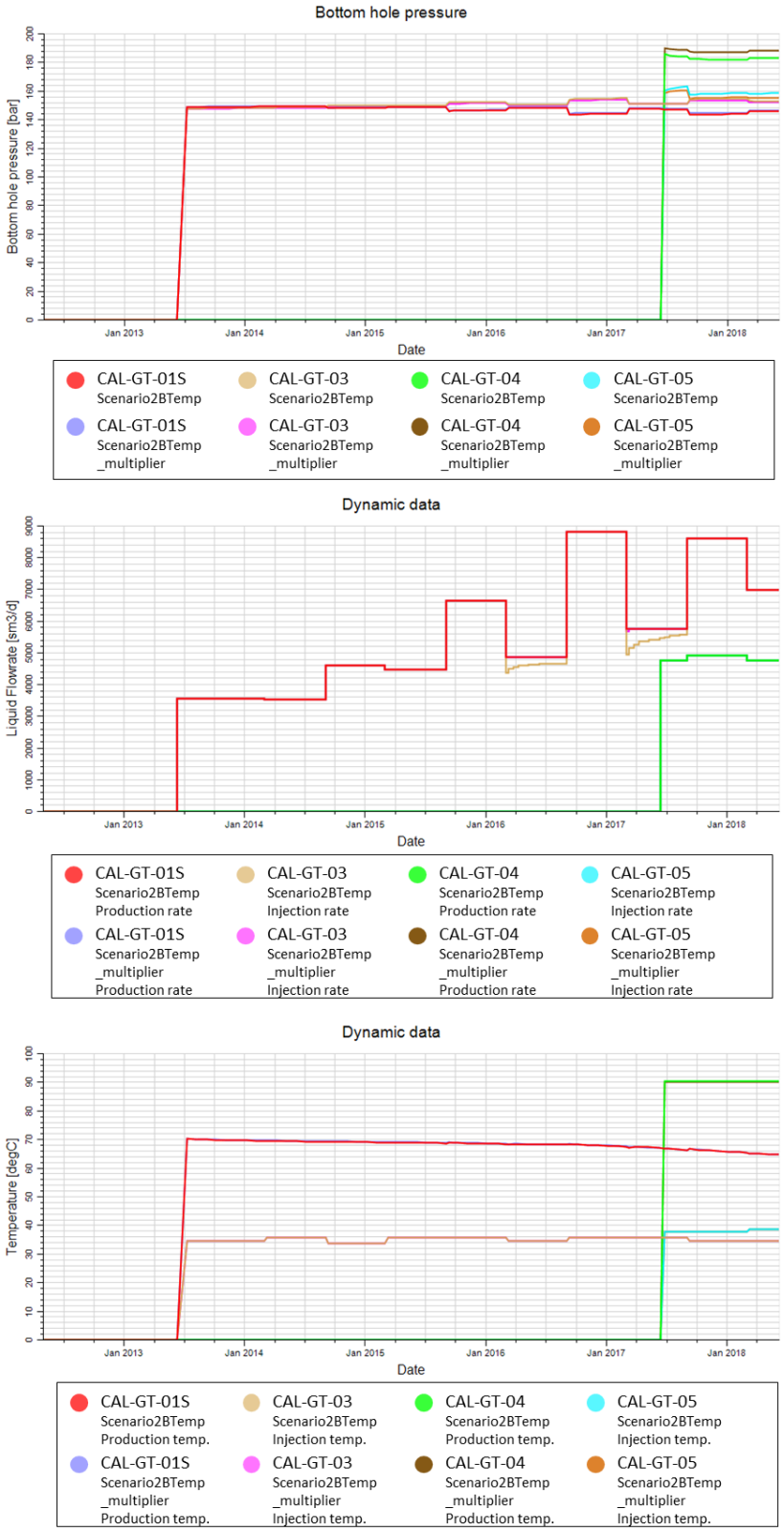

Appendix E. 15. Case: Scenario2BTemp_multiplier & Scenario2BTemp. Comparison of BHP, flow rate and temperature plot

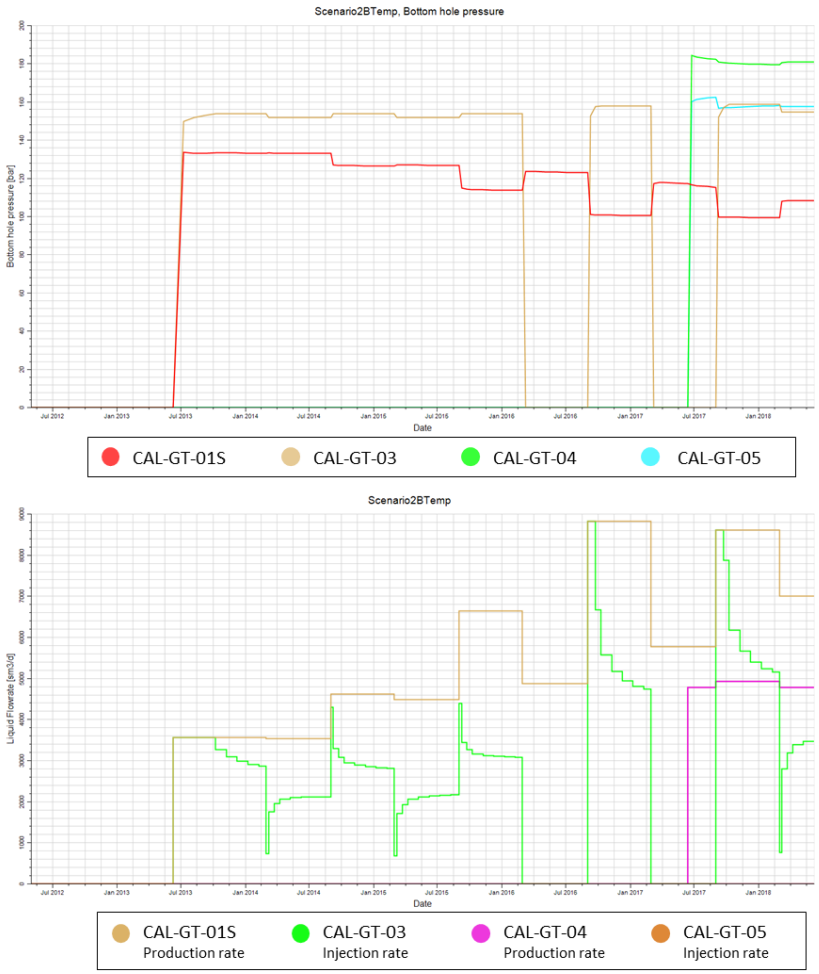

Appendix E. 16. Case: Scenario2BTemp. BHP and flow rate plot of Scenario2B with a small radius (250m) and a high permeability value (Kj=12 D)*

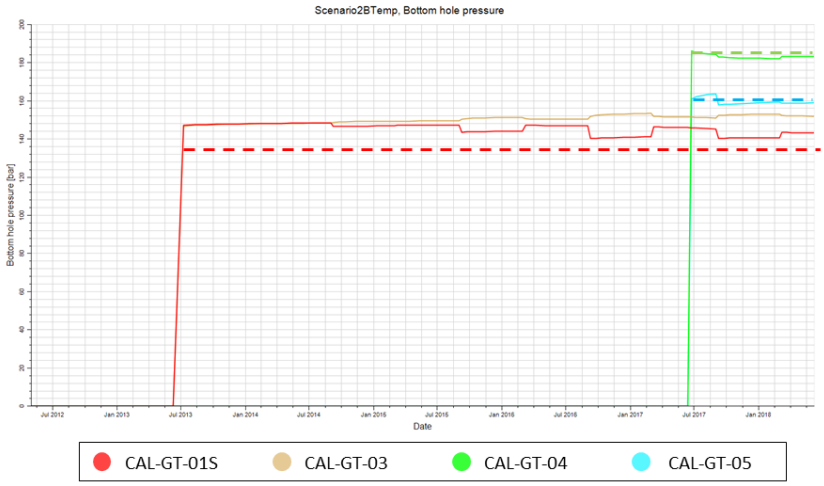

Appendix E. 17. Case: Scenario2BTemp. BHP, flow rate and temperature plot of Scenario2B with a small radius (370m) and a high permeability value (Kj=7 D)*

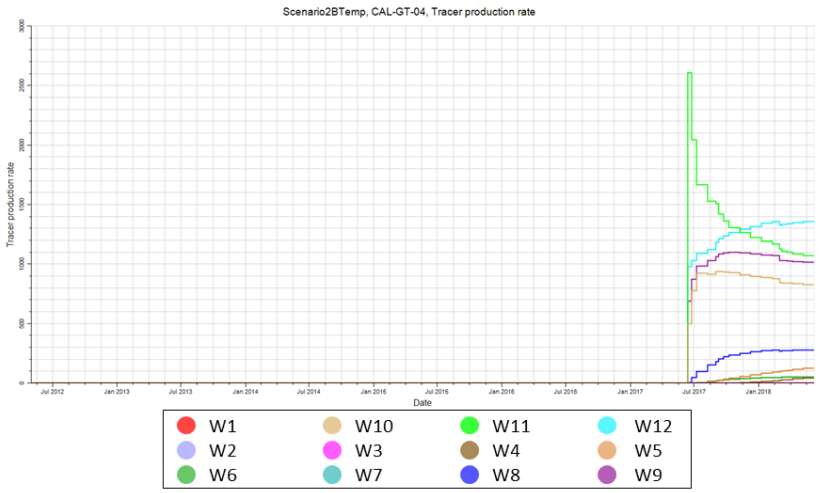

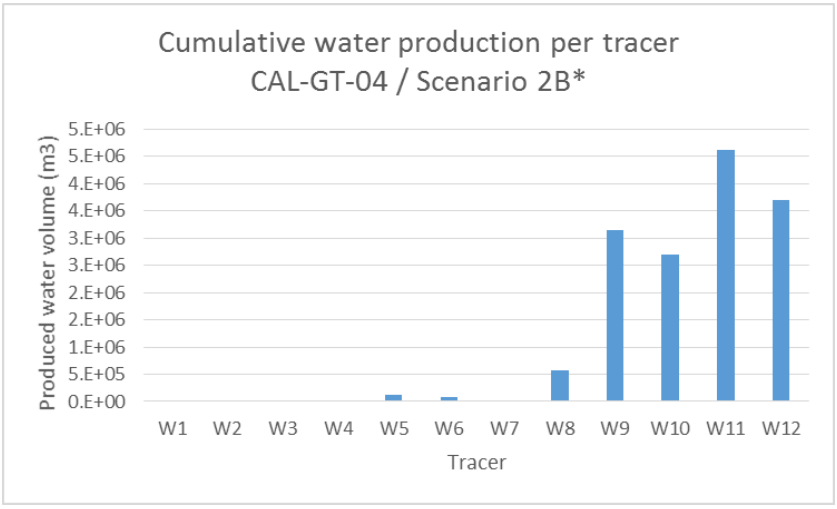

Appendix E. 18. Case: Scenario2BTemp. Tracer and cumulative water production plot for CAL-GT-04 in Scenario2B with a small radius (370m) and a high permeability value (Kj=7 D)*

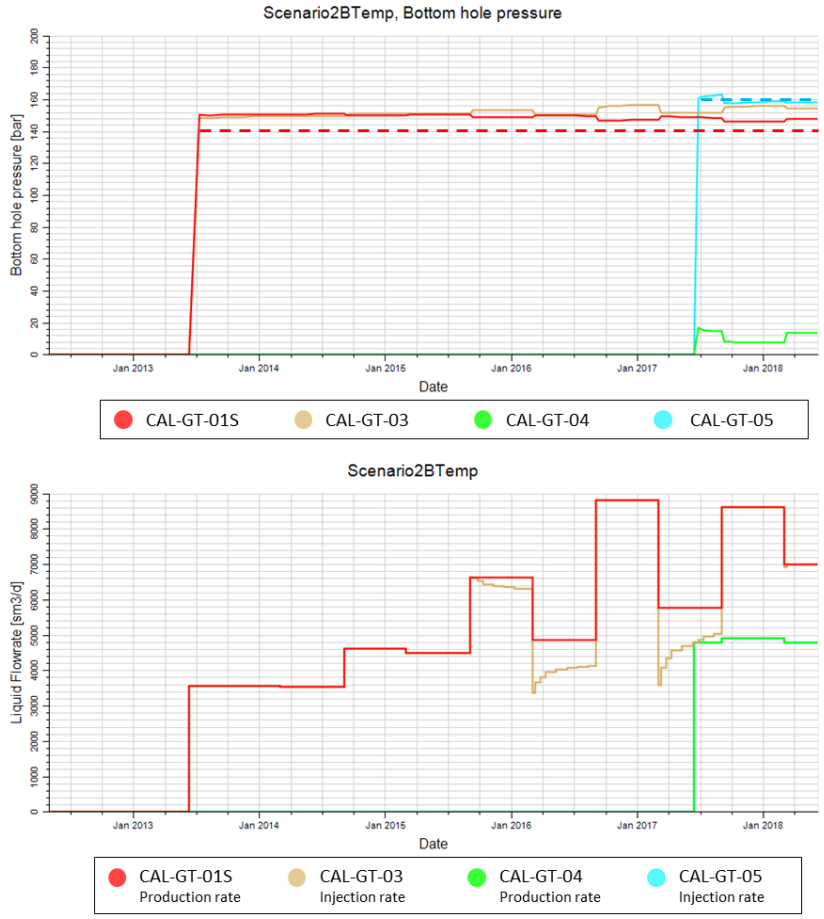

Appendix E. 19. Case: Scenario2BTemp. BHP and flow rate plot of Scenario2B with changed completion (CAL-GT-01S stimulated with a hydraulic fracture and CAL-GT-04 with a plugback)

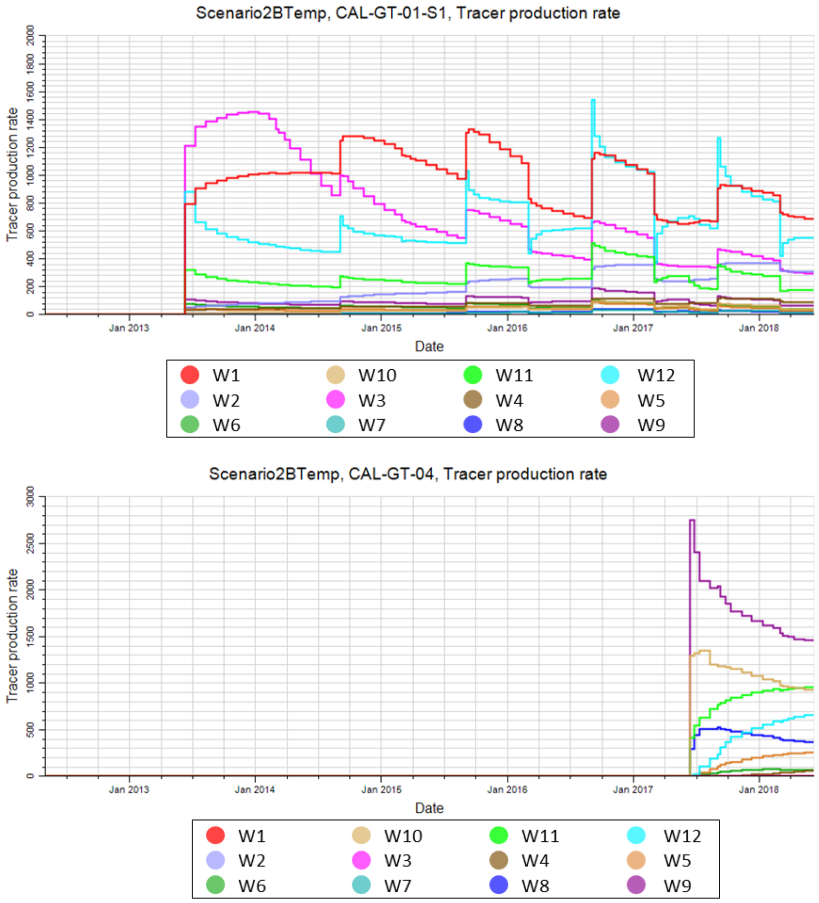

Appendix E. 20. Case: Scenario2BTemp. Tracer production of Scenario2B with changed completion (CAL-GT-01S stimulated with a hydraulic fracture and CAL-GT-04 with a plugback)

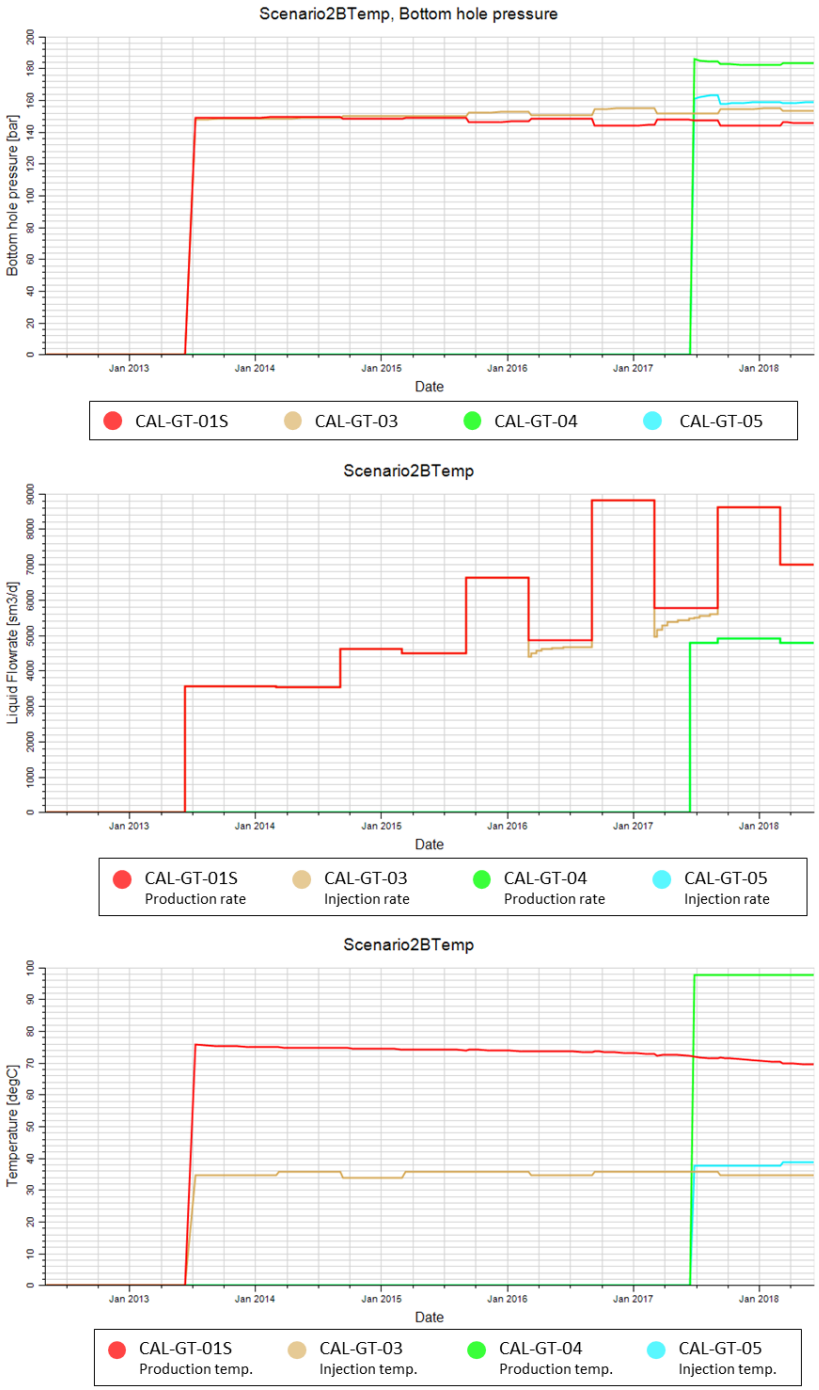

Appendix E. 21. Case: Scenario2BTemp. BHP, Flow rate and temperature profile for Scenario2B with an increased reservoir temperature gradient (36 ˚C/km, surface T = 11 C)

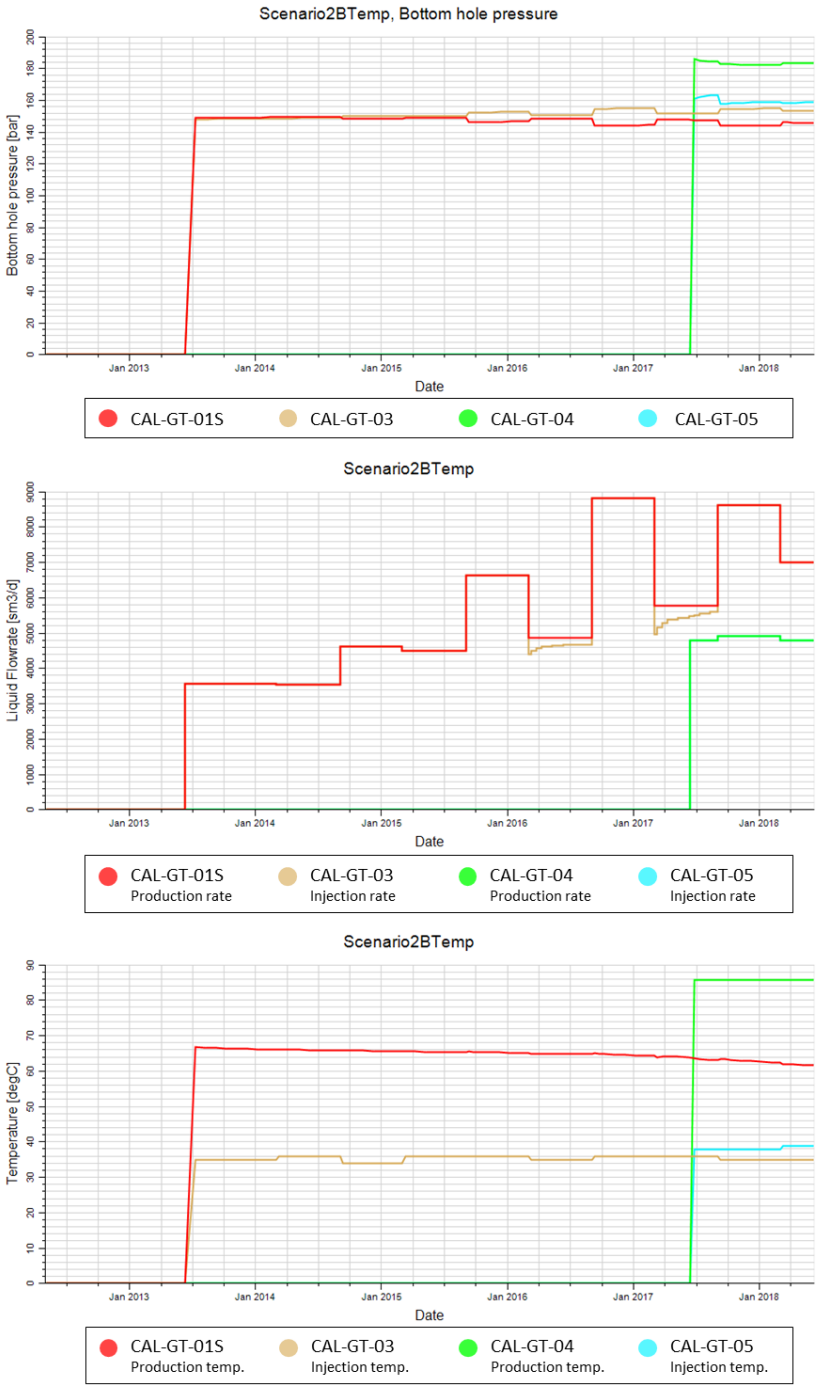

Appendix E. 22. Case: Scenario2BTemp. BHP, Flow rate and temperature profile for Scenario2B with a decreased reservoir temperature gradient (31 ˚C/km, surface T = 11 C)